University of Cape Town
Department of Mathematics and Applied Mathematics

Finite System Size Effects on the Effective Coupling in Scalar Quantum Field Theory

MSc Thesis

Submitted by:
J.F. Du Plessis

Supervisor:
Prof. Jonathan Shock

Co-supervisor:
Prof. W.A. Horowitz

November 6, 2023

Extended Abstract

Findings from the Large Hadron Collider (LHC) provide evidence that quark-gluon plasma (QGP) formation , traditionally associated with large nucleus-nucleus collisions, also emerges in high multiplicity proton-proton ($p+p$) and proton-nucleus ($p+A$) collisions [1–4]. It has also been shown that azimuthal correlations of low transverse momentum outgoing particles from these high multiplicity $p+p$ and $p+A$ collisions can be modeled well using nearly inviscid relativistic hydrodynamics [5]. One would expect the equation of state (EOS) used in such hydrodynamic simulations to receive significant contributions in systems of size characteristic of $p+p$ collisions. Indeed it has been shown that free scalar thermal field theory receives $\sim 40\%$ corrections to the usual thermodynamic quantities when confined using Dirichlet boundary conditions with characteristic lengths set by central $p+p$ collisions [6]. Furthermore, the potential importance of asymmetric system sizes has also been highlighted in quenched lattice QCD calculations using periodic boundary conditions [7]. In order to analyse the finite system size corrections to the QCD EOS, we need to explore the finite system size corrections to the running of the QCD coupling.

This thesis provides a first step toward such a calculation. We consider massive scalar ϕ^4 theory in a spacetime with periodic boundary conditions. We allow characteristic lengths to be asymmetric, or even infinite. We first recount the infinite volume NLO $2 \to 2$ scattering amplitude calculation using dimensional regularisation, and then introduce and employ denominator regularisation. We then perform the non-trivial calculation of the NLO $2 \to 2$ scattering amplitude in our compactified spacetime. This requires the derivation of an new analytic continuation of the generalised Epstein zeta function after employing denominator regularisation in order to isolate the UV divergence. Denominator regularisation is necessary, since the usual techniques in dimensional regularisation no longer applies when we allow asymmetric characteristic lengths. We confirm that taking the limit of infinite characteristic lengths yields the usual infinite space-time result. We

then perform another non-trivial self-consistency check by verifying that the NLO $2 \to 2$ scattering amplitude satisfies unitarity in the form of the optical theorem, regardless of the number of compactified dimensions. In order to show this we derived a generalisation of a formula originally proposed by Hardy and Ramanujan, and interpret its analytic continuation in the context of Abel summation. We numerically explore the scattering amplitude in some special cases, but find the s-channel of the 2 compactified dimension case to be numerically ill-behaved. We then derive and employ a dispersion relation in order to numerically explore the s-channel. Using the Callan-Symanzik equation to derive the beta function, we find it insensitive to finite system effects, which only modifies the IR. We then perform a geometric resummation of bubble diagrams, and show that the running coupling from the beta function agrees to a leading log in energy to the resummed amplitude. Interpreting the modulus of the resummed amplitude as an effective coupling in analogy to QED, we numerically explore its dependence on energy scale as well as the length scale of the system. We find that surprisingly at small length scales the effective coupling decreases, even though the beta function is positive.

This thesis has overlap with related work by the author [8–13].

Acknowledgements

With heartfelt gratitude, I acknowledge the enduring and invaluable support, guidance, and mentorship of my co-supervisor, Prof. Will Horowitz. From welcoming an unabashed undergraduate into his Quantum Field Theory lectures to his ongoing encouragement and wisdom, he has played a pivotal role in shaping me into the physicist and researcher I am today. His influence has been a constant, positive force in my development, and I will be forever indebted to him for his guidance.

I would also like to express my sincere appreciation to my supervisor Prof. Jon Shock for his instrumental role in bringing this thesis to fruition. His youthful optimism often transformed what seemed like insurmountable problems into challenges that were not only assailable but also enjoyable. Additionally, I will always have a deep appreciation for anyone that helps me go through some necessary but emaciating bureaucratic process.

Even though most of his various edits to the thesis have not made it into the final version, I must also extend a fuzzy thank you to my cat, Tigger. Not only has he been vocal about several strong opinions on the work presented here, but his warmth during the cold Stellenbosch winter of 2023 has also undoubtedly extended many of my working and writing sessions.

To Maja, Daniel, Adri, Kwas and my dad, I extend my condolences for enduring (sometimes inconsistent) ramblings about an s channel not converging.

Vir my vriende en familie se ondersteuning en liefde sal ek altyd dankbaar wees. Vele aande was 'n gesprek voor die vuur met mamma en pappa of "net nog een tubbo" met vriende net wat ek nodig gehad het om nog 'n paar uur se produktiewe werk in te kry. Ek moet ook my broer André bedank vir gedurig gewillig wees om al weer te luister hoe ek

fisika probeer verstaanbaar maak aan hom. Aan Maja, baie dankie vir oneindige liefde en ondersteuning. Vele probleme was opgelos na 'n stappie om die blok met jou. Laastens ook dankie aan Aandklas vir verskeie klippies specials om met Daniel te deel.

List of Acronyms

QFT	Quantum Field Theory
pQFT	perturbative Quantum Field Theory
QCD	Quantum Chromodynamics
EOS	Equation of State
QED	Quantum Electrodynamics
$\overline{MS}$	Modified Minimal Subtraction
BLM	Brodsky-Lepage-Mackenzie
LSZ	Lehmann–Symanzik–Zimmermann

Contents

Chapter 1

Introduction

This thesis begins with an abstract that is technical in nature, offering a precise background and synopsis for those well-versed in the field. If you find the abstract dense, challenging or even completely incomprehensible, fear not. The following introduction chapter is intended to be accessible to a wider audience. The first couple of sections in the introduction, accessible to anyone with a high-school level understanding of physics, serves as a welcoming gateway into the world of Quark Gluon Plasma. As you delve further into the "QGP in Small Systems" section, a university-level background in physics will enhance your comprehension, though some insights can still be gleaned without it. Finally, from "The QCD EOS Finite System Size Correction Program" and on we will be diving into more specialised territory and is best appreciated by those with a background in quantum field theory. This introduction is intended to contain all the background, laid out in a way I would have liked to be able to read in one place a couple of years ago. Enjoy.

1.1 The Big Bang

In the first microseconds of the universe, it is believed that the universe consisted of a substance called Quark-Gluon Plasma (QGP) [14–16]. In order to comprehensively understand these primordial instants of the universe, it is essential to study the behaviour of this peculiar state of matter. However, a conventional approach of observation, such

as using telescopes sensitive to electromagnetic (EM) radiation, presents a significant challenge. Much after quark gluon plasma has disappeared, estimated to be about 400,000 years later, the universe underwent a process that is called recombination. Due to the universe's expansion, the consequent cooling allowed the plasma filling the universe, which comprised free electrons and nucleons, to form the first atoms by capturing electrons into protons. The presence of these free charges resulted in the universe being opaque for its first ∼400,000 years. Following this period, the whole universe almost simultaneously became transparent to EM radiation. If we therefore look out into the universe with our telescopes (which, due to the finite speed of light, means looking back into the universe's history), we eventually look into a wall of electromagnetic plasma all around us, whose red-shifted radiation we call the Cosmic Microwave Background. A schematic picture of the evolution of the universe can be seen in Fig. 1.1, which shows the temperature evolution of the universe on a logarithmic scale. In Fig. 1.1, it is the period between the "Electro-Weak Transition" and "Hadro-Synthesis" that contains QGP, and recombination is at "Atom Formation". A standard text that covers the aforementioned cosmological concepts can be found at [17]. Since we are interested in the first microseconds, we therefore need another way of studying this substance and in order to know how we will study this QGP, we must first know what it is.

1.2 QGP and the QCD Phase Diagram

As with any substance in nature, nuclear matter exists in various phases [20, 21] dictated by parameters such as temperature that characterise its state. Analogous to ice transitioning into water with an increase in temperature, nuclear matter, under high enough temperatures, transitions into QGP. Fig. 1.2 is an illustration of the suspected structure of the Quantum-Chromodynamics (QCD) phase diagram. Baryon Chemical Potential (μ_B) should be interpreted as a parameter that parameterises the imbalance of quarks and anti-quarks (with $\mu_B > 0$ showing a net positive amount of expected quarks versus anti-quarks). We can see that at near 0 temperature and at a μ_B roughly corresponding

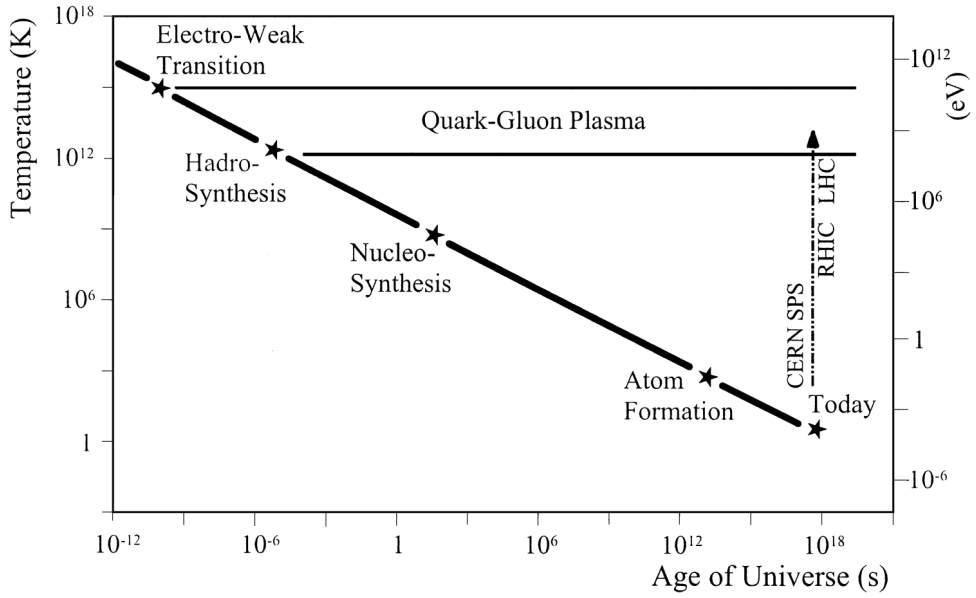

Figure 1.1: Figure and caption from [18] with permission from Elsevier. Temperature evolution of the universe as a function of time after Big Bang. The occurrence of various predicted transitions is indicated, as well as the path which heavy-ion experiments at different accelerators are exploring in order to recreate a QGP.

to the mass of a nucleon, we have the nuclear matter we are used to finding in the nuclei of atoms. As also shown in Fig. 1.1, the universe started out at an extremely large temperature (and is expected to start near $\mu_B = 0$), and cooled down as it expanded, moving along the arrow as indicated in Fig. 1.2. The precise location of the Critical point and the 1st order phase transition is still an ongoing search. Indeed their existence is only strongly suspected, and not guaranteed. The low temperature, large μ_B region of the phase diagram, corresponding to the circumstances thought to be found inside Neutron stars, is outside the scope of this thesis. Instead we are interested in the QGP region accessible to heavy-ion collision experiments.

The "plasma" in QGP signifies the free flow of colour charges, analogous to the free flow of electrical charges in conventional electromagnetic plasma. Various conditions can induce temperatures high enough in nuclear matter to facilitate QGP formation. One of them is in the immediate aftermath of the Big Bang, and another during the usage of heavy-ion colliders such as at the Large Hadron Collider (LHC) at the European Organisation for Nuclear Research (CERN) in Geneva, Switzerland or the Relativistic Heavy Ion Collider (RHIC) at Brookhaven National Laboratory (BNL) in New York.

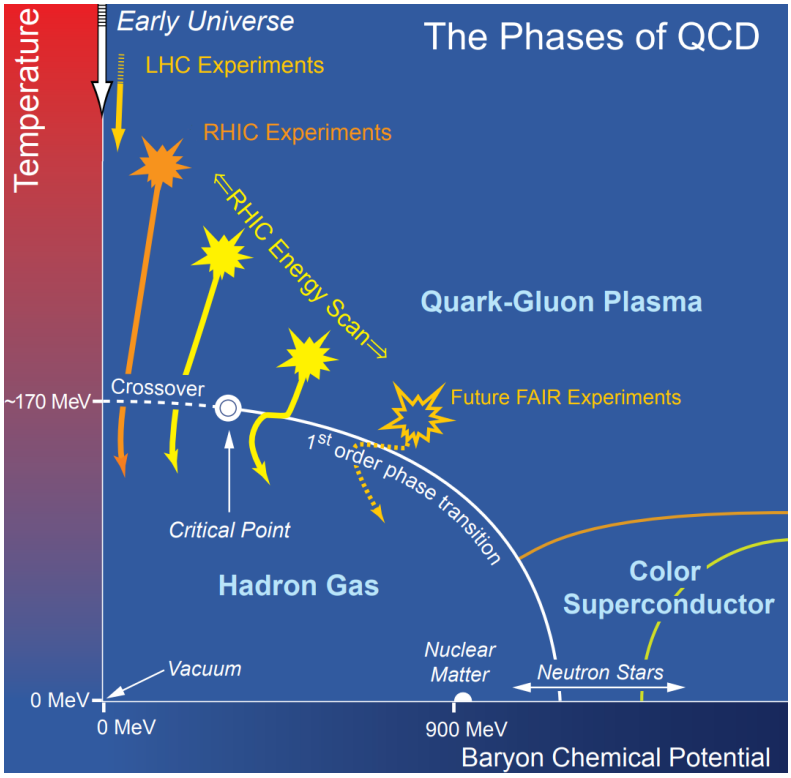

Figure 1.2: Figure adapted from [19]. An illustration of the suspected structure of the phase diagram for QCD in the Temperature-Baryon Chemical Potential Plane. Regions explored by current and future experiments are indicated,as well as suspected phase boundaries and phases.

Heavy-ion colliders accelerate heavy ions (nuclei of heavy atoms with their electrons stripped off) to near the speed of light, in order to collide them. Such collisions briefly recreate circumstances analogous to those found just after the Big Bang.

The phase diagram of water is determined by the properties of the electromagnetic force, as well as the water molecules which makes it up. Similarly the phase diagram of nuclear matter is determined by the relevant forces that it interacts through, as well as the constituent quarks and gluons as well as their various bound states. The region of the QCD phase diagram we are interested in is studied experimentally using heavy-ion collisions. We therefore need to not only understand the strong force, but also the heavy-ion collisions used to experimentally probe the QGP.

1.3 QED vs QCD

The strong force, whose interaction with quarks through gluons is accurately described by QCD, is one of the four known fundamental forces of nature. For an introduction to QCD, refer to [22–25]. The strong force is responsible for nucleons (protons and neutrons) and nuclei being held together. Electromagnetism, responsible for keeping atoms and molecules together, is well-described by Quantum-Electrodynamics (QED), which is also covered in [22]. Both QCD and QED are what is known as quantum field theories (QFTs). In order to get an idea of what makes QCD different from QED, we can compare some of their characteristics on a classical level (leaving out quantum effects for now). QED has many of the properties we are used to when thinking about electromagnetic phenomenon. Crucially it describes the existence of a single type of charge (electric charge) that comes in positive and negative variants. This charge obeys an inverse square law, which describes the force between electrically charged objects. Additionally, we observe that the electric charge is quantised, appearing only in multiples of a fundamental amount. Also, the photon, which carries the electromagnetic force, is electrically neutral. Consequently, the photon does not interact with itself directly, with any indirect interaction having a very low probability of occurrence. Therefore, charged objects can be pulled apart and eventually become fully separate. Moreover, when light beams intersect, they do not collide. QCD on the other hand differs in some crucial ways. Firstly, there are three colour charges, not to be confused with everyday perceptible colours, along with their inverse charges. This already complicates matters significantly. The three colour charges are designated as red, green, and blue because their combination results in a colour(-charge)-neutral ("white") object. In QED, the only way to have a charge-neutral object, is to have equal amounts of electric charge and its negative. In QCD that is one way of producing colour-charge-neutral objects. Another is to have the same amount of red green and blue net charge, giving a colour-neutral object. These colour charges follow an asymptotically constant force law at large distances, implying that colour-charged objects cannot be adequately separated without generating new coloured particles from the potential energy between them. This

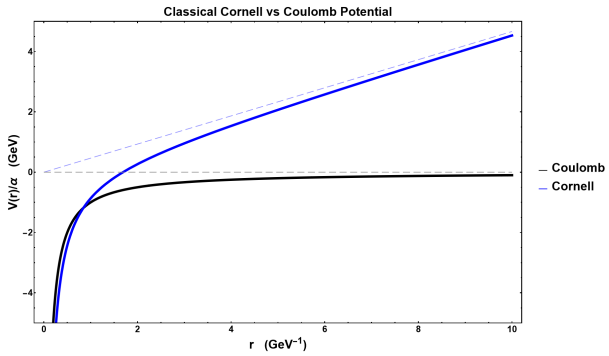

Figure 1.3: Comparison of behaviour of Classical Coulomb and Cornell potentials for QED and QCD respectively. Both are rescaled by their respective couplings $\alpha_{\text{EM}}, \alpha_{\text{S}}$, taken to have constant values of 1/137 and 0.39 respectively.

is due to the constant force, enabling an arbitrarily large potential energy with increased distance. This is why we only see colour-neutral objects in our everyday lives, while we do interact with electrically charged objects. The comparison of the potential energies of QED and QCD can be seen in Fig. 1.3. The Coulomb potential is given by $-\alpha_{\text{EM}}/r$ where, neglecting quantum effects we will discuss below, $\alpha_{\text{EM}} \approx 1/137 \approx 0.0073$. The Cornell potential [26] on the other hand is given by $-\alpha_{\text{S}}/r + \sigma r$ where $\alpha_{\text{S}} = 0.39, \sigma = 0.182$ GeV^2 are fit parameters [27]. In Fig. 1.3 we plot the Coulomb and Cornell potentials, each divided by their respective couplings $\alpha_{\text{EM}}, \alpha_{\text{S}}$ in order to see the qualitative differences (seeing as $\alpha_{\text{EM}} \ll \alpha_{\text{S}}$ would otherwise dominate the behaviour). We also show, with a light dashed black (blue) line, the asymptotically constant (linear) behaviour of the Coulomb (Cornell) potential. Colour charge is also quantised, but the gluon, a massless particle that carries the strong force, itself has colour charge (in fact it has one colour charge and one inverse colour charge). Consequently, "beams" of gluons would not simply pass through each other. Thus, in QCD, we have three charges and eight distinct force-carrying particles, complicating calculations significantly. Seeing that every gluon carries a colour charge and a colour anti-charge, and that there are three types of colour charges and anti-charges, one might so a naive calculation and conclude that there should be 9 distinct gluons. A complicated calculation however shows that only 8 independent types of gluons exist, where the ninth can be seen as a combination of the other 8. This turns out to be equivalent to the mathematical statement that although a traceless 3×3 matrix has 9 components, it only has 8 *independent* components. On a more technical level QED is

what is called an Abelian gauge theory, while QCD is a non-Abelian gauge theory, which generally makes calculations more cumbersome. In a very loose sense, part of this can be seen in analogy with commutative ($AB = BA$) versus non-commutative ($AB \neq BA$) matrices (indeed the Abelian and non-Abelian labels refers to whether the generators of the relevant gauge group commute or not). If we have two commutative matrices A, B, then calculating the expansion of $(A+B)(A-B) = A^2 - B^2$ only requires us to calculate A^2 and B^2, the cross terms cancelling due to the commutativity. If, on the other hand, A, B are matrices that do not commute, then $(A+B)(A-B) = A^2-B^2+BA-AB$, where the cross terms no longer cancel. In a similar way, many calculations in Abelian gauge theories contain convenient cancellations that analogous non-Abelian gauge theories do not have.

We can also consider some differences between QCD and QED that arise due to quantum effects. We might not be used to it in our everyday lives, but it is an experimental [28] and theoretical [22] fact that the apparent charge of an electron varies with the observer's distance from it or, equivalently, the energy at which it is observed. This is a more general feature of interacting QFTs, known as the running of the coupling. A common intuitive (slightly hand-wavy) way to think about it in QED is that there is a "true" electron possessing an infinite "bare" charge. In QFTs, it is possible (through the Heisenberg uncertainty principle) that for a brief time, an electron and a positron pop into existence, before annihilating each other. Such particles are referred to as virtual particles. If there is this true electron, then the (positive) virtual positron will be more likely to be closer to the true electron than the virtual electron, which is repelled from the true electron. This phenomenon is known as vacuum polarisation. Since we are in a spherically symmetric situation its best to think of "shells" of charged virtual particles. Due to the shell theorem [29], we can only detect the presence of two shells of equal but opposite charge if we are between them. Positrons tending to be closer to the "true" electron" due to vacuum polarisation results in a net positive charge in the vacuum between you and the "true" electron, and a net negative charge outside. This means that some of the charge of the electron gets hidden from us, usually referred to as charge screening, but the amount it

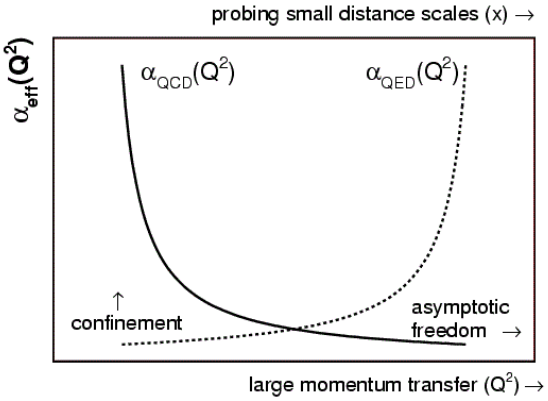

Figure 1.4: Figure from [30] of behaviour of QCD and QED running couplings at different momentum transfers/distance scales.

gets hidden by of course then depends on our proximity to the electron. Consequently, the apparent charge of the electron will be reduced (the bare charge is screened more) at large distances or equivalently at low energies. QCD, on the other hand, is again more complicated than QED. Colour-charge screening occurs in QCD, much like the charge screening in QED we just discussed. However, since gluons (the force carriers of QCD) can directly interact with each other, a potent "anti-screening" effect arises, which more than cancels out the screening from vacuum polarisation. The consequence is that QCD describes an interaction that becomes stronger at large distances and weaker at short distances. This phenomenon is known as asymptotic freedom [31, 32]. The conditions under which the interaction is weak are significant, as the primary method used for our calculations, referred to as perturbative quantum field theory (pQFT), only applies when interactions are weak. A comparison of the running couplings in QED and QCD is depicted in Fig. 1.4. Additionally, Fig. 1.5 shows experimental measurements of the running couplings for QCD and QED, respectively. We can see that when the momentum involved in an experiment with QED (QCD) is low (high) the coupling will be small, such that pQFT applies.

1.4 Heavy-ion collisions

Heavy-ion collisions [14, 18] generally involve two beams of heavy nuclei (nuclei with many nucleons) being accelerated to near the speed of light, before being collided in a

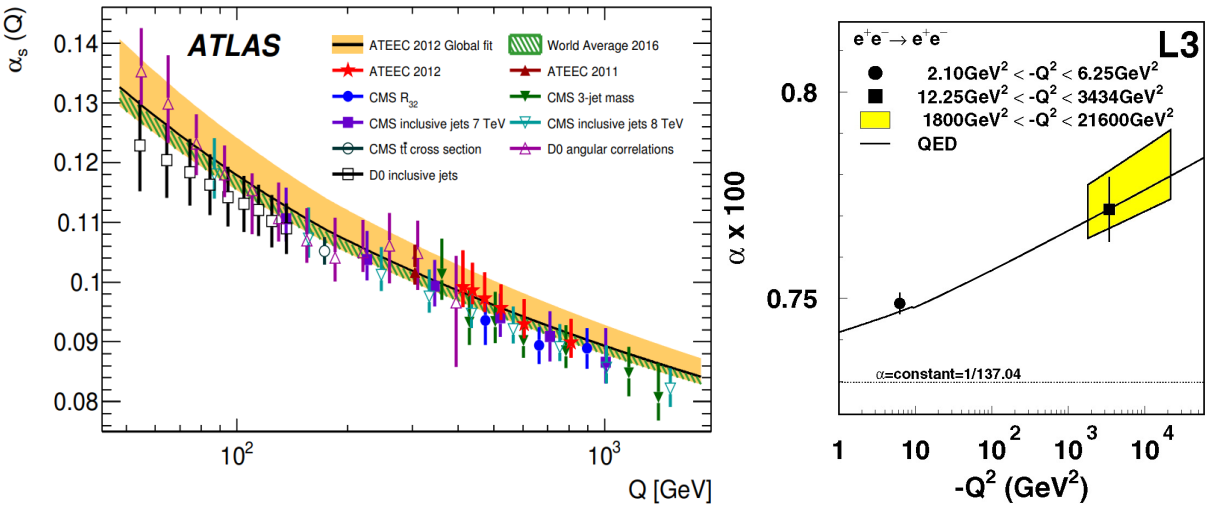

Figure 1.5: *Left*: Figure from [33] with permission from Springer. Various experimental results showing the running of the QCD coupling with energy and its agreement with theory.
Right: Figure from [28] with permission from Elsevier. Some experimental results showing the running of the QED coupling with energy and its agreement with theory.

detector. It is also possible to collide a beam with a stationary target which has several drawbacks, but also advantages. For the large energies required for QGP formation, beam experiments are the advantageous approach. Generally, ion-ion collisions are denoted as $A + A$ collisions, but when a specific ion like lead (Pb) is used, it is represented as a $Pb + Pb$ collision. Using different ions, usually gold (Au) or lead (Pb), leads to some important differences. Since lead as a larger nucleus (more nucleons) than gold, one has the $Pb + Pb$ collisions generally has larger multiplicities and centre of mass energies (usually denoted $\sqrt{s}$), in addition to providing a larger overlap region for the nuclei. It is also possible to collide a single proton with an ion, which is denoted as a $p + A$ collision, or just a proton with another proton, signified as a $p + p$ collision. Also note that other conventions include dropping the "+" symbols. Given that the incoming nuclei are travelling close to the speed of light, length contraction results in the two incoming nuclei appearing flattened in the detector's reference frame. These length contracted nuclei are sometimes referred to as "pancake" nuclei, and are depicted at the top left of Fig. 1.6. Not every collision will be head-on; typically, there exists a finite distance b, known as the impact parameter, between the centres of mass of the two nuclei. The impact parameter can be geometrically interpreted as the distance between the centres of the

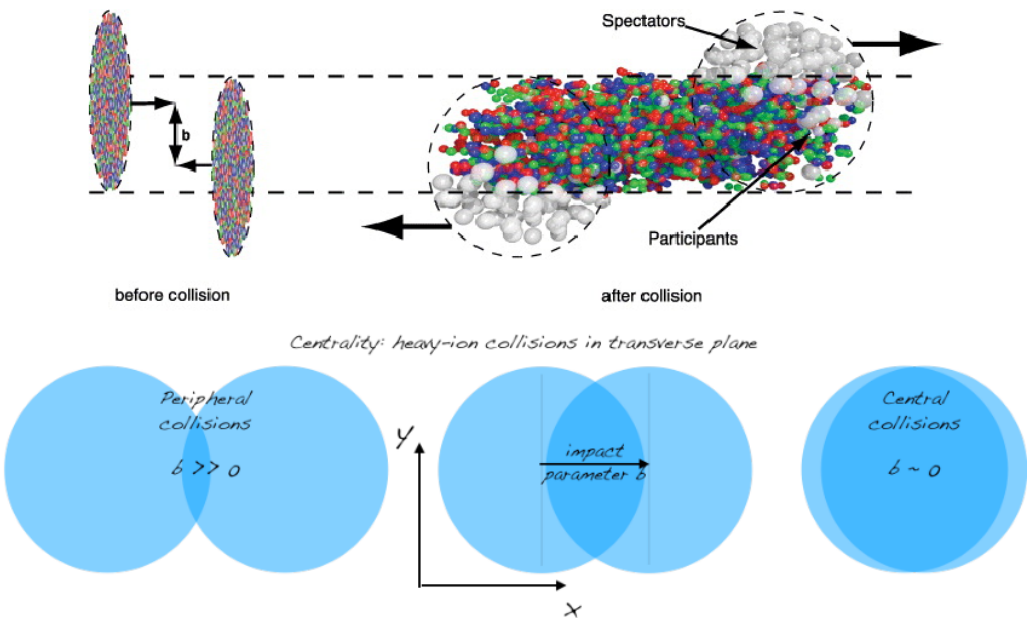

Figure 1.6: Figure and caption from [34]. *Top Left*: Two heavy ions before the collision with the impact parameter b. *Top Right*: The spectators remain unaffected while in the participant zone, particle production takes place. *Bottom*: An illustration of the often used nomenclature. Three collisions in the transverse plane are shown (from left to right): peripheral, semi-central, and central.

flattened nuclei at the moment of collision. In heavy ion collisions the impact parameter is generally a variable over which we have no direct control. In the region the two nuclei overlap, their respective nucleons will interact, and are called participants. Conversely, particles outside the overlap region generally continue moving along the beam direction and are termed spectators. This is illustrated at the top right of Fig. 1.6. The extent of overlap between the nuclei is termed the centrality of the collision. A central collision is essentially head-on, where the impact parameter is significantly smaller than the radii of the collided particles, and a non-central collision signifies a "glancing" collision, featuring only limited overlap between the collided particles. This can be seen at the bottom of Fig. 1.6. Ultra-peripheral collisions, where there is no overlap between colliding nuclei, do occur, but will not be discussed in this thesis. Our detectors generally pick up the energy-momentum, charge-to-mass ratio of the outgoing particles (and in general not along the beam direction). We can also detect whether a given particle is electromagnetic or hadronic (a bound state of quarks, antiquarks and gluons), and sometimes the outgoing speed of the particles. With this information it's important to note that the particles

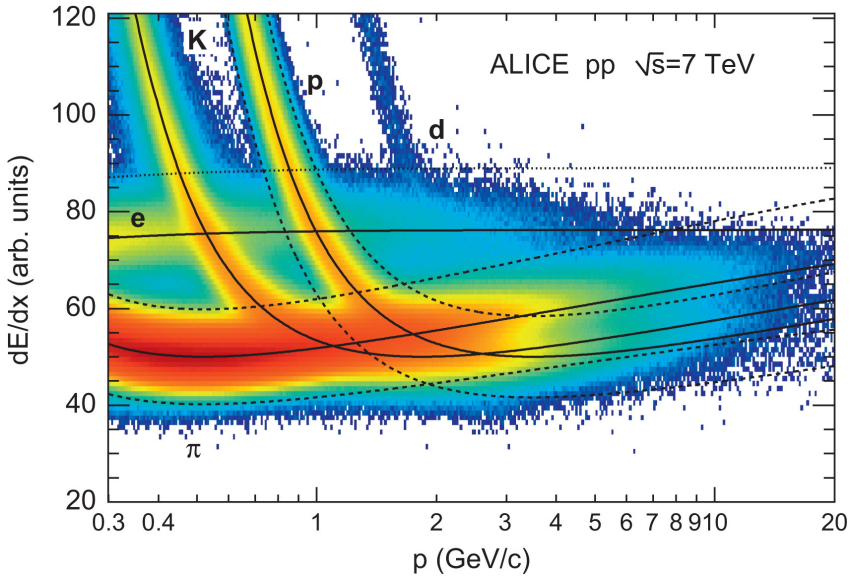

Figure 1.7: Figure from [35] with permission from Elsevier. Particle identification using momentum and energy loss.

created immediately post-collision aren't generally those observed, given that many of these particles are short-lived, decay rapidly, or tend to form bound states with other particles. From this limited information and experimental control, we need to then work backwards in order to probe the behaviour during these complicated and chaotic collisions that in general involve a huge number of outgoing particles. It is often important to detect the type of outgoing particles. In order to do this one can use the momentum and energy loss of the particle in order to attempt to identify particle type, as illustrated in Fig. 1.7. One of the most straightforward observables is the number of particles detected leaving the collisions, known as multiplicity. We generally only measure the multiplicity of charged outgoing particles, as they are readily measurable. Multiplicity can be used to categorise our collisions into centrality classes, where, for example, the 10% most central collisions are grouped together, followed by the next 10-20% most central, and so forth. This is often called "binning" the data. An illustration of such a binning procedure is shown in Fig. 1.8.

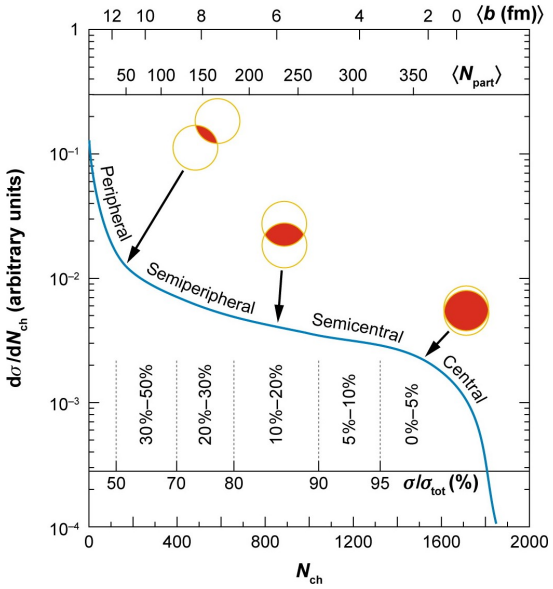

Figure 1.8: Figure from [36] with permission from Annual Reviews. An illustration (not actual measurements) of the correlation of the observable charged-particle multiplicity N_{ch} with expectation values of quantities calculated from simulations (the impact parameter b and number of participating partons N_{part}).

1.5 QGP Formation Signatures

The initial expectation was that QGP formation would primarily occur in central $A + A$ collisions, and that $p + A$ and especially $p + p$ collisions would serve as a baseline, given that QGP formation was not anticipated in these systems, to aid interpretation of QGP formation signatures in $A + A$ collisions [37]. There are several standard signatures of QGP formation. In what follows, suppression (enhancement) implies something being reduced (increased) relative to a baseline. One of the most prominent signatures of QGP formation is jet quenching [38,39]. In this context, a "jet" refers to a cascade of particles originating from a common source in the collision, generally a high-energy quark or gluon. These energetic particles are produced early in the collisions, and as they move through (potentially) the hot and dense medium formed by the collision, they interact with the (potential) medium and lose energy, a process referred to as jet quenching. This energy loss mechanism shows up as a suppression of high transverse momentum (p_T) particles measured. If QGP were not formed, there would not be a hot and dense medium to interact with and lose energy to, so jet quenching is a strong indicator of QGP formation. Suppression of high p_T particles that would interact with QGP in $Au + Au$ collision with

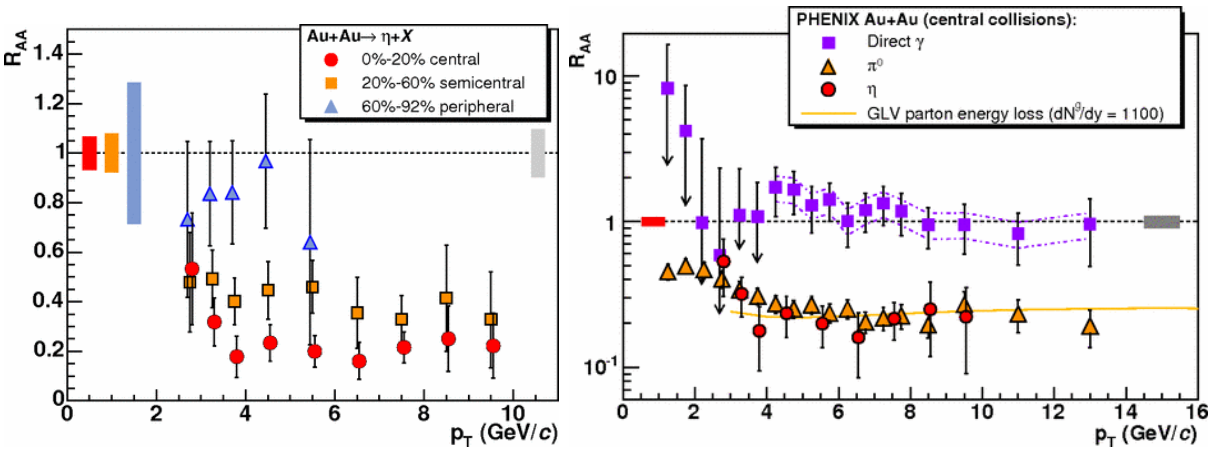

Figure 1.9: Figures and captions from [40] with permission from APS.
Left: Nuclear modification factors for η in Au+Au centralities: 0%–20%, 20%–60%, 60%–92%. The error bars show point-to-point uncertainties. The absolute normalization error bands at $R_{AA} = 1$ show the uncertainties in $\langle T_{AA} \rangle$ for decreasing centralities. The error box on the right indicates the 9.7% $p + p$ cross-section uncertainty.
Right: $R_{AA}(p_T)$ measured in central Au+Au at $\sqrt{s_{NN}} = 200$ GeV for η, π^0 [41] and direct γ [42]. The error bars include all point-to-point errors. The error bands at $R_{AA} = 1$ have the same meaning as in the left figure. The baseline $p + p \rightarrow \gamma + X$ reference used is a NLO calculation [42, 43], that reproduces our own data well [44], with theoretical uncertainties indicated by the dash-dotted lines around the points. The solid yellow curve is a parton energy loss prediction for a medium with density $dN^g/dy = 1100$ [45].

respect to $p + p$ collisions is shown in Fig. 1.9. R_{AA} in Fig. 1.9 is the so called nuclear modification factor, which is a ratio between what is measured in an $A + A$ collision, and what would theoretically be expected if the $A + A$ collision was simply the combination of $p + p$ collisions. So suppression is given by $R_{\mathrm{AA}} < 1$. We then see that on the left of Fig. 1.9 that more central collisions tend to have larger suppression, due to the jets having to traverse more medium. We furthermore also have a lack of suppression of photons (denoted by γ) on the right of Fig. 1.9, due to their lack of interaction with the medium, confirming that the observed suppression does not come from initial-state effects. We also see equal suppression of high p_T η and π^0 mesons, despite the significantly larger mass of the η meson, suggesting that the energy loss occurs before the quarks that make them up combine, showing that the suppression must happen in the medium itself.

Another signature of QGP formation is the increased production of strange quarks, a phenomenon known as strangeness enhancement [46]. Under ordinary conditions, the production of particles containing strange quarks is relatively suppressed due to the larger

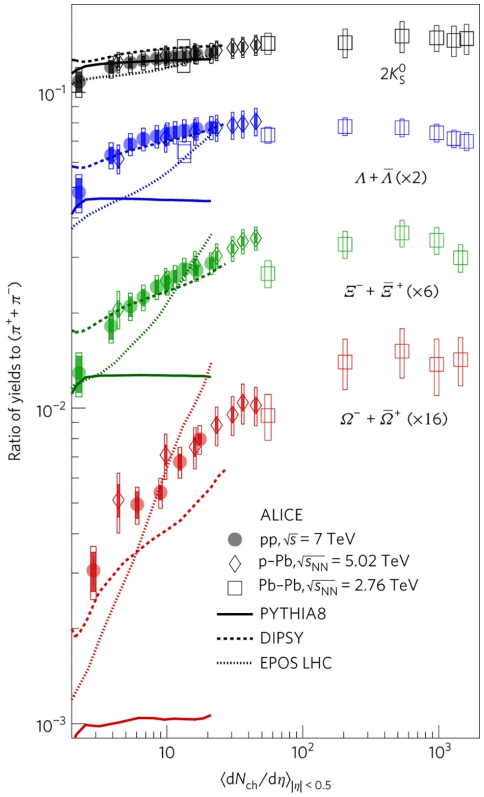

Figure 1.10: Figure from [52] with permission from Springer. Strange particle enhancement as a function of (charged) multiplicity for $p + p$, $p + Pb$ and $Pb + Pb$ collisions.

mass of the strange quark compared to the up and down quarks that generally make up protons and neutrons. However, in the extreme conditions of heavy-ion collisions, a significant increase in the production of strange particles, such as kaons (K) and lambda particles (Λ), has been observed [47–51]. This enhancement implies that the energy densities reached in the collision are high enough to facilitate the production of strange quark-antiquark pairs, which then hadronise into strange particles. This observation is in line with theoretical predictions of QGP formation [46], where a deconfined state of quarks and gluons allows for the enhanced production of heavier quarks. In Fig. 1.10 we see that strangeness enhancement is larger for particles with larger strangeness content. We also note the agreement between $p + p$, $p + Pb$ and $Pb + Pb$ collisions at equal multiplicities.

Conversely, one finds that QGP formation would cause a suppression of J/Ψ mesons [53]. In QGP, the presence of free colour charges, screens the binding of the charm quark with its antiquark, meaning the formation of J/Ψ mesons gets suppressed. The colour

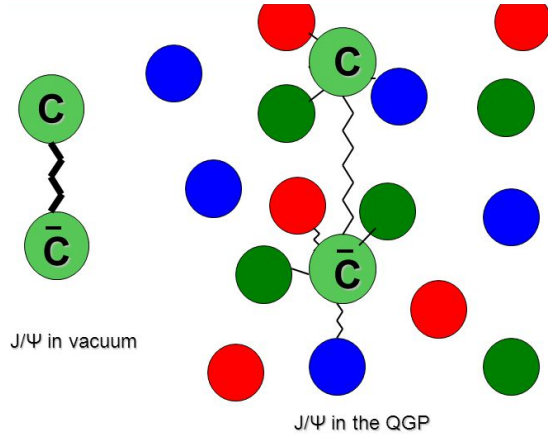

Figure 1.11: Figure from [54]. Illustration of the colour screening of charm quarks in QGP.

screening effect of QGP is illustrated in Fig. 1.11. In Fig. 1.12 one can see increased suppression in central collisions, since a larger portion of J/Ψ mesons would have been formed in the QGP itself, and have therefore experienced screening.

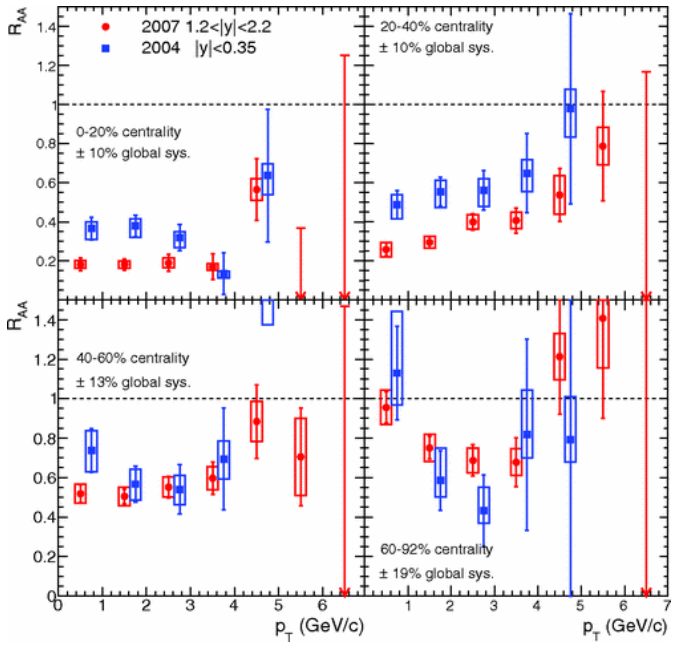

Figure 1.12: Figure from [55] with permission from APS. Nuclear modification factors R_{AA} for J/Ψ meson production in $Au + Au$ collisions as a function of transverse momentum p_T at different centralities.

The last signature we will discuss here is commonly known as elliptic flow. In non-central collisions, the overlap region of the two colliding particles is geometrically "almond" shaped, as illustrated in the left of Fig. 1.13. This spatial anisotropy causes pressure gradients, which turns the spatial anisotropy into outgoing-momentum anisotropy,

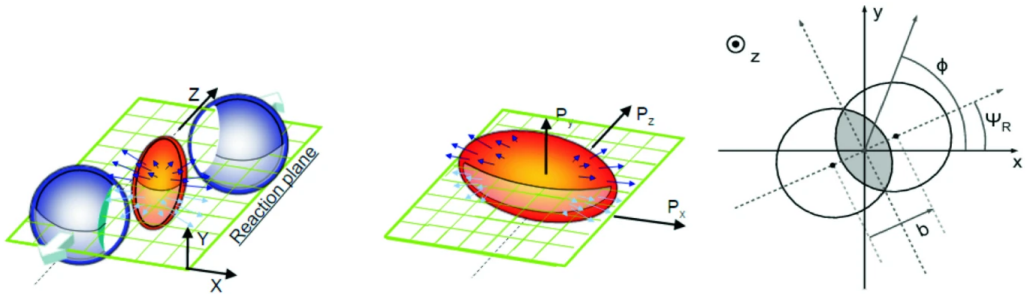

Figure 1.13: Figure and caption from [56]. *Left*: Depicting the spatial anisotropy of the almond-shaped overlap zone in non-central heavy-ion collision. *Centre*: Spatial anisotropy resulting in the momentum anisotropy. *Right*: Picture of a non-central heavy-ion collision in the transverse (x versus y) plane. Z (beam axis) is perpendicular to the plane of the figure. Φ is the azimuthal angle of one of the outgoing particles. Ψ_R is the reaction plane angle and b is the impact parameter

as illustrated at the centre of Fig. 1.13 (this process has been called Nature's Fourier transform). The anisotropy in the outgoing momentum can be quantified by the size of the higher Fourier coefficients of the Fourier transform of the azimuthal distribution of outgoing particles. The most notable is the second Fourier coefficient, commonly denoted by v_2, which is connected to the aforementioned elliptic flow. Some experimental measurements of v_2, v_3 and v_4 in $p+p$, $p+Au$ and $Au+Au$ collisions from ATLAS and CMS is shown in Fig. 1.14.

One then finds that not only are these QGP formation signatures found in $A+A$ collisions at both the LHC [57] and the RHIC [40], but modelling the QGP using relativistic hydrodynamics (modelling it as a fluid where its constituents move at relativistic speeds) gives an excellent account of many of the observables [5, 58]. Furthermore, one needs this fluid to be nearly inviscid, having so called shear viscosity close to the (conjectured) theoretical limit $\eta/s = 1/(4\pi)$ set by infinite coupling AdS/CFT calculations [59]. An example of viscous relativistic hydrodynamics being used in [5] to to model observed v_2 results in $Pb+Pb$ collisions is shown on the right in Fig. 1.14. We can see that v_2, v_3 and v_4 has very good agreement between the simulations and experiment, motivating the assertion that QGP acts as a strongly coupled, nearly inviscid relativistic fluid.

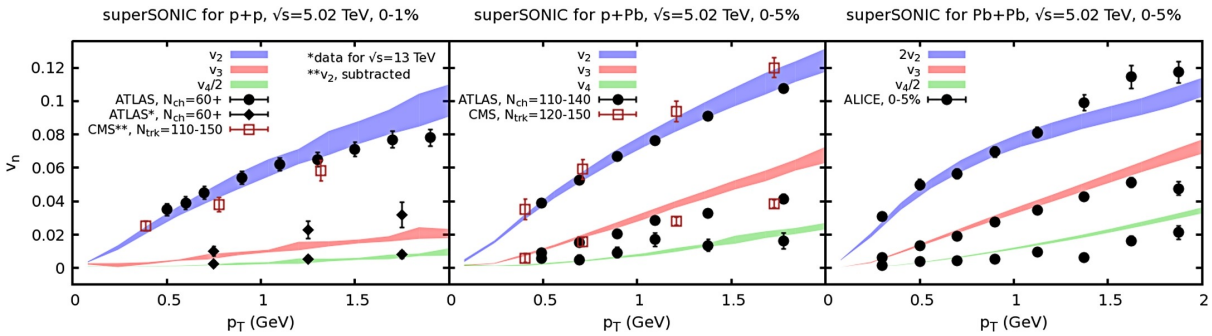

Figure 1.14: Figure from [5] with permission from Elsevier. Comparison of the Fourier coefficients v_2, v_3, v_4 from a hydrodynamic model to experimental data high from multiplicity $p+p$, $p+Pb$ and $Pb+Pb$ collisions from left to right. Simulations used a shear viscosity to entropy density ratio $\eta/s = 0.08$ and a bulk viscosity to entropy density ratio of $\zeta/s = 0.01$.

1.6 QGP in Small Systems

Many of these QGP formation signatures have now also been observed in high-multiplicity $p+A$ and even $p+p$ collisions, where nearly inviscid relativistic hydrodynamics can still be used to account for the experimental data [5]. These hydrodynamic simulations are run using the equation of state (EOS) that is valid for an infinite system, which is a good approximation in $A+A$ collisions, since corrections are expected to be on the order of $\frac{1}{LT_c}$, where L is the size of the system and T_c is the QCD critical temperature. In $A+A$ collisions $\frac{1}{LT_c}$ is small, but in $p+A$ and especially $p+p$ collisions, $\frac{1}{LT_c}$ is order 1, so one should naively expect significant corrections to the equation of state to be necessary. Numerically, the transition temperature $T_c \approx 155$ MeV [60] in natural units . The radius of a proton is $r_p \approx 10^{-15}\text{m} \approx 1/200\text{MeV}^{-1}$, while the radius of a lead nucleus for example is $r_{Pb} \approx 6 \times 10^{-15}\text{m} \approx 1/33\text{MeV}^{-1}$.

1.7 Small System Investigations so far

Free massless scalar thermal field theory with Dirichlet boundary conditions imposed has been investigated [6], finding more than 40% corrections to usual thermodynamic variables in systems the size of a $p+p$ collision, as can be seen in Fig. 1.15 for the free and total energy. Quenched lattice QCD calculations further showed the importance of asymmetric finite size systems [7].

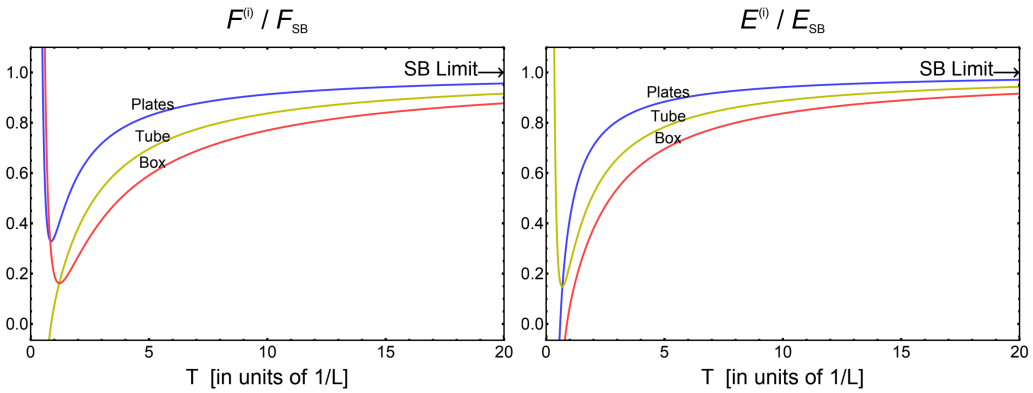

Figure 1.15: Figure and caption from [6] with permission from APS. The free energy (left) and the total energy (right) for a massless, non-interacting scalar field between two infinite parallel plates (blue lines), in an infinite symmetric tube (yellow lines), and in a finite volume symmetric box (red lines). The results have been rescaled by the Stefan-Boltzmann limits and are shown as a function of temperature T in units of $1/L$, where L is the distance between the sides of the system that are of finite length.

1.8 The QCD EOS Finite System Size Correction Program

The question then becomes if the QCD EOS actually does contain significant corrections due to system size, or if corrections are actually much smaller than may be expected. To determine this analytically one needs to understand QFTs in finite systems. In particular, the QCD EOS is set by the QCD trace anomaly in the massless quark limit. This can be seen from the observation that the trace of the energy-momentum tensor is given by the difference between the energy density and three times the pressure, so the trace of the energy momentum tensor directly yields the EOS. The QCD trace anomaly in the chiral (massless quark) limit comes from considering how the QCD Lagrangian changes under scale transformations. Classically, in infinite spacetime QCD is a conformal field theory (unchanged by dilatations), but as a QFT this symmetry is broken by the running of the coupling. One would similarly expect that since a finite system size also breaks the conformal symmetry, that finite systems should also introduce trace anomalies. However, a free scalar field at finite temperature with Dirichlet boundary conditions imposed, still yields a 0 trace for the energy momentum tensor [61]. Finite system size corrections to the QCD EOS should therefore come from the QCD coupling depending on the system

size. This dependence is not yet well-understood. We therefore set out to investigate the relatively simple case of massive scalar ϕ^4 theory in a system with (potentially asymmetric) periodic boundary conditions. Since the beta function as set by the Callan-Symanzik equation is insensitive to maximum length scales in the system (maximum length scales are an IR effect, while the running of the coupling with renormalisation scale is a UV effect), we should think of the Callan-Symanzik equation as capturing the running of the coupling at *constant* maximum length scale. We instead argue that a resummation of bubble diagrams gives us an effective coupling, which explicitly depends on the maximum length scales of the system. We show that if the renormalisation scale is set by some large kinematic energy scale, the running coupling agrees with the effective coupling to a leading logarithm in said energy scale. The effective coupling then gives us a way to investigate both the kinematic and geometric running of the coupling. The central goal of this thesis will then be to derive an analytic expression for the effective coupling of massive scalar ϕ^4 theory in a finite system, and to provide a numerical exploration of the behaviour of the effective coupling as a function of kinematics and geometry.

1.9 Thesis Outline

We will start by recounting the usual derivation of the LO and NLO $2 \to 2$ scattering amplitudes in infinite spacetime using the usual technique of dimensional regularisation in Chapter 2. This will provide a valuable base result to refer back to. In preparation for the finite system calculation, we will introduce and employ denominator regularisation in Chapter 3 (and motivated further in App. A), to see that we get the same amplitude as with dimensional regularisation (as we must). Denominator regularisation will be required when we impose asymmetric periodic boundary conditions, since the usual techniques in dimensional regularisation will no longer apply. After imposing boundary conditions in Chapter 4 we find that in order to isolate the usual UV divergence in $d = 3 + 1$ total spacetime dimensions, a new analytic continuation of the generalised Epstein zeta function is required. Using this analytic continuation derived in App. B and applying

the modified $\overline{\text{MS}}$ renormalisation scheme identified in the infinite spacetime calculation, we find an amplitude that limits to the infinite spacetime result when all lengths of the finite dimensions are taken to infinity. We furthermore verify that unitarity in the form of the optical theorem is satisfied for any number of dimensions finite in Chapter 5. This requires the generalisation of a number theoretic formula originally proposed by Ramanujan and Hardy, which we derive in App. C. We also briefly discuss interpreting the derived generalisation as an analytic continuation, valid in the sense of Abel summation. We then move on to numerically investigate the s and t channels of the NLO amplitude for 1 and 2 dimensions finite in Chapter 6, which necessitated exploiting analytic properties of the amplitude in App. D. This leads us to discover "geometric bound states", identified by their corresponding poles in the S matrix, as with more generic bound states. Brief asymptotic analysis of the t channel with all 3 spatial dimensions finite is also provided in Chapter 7, and it is shown to agree with numerics well. We then numerically explore the effective coupling in Chapter 8, taking care to interpret its behaviour around geometric bound states and in the $pL \to 0$ limits carefully and separately. With 2 finite dimensions we find large corrections even at moderate system sizes and momenta. We finally provide a discussion and some closing remarks in the Conclusions.

Chapter 2

Infinite Volume Scattering

2.1 Field Theory Defined

In order to prepare for the finite system size calculation, to fix some notation, and to provide a valuable reference to compare to, we compute $2 \to 2$ scattering at NLO in massive ϕ^4 theory using dimensional regularisation and the $\overline{\text{MS}}$ renormalisation scheme [22].

We begin with the bare Lagrangian for ϕ^4 theory:

$$\mathcal{L} = \frac{1}{2}\partial_\mu\phi_0\partial^\mu\phi_0 - \frac{1}{2}m_0^2\phi_0^2 - \frac{\lambda_0}{4!}\phi_0^4. \tag{2.1}$$

We choose as usual to multiplicatively renormalise. We'll work in $d = 4 - \epsilon$ spacetime dimensions. In order to fix our coupling constant to be dimensionless in any number of spacetime dimensions, we introduce a scale μ, with dimensions of energy,

$$\begin{aligned} \phi_r &\equiv Z_\phi^{-1/2}\phi_0 \\ m_r^2 &\equiv Z_m^{-1}Z_\phi m_0^2 \\ \lambda_r &\equiv Z_\lambda^{-1}Z_\phi^2\mu^\epsilon\lambda_0. \end{aligned} \tag{2.2}$$

Further defining

$$\begin{aligned} Z_\phi &\equiv 1 + \delta_\phi \\ Z_m &\equiv 1 + \frac{1}{m^2}\delta_m^2 \\ Z_\lambda &\equiv 1 + \frac{1}{\lambda_r}\delta_\lambda \end{aligned} \tag{2.3}$$

we arrive at the renormalised Lagrangian

$$\mathcal{L} = \frac{1}{2}\partial_\mu\phi\partial^\mu\phi - \frac{1}{2}m^2\phi^2 - \frac{\lambda}{4!}\mu^\epsilon\phi^4 + \delta_\phi\frac{1}{2}\partial_\mu\phi\partial^\mu\phi - \delta_m^2\frac{1}{2}\phi^2 - \delta_\lambda\mu^\epsilon\frac{1}{4!}\phi^4, \tag{2.4}$$

where we've dropped all r subscripts on renormalised quantities for notational convenience.

2.2 LO scattering

When we perform LSZ reduction [62], we must take care with R_ϕ, the residue of the propagator at the physical mass. However, for ϕ^4 theory in $4-\epsilon$ spacetime dimensions, one has that the first order correction to the scalar self energy is

$$\begin{aligned} -i\Sigma^{[1]}(p^2) = &\quad \text{ 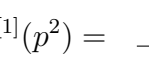 } \quad + \quad \text{ 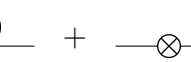 } \\ &= \frac{-i\lambda\mu^\epsilon}{2}\frac{1}{(4\pi)^{d/2}}\frac{\Gamma\left(1-\frac{d}{2}\right)}{(m^2)^{1-\frac{d}{2}}} + i(p^2\delta_\phi - \delta_m^2). \end{aligned} \tag{2.5}$$

Since the divergence is momentum independent, we may take $\delta_\phi = 0$, and we have that $R_\phi = 1 + \mathcal{O}(\lambda^2)$.

Thus when we compute the leading order amplitude for $2 \to 2$ scattering, we find

$$\begin{aligned} i\mathcal{M} = &\quad \text{  } \quad = -i\lambda\mu^\epsilon + \mathcal{O}(\lambda^2) \\ &\xrightarrow[\epsilon\to 0]{} -i\lambda + \mathcal{O}(\lambda^2); \end{aligned} \tag{2.6}$$

i.e. there's no symmetry factor in this particular case.

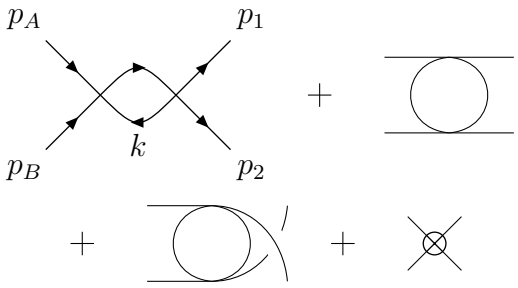

Figure 2.1: The four diagrams contributing to the NLO correction to $2 \to 2$ scattering in our renormalised ϕ^4 theory. Momenta are labelled on the s channel diagram but are suppressed for simplicity on the t and u channel diagrams.

2.3 NLO scattering

The diagrams associated with the NLO correction to $2 \to 2$ scattering are shown in Fig. 2.1. Let's focus on the s channel diagram. A detailed examination of the contracted fields shows that the symmetry factor is $S = 1/2$. Then defining $p \equiv p_A + p_B$ and $V(p^2; \mu, \epsilon)$ by

$$(-i\lambda)^2 \mu^\epsilon i V(p^2; \mu, \epsilon) \equiv$$

we have that

$$(-i\lambda)^2 \mu^\epsilon i V(p^2; \mu, \epsilon) = \frac{(-i\lambda\mu^\epsilon)^2}{2} \int \frac{d^d k}{(2\pi)^d} \frac{i}{k^2 - m^2 + i\varepsilon} \frac{i}{(p+k)^2 - m^2 + i\varepsilon}. \tag{2.7}$$

Note the $\epsilon > 0$ that guarantees convergence of the integral on the right-hand side of the expression, which is different from the $\varepsilon > 0$ that enforces the Feynman propagator pole prescription. Following the usual procedure to combine denominators using a Feynman x parameter, Wick rotating, and evaluating the resulting Euclidean integral, and expanding to $\mathcal{O}(\epsilon)$ yields

$$V(p^2; \mu, \epsilon) = -\frac{1}{2} \frac{1}{(4\pi)^2} \int_0^1 dx \left[\frac{2}{\epsilon} - \gamma_E + \ln 4\pi + \ln \frac{\mu^2}{-x(1-x)p^2 + m^2 - i\varepsilon} \right] + \mathcal{O}(\epsilon). \tag{2.8}$$

Note that close examination of the location of the poles of the denominator (combined in the usual way using the Feynman x parameter) shows that the poles are restricted to the second and fourth quadrants in the complex plane for both $p^2 > 0$ and for $p^2 < 0$; hence the Wick rotation, and thus Eq. (2.8), are valid for $p^2 \in \mathbb{R}$.

Applying the $\overline{\text{MS}}$ renormalisation scheme fixes the coupling counterterm to

$$\delta_\lambda = 3\lambda^2 \frac{1}{2}\frac{1}{(4\pi)^2}\Big[\frac{2}{\epsilon} - \gamma_E + \ln 4\pi\Big] \tag{2.9}$$

and the renormalised NLO contribution to

$$\overline{V}(p^2;\mu) = -\frac{1}{2}\frac{1}{(4\pi)^2}\int_0^1 dx \ln\frac{\mu^2}{-x(1-x)p^2 + m^2 - i\varepsilon}. \tag{2.10}$$

Thus up to NLO the $2 \to 2$ amplitude is

$$\begin{aligned} i\mathcal{M} &= -i\lambda\mu^\epsilon\big[1 + \lambda\big(V(s;\mu) + V(t;\mu) + V(u;\mu)\big) + \frac{1}{\lambda}\delta_\lambda\big] \\ &\xrightarrow[\epsilon\to 0]{} -i\lambda\big[1 + \lambda\big(\overline{V}(s;\mu) + \overline{V}(t;\mu) + \overline{V}(u;\mu)\big)\big]. \end{aligned} \tag{2.11}$$

One may perform a non-trivial cross check of Eq. (2.10) by confirming that the Optical Theorem is satisfied. For $p^2 > 4m^2$ and $x_- < x < x_+$, where

$$-x_\pm(1-x_\pm)p^2 + m^2 = 0 \tag{2.12}$$

$$\Rightarrow \quad x_\pm = \frac{1}{2}\left[1 \pm \sqrt{1 - \frac{4m^2}{p^2}}\right], \tag{2.13}$$

we have that

$$\text{Im } \ln\frac{\mu^2}{-x(1-x)p^2 + m^2 - i\varepsilon} = \pi. \tag{2.14}$$

Thus to order $\mathcal{O}(\lambda^2)$

$$\text{Im}\,\mathcal{M} = -\lambda^2\pi\Big[-\frac{1}{2}\frac{1}{(4\pi)^2}\Big]\int_{x_-}^{x_+} dx. \tag{2.15}$$

Therefore

$$2\,\text{Im}\,\mathcal{M} = \frac{\lambda^2}{16\pi}\sqrt{1 - \frac{4m^2}{s}}\theta(s - 4m^2) + \mathcal{O}(\lambda^3). \tag{2.16}$$

One may straightforwardly show that one arrives at the exact same result from evaluating

$$\sigma_{\text{tot}} = \frac{1}{2}\int \frac{d^3p_2}{(2\pi)^3 2E_{p_2}}\int \frac{d^3p_1}{(2\pi)^3 2E_{p_1}}|\mathcal{M}|^2(2\pi)^4\delta^{(4)}(p_A + p_B - p_1 - p_2), \tag{2.17}$$

where $\mathcal{M} = \lambda + \mathcal{O}(\lambda^2)$ is the leading order cross section, and one must be careful of the overall factor of $1/2$ due to the presence of two identical particles in the final state.

The four point Green function is given by $i\mathcal{M}$. Since to $\mathcal{O}(\lambda^2)$ there's no contribution

from an anomalous dimension γ, we have the Callan-Symanzik equation

$$(\mu\partial_\mu + \beta\partial_\lambda)\mathcal{M} = 0$$

$$(\mu\partial_\mu + \beta\partial_\lambda)\big[-\lambda - \lambda^2\big(\overline{V}(s;\mu) + \overline{V}(t;\mu) + \overline{V}(u;\mu)\big)\big] = 0. \tag{2.18}$$

Since $\mu\partial_\mu \overline{V}(p^2;\mu) = -(4\pi)^{-2}$, we find the standard result [22] that

$$\beta = \frac{3\lambda^2}{(4\pi)^2}. \tag{2.19}$$

And since $\beta \equiv \partial\lambda/\partial \ln\mu$, we must have that

$$\int_{\lambda(\mu_0)}^{\lambda(\mu)} \frac{d\lambda}{\lambda^2} = \int_{\ln\mu_0}^{\ln\mu} d\ln\mu' \frac{3}{4\pi^2} \tag{2.20}$$

$$\Rightarrow \qquad \lambda(\mu) = \frac{\lambda(\mu_0)}{1 + \lambda(\mu_0)\frac{3}{(4\pi)^2}\ln\mu_0/\mu}. \tag{2.21}$$

We'll refer to Eq. (2.21) as the *running* coupling.

For example, in $e^+ + e^- \to \mu^+ + \mu^-$ scattering in QED, one may exactly resum the geometric series of 1PI fermion loops to generate an *effective* coupling. For $p^2 \gg m_e^2$ the leading logarithmic behaviour of the effective coupling is identical to the running coupling from the Callan-Symanzik equation evaluated at the centre of mass energy s, $\alpha_{EM}(s)$. This resummation procedure can be more difficult for different processes and different theories. Nonetheless, the idea of an effective coupling is a valuable one. For example, in QCD one has the BLM scale setting procedure [63], in which one resums the fermion bubbles and then completes the beta function [64].

For our ϕ^4 theory, the correct geometric resummation that captures the leading logarithmic physics of the Callan-Symanzik equation for the $2 \to 2$ process involves the s, t, and u channels. Recalling that one may write $u(s,t)$,

$$\begin{aligned} -i\lambda_{\text{eff}}(s,t) &\equiv -i\lambda(\mu)\big[1 + \lambda(\mu)\big(\overline{V}(s;\mu) + \overline{V}(t;\mu) + \overline{V}(u;\mu)\big) \\ &\qquad + \lambda^2(\mu)\big(\overline{V}(s;\mu) + \overline{V}(t;\mu) + \overline{V}(u;\mu)\big)^2 + \dots\big] \\ &= \frac{-i\lambda(\mu)}{1 - \lambda(\mu)\big(\overline{V}(s;\mu) + \overline{V}(t;\mu) + \overline{V}(u;\mu)\big)}, \end{aligned} \tag{2.22}$$

where $\lambda(\mu)$ is the running coupling given by Eq. (2.21). At NLO, all μ dependence in Eq. (2.22) exactly cancels between the running coupling and in the $\overline{V}$'s, leaving λ_{eff} with no μ dependence at all. For $Q^2 \equiv -p^2 > 0$, one may easily evaluate the x integral in

Eq. (2.10) to find

$$\overline{V}(Q^2;\mu) = -\frac{1}{2}\frac{1}{(4\pi)^2}\left[2 - 2\sqrt{1+\frac{4m^2}{Q^2}} + \ln\frac{\mu^2}{m^2}\right] \tag{2.23}$$

$$= -\frac{1}{2}\frac{1}{(4\pi)^2}\ln\frac{\mu^2}{Q^2} + \mathcal{O}\big((m^2/Q^2)\big). \tag{2.24}$$

For $s \sim -t \sim -u \sim E^2 \gg m^2$ and we take $\mu^2 = E^2$ in the running coupling Eq. (2.21), then we once again have to leading log that $\lambda_{\text{eff}}(E^2) = \lambda(E^2)$.

Chapter 3

Denominator Regularisation

In the standard calculation recounted in Chapter 2 one relies heavily on the symmetry of (Wick rotated) spacetime in order to use dimensional regularization. When we move to the setup in which the spacetime is $\mathbb{R} \times T^n$, the potential asymmetry of the various spatial directions and the discrete momentum space sums mean that the usual techniques of dimensional regularisation are no longer applicable. Instead of making the calculation a function of the number of spacetime dimensions and analytically continuing to $d = 4$, we rather make the *power* of the denominator in the loop integral for V a function and analytically continue to the log divergent value of 2, as can be seen in [8,11]. In particular, in denominator regularisation the number of spacetime dimensions is fixed to 4. As a result, one doesn't need to introduce μ to keep the coupling dimensionless as a function of ϵ (a μ will still be introduced to keep the dimensions of V independent of the power of the denominator); the denominator regularisation renormalised Lagrangian is

$$\mathcal{L} = \frac{1}{2}\partial_\mu\phi\partial^\mu\phi - \frac{1}{2}m^2\phi^2 - \frac{\lambda}{4!}\phi^4 + \delta_\phi\frac{1}{2}\partial_\mu\phi\partial^\mu\phi - \delta_m^2\frac{1}{2}\phi^2 - \delta_\lambda\frac{1}{4!}\phi^4. \tag{3.1}$$

One must of course still have that $R_\phi = 1 + \mathcal{O}(\lambda^2)$ in denominator regularisation since the regularisation procedure cannot introduce any new divergences. Nevertheless, one may easily check explicitly that in denominator regularisation the one loop self energy is still momentum independent, and thus one has in denominator regularisation that $R_\phi = 1 + \mathcal{O}(\lambda^2)$. One trivially, then, has that $i\mathcal{M} = -i\lambda + \mathcal{O}(\lambda^2)$. At NLO, one has after

combining denominators with a Feynman parameter and Wick rotating

$$(-i\lambda)^2 iV(p^2) = i\frac{\lambda^2}{2}\int_0^1 dx \int \frac{d^4\ell_E}{(2\pi)^4}\frac{1}{(\ell_E^2+\Delta^2)^2}, \tag{3.2}$$

$$\Delta^2 \equiv -x(1-x)p^2 + m^2 - i\varepsilon. \tag{3.3}$$

The integral in Eq. (3.2) diverges logarithmically in the UV as the numerator scales like ℓ_E^3 and the denominator like ℓ_E^4. We now perform denominator regularisation by allowing V to depend on the power of the denominator. We introduce the denominator regulator ϵ (again distinct from ε) such that the integral converges for all $\epsilon > 0$. In order to maintain the dimensionlessness of V we introduce a scale μ with dimensions of energy. We then have

$$V(p^2;\mu,\epsilon) = -\frac{1}{2}\int_0^1 dx \int \frac{d^4\ell_E}{(2\pi)^4}\frac{\mu^{2\epsilon}}{(\ell_E^2+\Delta^2)^{2+\epsilon}}. \tag{3.4}$$

Similar to the dimensional regularisation procedure, one may perform the spherical integration over the full 4 dimensional spacetime. In order to better make contact with our future finite-sized spatial spacetime calculation, we rather perform the "temporal" integration first (temporal in quotes as in this case no direction is different from another). Then one has that

$$V(p^2;\mu,\epsilon) = -\frac{1}{2}\frac{1}{(2\pi)^4}\int_0^1 dx \frac{\sqrt{\pi}\Gamma\left(\frac{3}{2}+\epsilon\right)}{\Gamma(2+\epsilon)}\int d^3\ell_E \frac{\mu^{2\epsilon}}{(\ell_E^2+\Delta^2)^{\frac{3}{2}+\epsilon}}. \tag{3.5}$$

The remaining momentum integrals evaluate to

$$4\pi\int_0^\infty \ell_E^2 d\ell_E \frac{\mu^{2\epsilon}}{(\ell_E^2+\Delta^2)^{\frac{3}{2}+\epsilon}} = \frac{\sqrt{\pi}\Gamma(\epsilon)}{4\Gamma\left(\frac{3}{2}+\epsilon\right)}\left(\frac{\mu^2}{\Delta^2}\right)^\epsilon. \tag{3.6}$$

Thus

$$\begin{aligned} V(p^2;\mu,\epsilon) &= -\frac{1}{2}\frac{1}{(4\pi)^2}\int_0^1 dx \frac{\Gamma(\epsilon)}{\Gamma(2+\epsilon)}\left(\frac{\mu^2}{\Delta^2}\right)^\epsilon \\ &= -\frac{1}{2}\frac{1}{(4\pi)^2}\int_0^1 dx \left[\frac{1}{\epsilon} - 1 + \ln\left(\frac{\mu^2}{\Delta^2}\right)\right] + \mathcal{O}(\epsilon). \end{aligned} \tag{3.7}$$

It's interesting that the -1 of the finite part from denominator regularisation is identical to the -1 that one finds when regularising through an explicit UV cutoff, compared to the $-\gamma_E + \ln 4\pi$ one finds from dimensional regularisation. A similar calculation in which one performs the usual spherical integration over the full 4D space yields an identical result.

One can see that the denominator regularisation procedure reproduces the same $1/\epsilon$ divergence and $\ln \mu^2/\Delta^2$ dependence (with the same overall coefficient) for $V(p^2; \mu, \epsilon)$ as in dimensional regularisation (as it must); the only difference comes in the coefficient of the divergence (which is halved, but can simply be absorbed by a rescaling of ϵ) and the finite correction of -1 compared to $-\gamma_E + \ln 4\pi$. If we modify our $\overline{\text{MS}}$ prescription for denominator regularisation to absorb the $1/\epsilon$ divergence and the -1 instead of the $2/\epsilon$ divergence and the $-\gamma_E + \ln 4\pi$, then the renormalised NLO $2 \to 2$ cross section from denominator regularisation agrees exactly with that from the usual dimensional regularisation procedure. In particular, for our denominator regularisation procedure we take

$$\delta_\lambda = 3\lambda^2 \frac{1}{2} \frac{1}{(4\pi)^2} \Big[\frac{1}{\epsilon} - 1 \Big]. \tag{3.8}$$

Now that we have a way to regularize that does not rely on the symmetries of the phase space, we can proceed to consider ϕ^4 theory in a compactified spacetime with potentially asymmetric characteristic lengths in Chapter 4.

Chapter 4

Finite Size Corrections

4.1 Field Theory Defined

It's no more difficult to consider a real scalar field theory in only 4 spacetime dimensions with all three spatial dimensions periodic as to consider a very general scalar field theory with n directions periodically identified and m directions of infinite extent. Let the i^{th} compact spatial dimensions have size $[-\pi L_i, \pi L_i]$ and take

$$\begin{aligned}
\phi(x) = \sum_{\vec{k}\in\mathbb{Z}^n} \frac{1}{(2\pi)^n L_1 \cdots L_n} \int \frac{d^m p}{(2\pi)^m} \frac{1}{2E_{\vec{p}}} \\
\times \left[e^{-ip\cdot x} a(\vec{p}) + e^{ip\cdot x} a^\dagger(\vec{p}) \right], \\
p^i = \frac{k^i}{L_i}, \quad i = 1, \ldots, n \\
p^j = p^j, \quad j = 1, \ldots, m \\
p^0 = E_{\vec{p}} = \sqrt{\vec{p}^2 + m^2}.
\end{aligned} \tag{4.1}$$

Then

$$[a(\vec{p}), a^\dagger(\vec{q})] = (2\pi)^{n+m} 2E_{\vec{p}} L_1 \cdots L_n \delta_{\vec{k}_{\vec{p}}, \vec{k}_{\vec{q}}} \delta^{(m)}(\vec{p} - \vec{q}) \tag{4.2}$$

gives a field that obeys the usual canonical commutation relation

$$[\phi(x), \Pi(y)]_{x^0 = y^0} = i\delta^{(n+m)}(\vec{x} - \vec{y}). \tag{4.3}$$

Further, the total momentum in the field is

$$P^\mu = \sum_{\vec{k}\in\mathbb{Z}^n} \frac{1}{(2\pi)^n L_1 \cdots L_n} \int \frac{d^m p}{(2\pi)^m} \frac{1}{2E_{\vec{p}}} p^\mu a^\dagger(\vec{p}) a(\vec{p}), \tag{4.4}$$

and hence we have the usual interpretation of an excitation of a mode of the field as a particle of mass m and momentum $\vec{p}$.

Of crucial importance, one may compute the contraction

$$\overbrace{\phi(x)\phi(y)} = \sum_{\vec{k}\in\mathbb{Z}^n} \frac{1}{(2\pi)^n L_1 \cdots L_n} \int \frac{d^m p}{(2\pi)^m} \int \frac{dp^0}{2\pi} e^{-i\,p\cdot(x-y)} \frac{i}{p^2 - m^2 + i\varepsilon}. \tag{4.5}$$

4.2 LO Scattering

We may straightforwardly compute the LO scattering amplitude in the usual way. Since we're working at leading order, we don't need to consider any subtleties due to finite system size corrections to LSZ reduction; the asymptotic states are trivially the single particle states of the free theory. Thus the $\mathcal{T}$ matrix can be readily found to be

$$\begin{aligned}
&\langle p_1 p_2 | T | p_A p_B \rangle \\
&\quad = -i\,\lambda \int d^{m+n+1} z e^{i\,z\cdot(p_A + p_B - p_1 - p_2)} + \mathcal{O}(\lambda^2) \\
&\quad = -i\,\lambda\, 2\pi\delta(p_A^0 + p_B^0 - p_1 - p_2) \\
&\qquad \times (2\pi)^m \delta^{(m)}(\vec{p}_A + \vec{p}_B - \vec{p}_1 - \vec{p}_2) \\
&\qquad \times (2\pi)^n L_1 \cdots L_n \delta_{\vec{\ell}_{p_A} + \vec{\ell}_{p_B}, \vec{\ell}_{p_1} + \vec{\ell}_{p_2}} + \mathcal{O}(\lambda^2),
\end{aligned} \tag{4.6}$$

where the m Dirac deltas provide the spatial momentum conservation in the directions of infinite extent of the momenta to be the same and the n Kronecker deltas provide the spatial momentum conservation in the directions of finite extent. There is also an overall Dirac delta providing energy conservation. Note that even if we work in a spacetime that is fully compact in the spatial directions, energy conservation is given by a Dirac delta function as we've assumed that the extent of the time direction is infinite. Note further that we will at times consider (unphysical) momenta in the finite spatial directions that are not integer modes but that the Kronecker deltas associated with momentum conservation in those directions are only non-zero when the modes are properly integer.

The choice of allowing time to flow from $-\infty$ to $+\infty$ is perhaps somewhat inconsistent with the spirit of a scattering experiment one might imagine in a finite space. In infinite space, a scattering experiment consists of wavepackets that start off infinitely separated in the infinite past that are allowed to propagate to definite momentum states in the infinite future [22]. Implicitly, in this infinite volume picture, the particles interact at a time $t \sim 0$ only. There are two pathologies in the finite volume case when all spatial dimensions are finite: first, the wavepackets can never be infinitely separated; second, the particles interact an infinite number of times. The issue of initial separation isn't an issue at leading order because there's no renormalisation; beyond leading order, so long as the space is large compared to the interaction length, the wavepackets can be considered well separated. Further, the NLO contribution to the one particle irreducible self energy diagram will remain independent of the particle's momentum; hence at NLO, wavefunction renormalisation is still trivial. That the particles interact an infinite number of times over an infinite time interval will be reflected in an infinite total cross section.

One could alternatively consider a finite time for propagation, for example of the order of the size of the system. However, the integral over z^0 in Eq. (4.6) then yields a complicated expression that only converges to a Dirac delta function in the limit of the time for propagation going to infinity. Then the subsequent calculation of the NLO contribution is sufficiently far away from usual scattering problems or a thermal field theoretic calculation that its utility appears limited.

4.3 NLO Scattering

If we now restrict ourselves to three periodic spatial directions and no spatial directions of infinite extent, $n = 3$ and $m = 0$, one may immediately write down the quantity we need to evaluate for the NLO correction to $2 \to 2$ scattering:

$$V(p^2, \{L_i\}; \mu, \epsilon) = -\frac{1}{2} \int_0^1 dx \int \frac{d\ell_E^0}{2\pi} \sum_{\vec{k} \in \mathbb{Z}^3} \frac{1}{(2\pi)^3 L_1 L_2 L_3} \frac{\mu^{2\epsilon}}{[\ell_E^2 + \Delta^2]^{2+\epsilon}}, \tag{4.7}$$

where $\Delta^2 \equiv -x(1-x)p^2 + m^2 - i\varepsilon$ and $\ell_E^\mu = (\ell_E^0, \frac{k^i}{L_i} + x\, p^i)^\mu$. Notice that in contrast to the infinite volume case we cannot simply shift the spatial integration to remove the

$+xp^i$ shift in ℓ_E^μ. As in Chapter 3 we may evaluate the ℓ_E^0 integral to find

$$V(p^2,\{L_i\};\mu,\epsilon) = -\frac{1}{2}\frac{1}{2\pi}\frac{1}{(2\pi)^3 L_1 L_2 L_3}\int_0^1 dx \times \frac{\sqrt{\pi}\Gamma\left(\frac{3}{2}+\epsilon\right)}{\Gamma(2+\epsilon)}\sum_{\vec{k}\in\mathbb{Z}^3}\frac{\mu^{2\epsilon}}{\left(\sum_{i=1}^3\left(\frac{k^i}{L_i}+xp^i\right)^2+\Delta^2\right)^{\frac{3}{2}+\epsilon}}. \quad (4.8)$$

Our result includes a generalised Epstein zeta function [65],

$$\zeta(\{a_i\},\{b_i\},c;s) \equiv \sum_{\vec{n}\in\mathbb{Z}^p}\left[a_i^2 n_i^2 + b_i n_i + c\right]^{-s}, \quad (4.9)$$

where repeated indices are implicitly summed over. The generalised Epstein zeta function converges for $s > d$. As per usual we wish to isolate the pole occurring at $s = d$ and determine the finite remainder. To do so, we utilise the Poisson summation formula to provide an analytic continuation of the generalised Epstein zeta function; we detail the derivation in App. B. We can first write V in terms of a lattice sum over Λ^*, the lattice with spacings given by $\{L_i^{-1}\}$ to get

$$V(p^2,\Lambda;\mu,\epsilon) = -\frac{|\Lambda^*|}{2(2\pi)^4}\frac{\sqrt{\pi}\Gamma\left(\frac{3}{2}+\epsilon\right)}{\Gamma(2+\epsilon)}\int_0^1 dx\,\mu^{2\epsilon}\zeta\left(\Lambda^*, x\vec{p}, \Delta^2, \frac{3}{2}+\epsilon\right), \quad (4.10)$$

where we have written

$$\zeta(\Lambda,\vec{\delta},c;s) = \sum_{\vec{k}\in\Lambda}\left[(\vec{k}+\vec{\delta})^2 + c\right]^{-s}. \quad (4.11)$$

Noting that $(\Lambda^*)^* = \Lambda$ such that $|\Lambda^*| \times |(\Lambda^*)^*| = 1$, we can then apply Eq. (B.18) to find

$$V(p^2,\Lambda;\mu,\epsilon) = -\frac{1}{2(2\pi)^4}\frac{\sqrt{\pi}\Gamma\left(\frac{3}{2}+\epsilon\right)}{\Gamma(2+\epsilon)}\int_0^1 dx\,\mu^{2\epsilon}\frac{2\pi^{\frac{3}{2}}}{\Gamma\left(\frac{3}{2}+\epsilon\right)}(\Delta^2)^{-\epsilon} \left[\Gamma(\epsilon) + {\sum_{\ell\in\Lambda}}' \cos(2\pi x\vec{\ell}\cdot\vec{p})\left(\frac{\|\vec{\ell}\|}{\Delta^2}\right)^{\epsilon} K_{-\epsilon}(2\pi\|\vec{\ell}\|\sqrt{\Delta^2})\right]. \quad (4.12)$$

One may find similar expressions using Eq. (B.18) for different numbers of total spatial dimensions; for $n < 3$ there's no divergence.

Using our modified $\overline{\text{MS}}$ convention, the renormalised NLO contribution to $2 \to 2$ scattering in 3 periodic spatial dimensions is

$$\overline{V}(p^2,\Lambda;\mu) = -\frac{1}{2}\frac{1}{(4\pi)^2}\int_0^1 dx\left\{\ln\frac{\mu^2}{\Delta^2} + 2{\sum_{\vec{\ell}\in\Lambda}}' \cos(2\pi x\vec{\ell}\cdot\vec{p})K_0\left(2\pi\|\vec{\ell}\|\sqrt{\Delta^2}\right)\right\}, \quad (4.13)$$

or equivalently as an explicit sum over integer vectors

$$\overline{V}(p^2, \{L_i\}; \mu) = -\frac{1}{2}\frac{1}{(4\pi)^2}\int_0^1 dx \Bigg\{ \ln\frac{\mu^2}{\Delta^2} + 2\sum_{\vec{m}\in\mathbb{Z}^3}{}' \cos\Big(2\pi x \sum m_i p^i L_i\Big) K_0\Big(2\pi\sqrt{\Delta^2 \sum m_i^2 L_i^2}\Big)\Bigg\}, \quad (4.14)$$

and the counterterm is unchanged from the infinite volume case.

In principle Eq. (4.13) should apply to any 3 dimensional spatial geometry that discretises momentum space into some lattice Λ^*.

Since asymptotically $K_0(z) \sim \exp(-z)/\sqrt{z}$ we see that the finite system size corrections naturally go to zero as the system size grows. Notice further that the UV divergence is unaffected by the finite system size corrections. We should have expected this lack of sensitivity of the UV divergence to the finite system size, since a finite system size acts as an IR cutoff; the infinitely small distances probed at the infinite UV are insensitive to the global existence of any boundary conditions for the manifold (effectively) infinitely far away. As a result, a leading logarithmic analysis such as from an application of the Callan-Symanzik equation won't be able to capture the finite system size effects on the running coupling; rather, we must explicitly perform the resummation of the 1PI diagrams to see the subleading $1/L$ corrections to the running coupling. Even though this analysis is subleading log in the limit of large p, we're interested in the momentum region in which the finite system size effects aren't vanishingly small; i.e., we're interested in the case of $p \lesssim 1/L$.

The disappearance of the corrections as the system size goes to infinity is a reassuring self-consistency check. Next we will ensure that our calculations has left unitarity intact in Chapter 5.

Chapter 5

Unitarity Check

We can check the consistency of our finite system size corrections against the optical theorem: one should find self-consistently that the time evolution captured up to NLO is unitary. For self-consistency, then, we should find that

$$2\,\mathrm{Im}\,\mathcal{M} = \sigma_{\mathrm{tot}}. \tag{5.1}$$

We have already shown that unitarity holds in the infinite volume limit with $m = 3$ spatial dimensions of infinite extent and $n = 0$ spatial dimensions of finite extent in Chapter 2. We will show that unitarity holds as we increase n incrementally to 3. However, instead of rederiving $\overline{V}$ for each case, we may simply take the appropriate number of $L_i \to \infty$. Since the modified Bessel function of the second kind decreases exponentially with its argument, for each i for which $L_i \to \infty$ we may take the iterator $k_i \equiv 0$[1].

In general, the left hand side of Eq. (5.1) yields

$$2\,\mathrm{Im}\,\mathcal{M} = -2\lambda^2\,\mathrm{Im}\left(\overline{V}(s,\{L_i\};\mu) + \overline{V}(t,\{L_i\};\mu) + \overline{V}(u,\{L_i\};\mu)\right), \tag{5.2}$$

where $\overline{V}(p^2,\{L_i\};\mu)$ is given by Eq. (4.14). As noted in App. B, one may organise the sum for the finite system size correction such that the phases are only cosines. Therefore the only contribution to the imaginary part of the amplitude may come from values of x

[1]There is a slight subtlety here. We will see that for configurations such that all outgoing momenta are in the finite spatial directions the amplitude diverges (since the particles interact an infinite number of times). These "geometric bound states" only occur for countably discrete number of momentum configurations, so the limit of the finite system size correction going to the infinite volume result will hold everywhere but on a set of measure zero.

such that $\Delta^2 < 0$, in which case there are contributions from evaluating the logarithm of negative numbers and from evaluating the modified Bessel function for arguments with an imaginary part. Since t and u are non-positive, we therefore have that $\mathrm{Im}\,\mathcal{M}$ only comes from $\overline{V}(s, \{L_i\}; \mu)$. We will in general work in the centre of mass frame, in which case $p^i = 0$ for the s channel $\overline{V}(s, \{L_i\}; \mu)$. Recall from the infinite volume case reviewed in Chapter 2 that $\mathrm{Re}\,\Delta^2 < 0$ for $s > 4m^2$ and $x_- < x < x_+$, where $0 < x_\pm < 1$ are given by Eq. (2.13). As was done in the infinite volume review, we self-consistently align the branch cuts of arg, log, K_0, and the square root along the negative real axis. Then the small imaginary part from the propagators in the loop means that for $s > 4m^2$ and $x_- < x < x_+$ we have that Δ^2 is in the third quadrant of the complex plane; thus $\sqrt{\Delta^2}$ is in the fourth quadrant of the complex plane. Therefore for $x_- < x < x_+$ we have, for $\Delta^2 \equiv -x(1-x)s + m^2 - i\varepsilon$

$$\begin{aligned}\mathrm{Im}\, K_0\big(2\pi\sqrt{\Delta^2 \sum m_i^2 L_i^2}\big) &= \mathrm{Im}\, K_0\big(\varepsilon - 2\pi i|\Delta|\sqrt{\sum m_i^2 L_i^2}\big) \\ &= \frac{\pi}{2} J_0\big(2\pi|\Delta|\sqrt{\sum m_i^2 L_i^2}\big), \end{aligned} \tag{5.3}$$

where J_0 is the usual Bessel function of the first kind, and we've dropped the irrelevant terms linear and higher order in ε on the right hand side (and can take $|\Delta| = x(1-x)s - m^2$).

Defining $\tilde{Q} \equiv \sqrt{1 - (4m^2/s)}$ we have

$$\begin{aligned} 2\,\mathrm{Im}\,\mathcal{M} &= \frac{\lambda^2}{16\pi}\tilde{Q}\theta(\tilde{Q}^2)\left[1 + \frac{1}{\tilde{Q}}\sum_{\vec{m}\in\mathbb{Z}^n}{}' \int_{x_-}^{x^+} dx\, J_0(2\pi|\Delta|\sqrt{\sum m_i^2 L_i^2})\right] \\ &= \frac{\lambda^2}{16\pi}\tilde{Q}\theta(\tilde{Q}^2)\left[1 + \sum_{\vec{m}\in\mathbb{Z}^n}{}' \int_0^1 dv\, J_0(\pi\sqrt{s\sum m_i^2 L_i^2}\tilde{Q}\sqrt{1-v^2})\right] \\ &= \frac{\lambda^2}{16\pi}\tilde{Q}\theta(\tilde{Q}^2) \sum_{\vec{m}\in\mathbb{Z}^n} \mathrm{sinc}(\pi\sqrt{s\sum m_i^2 L_i^2}\tilde{Q}) \\ &= \frac{\lambda^2}{16\pi}\tilde{Q}\theta(\tilde{Q}^2) \sum_{\vec{\tilde{m}}\in\Lambda^n} \mathrm{sinc}(\pi\sqrt{s}\tilde{Q}|\vec{\tilde{m}}|). \end{aligned} \tag{5.4}$$

In the first line, the 1 in the square brackets is the contribution from $\int dx\, \mathrm{Im}\, \ln \mu^2/\Delta^2$; we have also already taken the imaginary part of the K_0 Bessel function. In the second line we defined the new variable $v \equiv (2x-1)/\tilde{Q}$ and exploited the symmetry of the integrand about $v = 0$. In the third line we evaluated $\int_0^1 dv J_0(a\sqrt{1-v^2}) = \mathrm{sinc}(a)$ [66].

In the fourth line, sinc is the usual unnormalised sinc function,

$$\mathrm{sinc}(x) \equiv \frac{\sin(x)}{x}. \tag{5.5}$$

In the last line, we exchanged the sum over integers $\vec{m}$ (which are weighted by L_i^2 in the summand) with a sum over the lattice Λ^n defined by the n lengths L_i. We make this last change to a sum over a lattice in anticipation of exploiting the Poisson summation formula over lattices [67]. The Poisson summation over lattices is given by

$$\sum_{\vec{\tilde{m}}\in\Lambda^n} f(\vec{\tilde{m}}) = \frac{1}{\det\Lambda} \sum_{\vec{\tilde{k}}\in\Lambda^{*n}} \tilde{F}(\vec{\tilde{k}}), \tag{5.6}$$

where Λ^* is the lattice dual to Λ and $\tilde{F}$ is the usual Fourier transform of f,

$$\tilde{F}(\vec{\tilde{k}}) \equiv \int d^n m\, e^{2\pi\, i\, \vec{k}\cdot\vec{m}} f(\vec{\tilde{m}}). \tag{5.7}$$

Following exactly the method of performing the n dimensional Fourier transform as shown in App. B with now $f(\vec{\tilde{m}}) = \mathrm{sinc}(\pi\sqrt{s}\tilde{Q}|\vec{\tilde{m}}|)$, we have that

$$\begin{aligned}\tilde{F}(\vec{\tilde{k}}) &= \Omega_{n-2}\sqrt{\pi}\frac{\Gamma\left(\frac{n-1}{2}\right)}{\Gamma\left(\frac{n}{2}\right)} \int_0^\infty \tilde{m}^{n-1} d\tilde{m}\, \mathrm{sinc}(\pi\sqrt{s}\tilde{Q}\tilde{m})\, {}_0F_1(;\, \frac{n}{2};\, -(\pi\tilde{k}\tilde{m})^2) \\ &= \Omega_{2-n}\big(\frac{s}{4}\tilde{Q}^2 - \tilde{k}^2\big)^{\frac{1-n}{2}}\theta\big(\frac{s}{4}\tilde{Q}^2 - \tilde{k}^2\big).\end{aligned} \tag{5.8}$$

Thus

$$2\,\mathrm{Im}\,\mathcal{M} = \frac{\lambda^2}{2(4\pi)^2\sqrt{s}}\theta(\tilde{Q}^2)\Omega_{2-n}\frac{1}{\prod L_i}\sum_{\vec{\tilde{k}}\in\Lambda^{*n}} \big(\frac{s}{4}\tilde{Q}^2 - \tilde{k}^2\big)^{\frac{1-n}{2}}\theta\big(\frac{s}{4}\tilde{Q}^2 - \tilde{k}^2\big). \tag{5.9}$$

Consider now the total cross section,

$$\begin{aligned}\sigma_{\mathrm{tot}} = \frac{1}{2}\sum_{\vec{k}_1\in\mathbb{Z}^n} \frac{1}{(2\pi)^n\prod L_i}\int\frac{d^m p_1}{(2\pi)^m 2E_1} \sum_{\vec{k}_2\in\mathbb{Z}^n}\frac{1}{(2\pi)^n\prod L_i}\int\frac{d^m p_2}{(2\pi)^m 2E_2} \\ \times\lambda^2(2\pi)^4\prod L_i\delta(p_A^0 + p_B^0 - p_1^0 - p_2^0)\delta^{(m)}(\vec{p}_A + \vec{p}_B - \vec{p}_1 - \vec{p}_2)\delta^{(n)}_{\vec{k}_A+\vec{k}_B,\vec{k}_1+\vec{k}_2}.\end{aligned} \tag{5.10}$$

We may immediately collapse the p_2 integrals with the Dirac delta functions and the k_2

sums with the Kronecker deltas. Then

$$\begin{aligned}\sigma_{\text{tot}} &= \frac{\lambda^2}{2(2\pi)^2}\sum_{\vec{k}_1\in\mathbb{Z}^n}\frac{1}{\prod L_i}\int\frac{d^m p_1}{(2E_1)^2}\times\delta(\sqrt{s}-2\sqrt{p_1^2+\sum\frac{k_i^2}{L_i^2}+m^2}) \\ &= \frac{\lambda^2}{2(4\pi)^2\sqrt{s}}\theta(\tilde{Q}^2)\Omega_{m-1}\frac{1}{\prod L_i}\sum_{\vec{k}\in\mathbb{Z}^n}\big(\frac{s}{4}\tilde{Q}^2-\sum k_i^2L_i^2\big)^{\frac{m-2}{2}}\theta\big(\frac{s}{4}-m^2-\sum k_i^2L_i^2\big) \\ &= \frac{\lambda^2}{2(4\pi)^2\sqrt{s}}\theta(\tilde{Q}^2)\Omega_{2-n}\frac{1}{\prod L_i}\sum_{\vec{\tilde{k}}\in\Lambda^{*n}}\big(\frac{s}{4}\tilde{Q}^2-\vec{\tilde{k}}^2\big)^{\frac{1-n}{2}}\theta\big(\frac{s}{4}\tilde{Q}^2-\vec{\tilde{k}}^2\big). \qquad (5.11)\end{aligned}$$

In the second line we integrate out the Dirac delta function. In the third line, we use $n+m=3$ to set $m=3-n$ and also change the sum over the integers to a sum over the lattice dual to the lattice from Eq. (5.4).

One can readily see that Eqs. (5.9) and (5.11) are equal, and therefore the optical theorem (i.e. unitarity) is satisfied for our newly derived result for $n = 0, 1, 2,$ or 3 compact spatial dimensions of lengths $\{L_i\}$.

We provide an alternative check on unitarity for Eq. (4.14) for $n = 2$ or 3 compact spatial dimensions that utilises a novel generalisation of a conjectured identity from Ramanujan and Hardy involving the square counting function [68] in App. C.

Chapter 6

Sample Plots of $\overline{V}$

We would like to have some sense of the scale and type of correction due to the presence of the finite size of the system; in particular, we would like to compare the magnitude and sign of the contribution that remains when all lengths are taken to infinity to the magnitude and the sign of the contribution that goes to zero smoothly as all lengths are taken to infinity.

Since the full result we derived earlier for $2 \to 2$ scattering Eq. (4.14) captures both the infinite volume and finite volume contributions, and we may take any one or more finite lengths to infinity, we will do so now. In particular, since the modified Bessel function of the second kind decays exponentially for large argument, for any length L_i taken to infinity, we may simply take only the $m_i = 0$ contribution associated with that length to find the result for only $n = 1$ or 2 compact directions.

If we restrict ourselves to considering only $n = 1$ or 2, then we may avoid any questions about the applicability of or corrections to the usual LSZ and Gell-Mann–Low formalisms [22, 69] associated with scattering in quantum field theories so long as we have our incoming (outgoing) particles come from one of the directions of infinite length. It is important to consider that in compactified directions the physical momentum modes are discretised, so instead of considering scattering angles in the finite directions, we consider the mode number instead.

In general, one may straightforwardly evaluate Eq. (4.14) by brute force for $p^2 < 0$,

i.e. for the t or, equivalently, the u channel contribution to the amplitude. In addition to the obvious numerical check of doubling the number of terms included in the sum and verifying that the results are unchanged, we further confirm that the brute force method is accurate by comparing to an asymptotic analytic analysis in Chapter 7.

The numerics are significantly more difficult in the s channel, since the integral over x yields both positive and negative values of the argument of the modified Bessel function. As a result, the s channel has both real and imaginary parts. One may show that the imaginary part is straightforward and involves only a sum of a finite number of terms. The real part involves an infinite sum over oscillating (not modified) Bessel functions. For one compact dimension, one may make significant analytic progress on the s channel. Using

$$\mathrm{Re}\, K_0(-x - i\varepsilon) = -\frac{\pi}{2} Y_0(x), \qquad x > 0, \tag{6.1}$$

and

$$\int_0^z Y_0(\sqrt{z^2 - x^2})dx = \frac{2}{\pi}\big[\,\mathrm{Ci}(z)\sin(z) - \mathrm{Si}(z)\cos(z)\big], \tag{6.2}$$

where Y_0 is the usual Bessel function of the second kind, $\mathrm{Ci}(x)$ is the usual cosine integral, and $\mathrm{Si}(x)$ is the usual sine integral[1], and noting that $p_i \equiv 0$ in the s channel. We then have that the real part of the finite volume contribution is

$$\begin{aligned}\mathrm{Re}\,\overline{V}_{\mathrm{fin}}(s,\, L;\, \mu) = 4\sum_{\ell=1}^{\infty}\Bigg[2\int_0^{x_-} K_0\big(2\pi\,\ell\, L\sqrt{-4x(1-x)E^2 + m^2}\big)dx \\ + \frac{1}{2\pi\, L\, E\,\ell}\Big(\,\mathrm{Ci}\big(2\pi\,\ell\, L q\big)\sin(2\pi\,\ell\, L q) - \mathrm{Si}\big(2\pi\,\ell\, L q\big)\cos(2\pi\,\ell\, L q)\Big)\Bigg],\end{aligned} \tag{6.3}$$

where $s = 4E^2$ and $q \equiv \sqrt{(s - 4m^2)}$. The integral over the modified Bessel function is numerically safe as the argument is pure real over $x \in (0, x_-)$. Then, from Eq. (5.4) and Eq. (C.7), we have that

$$\mathrm{Im}\,\overline{V}_{\mathrm{fin}}(s,\, L;\, \mu) = \pi\frac{q}{E}\Big(\frac{1}{2Lq} + \frac{\lfloor Lq\rfloor}{Lq} - 1\Big). \tag{6.4}$$

Although the cosine and sine integral special functions oscillate in Eq. (6.3), the overall $1/\ell$ factor leads to a numerically stable solution. In two (or more) compact dimensions,

[1]The integral over the Y_0 modified Bessel function may be derived by integrating its Frobenius expansion term by term and then performing the infinite sum.

a similar analysis as done to arrive at Eq. (6.3) yields a sum that does not behave well numerically for small q or L. A direct evaluation of Eq. (4.14) similarly does not yield a numerically convergent result.

In order to obtain plots of the real part of the s channel contribution in two compact dimensions, we tried to analytically perform the complete infinite sum first, then numerically evaluate the integral over x. In one compact dimension, one can factor out the iterator in the sum from the square root in the argument of the modified Bessel function. One may then perform the complete infinite sum by using a common integral representation of the modified Bessel function,

$$\begin{aligned}\sum_{\ell=1}^{\infty} K_0(\ell x) &= \sum_{\ell=1}^{\infty} \int_0^{\infty} e^{-\ell x \cosh t} dt \\ &= \int_0^{\infty} \frac{dt}{e^{x \cosh t} - 1}.\end{aligned} \tag{6.5}$$

However, in two compact dimensions, in order to perform the infinite sum one needs an integral representation of the modified Bessel function that, e.g., looks like the exponential of the square of the argument of the modified Bessel function. We were unable to find any such useful representations in the literature.

Rather, the method we found that could provide numerically stable results relied on a Kramers-Kronig type dispersion relation we derived relating the (derivative of the) real part of $\overline{V}(s)$ to the imaginary part of $\overline{V}(s)$. The detailed derivation and consistency checks of this result is outside the main scope of this work; we leave the details to App. D. We provide several sample plots for the cases of 1 and 2 compact dimensions in the following subsections.

6.1 One Compact Dimension

We will consider scattering in the centre of mass frame, where

$$\begin{aligned} p^i_{\text{in}} &= \left(\frac{n_i}{L}, 0, p_{\text{inf}}\right)^i \\ p^i_{\text{out}} &= \left(\frac{n_f}{L}, \sin(\theta)p_{\text{inf},\,f}, \cos(\theta)p_{\text{inf},\,f}\right)^i \\ p_{\text{inf},\,f} &\equiv \sqrt{p^2_{\text{inf}} + \frac{n_i^2 - n_f^2}{L}}, \end{aligned} \tag{6.6}$$

where n_i, $n_f \in \mathbb{Z}$ are the number of modes in the compact dimension such that the Mandelstam variables are given by

$$\begin{aligned} s &= 4(m^2 + \vec{p}^{\,2}_{\text{in}}) \\ t &= -(\vec{p}_{\text{in}} - \vec{p}_{\text{out}})^2 \\ u &= -(\vec{p}_{\text{in}} + \vec{p}_{\text{out}})^2. \end{aligned} \tag{6.7}$$

6.1.1 s Channel

We use Eqs. (D.5) and (D.30) to obtain

$$\begin{aligned} \overline{V}_1(s, L; \mu) = -\frac{1}{32\pi^2}\Bigg[&\ln\left(\frac{\mu^2}{m^2}\right) + a_1(Lm) \\ &+ \sum_{l=-\infty}^{\infty}\left(\frac{2}{L}\frac{\operatorname{arctanh}\left(\frac{L}{2}\sqrt{\frac{s+i\varepsilon}{(Lm)^2+l^2}}\right)}{\sqrt{s+i\varepsilon}} - \frac{1}{\sqrt{l^2+(Lm)^2}}\right)\Bigg], \end{aligned} \tag{6.8}$$

where a_1 is given by Eq. (D.29).

We show a comparison between the infinite volume contribution to $\overline{V}_1(s, L, \mu)$ and the finite volume contribution when one of the three directions is finite as a function of p_{inf} in Fig. 6.1 and as a function of L in Fig. 6.2 for the s channel. Note that the centre of mass energy depends only on the magnitude of the incoming (equivalently outgoing) momentum, and not the scattering angle; thus we only plot against the value of the incoming finite system size momentum mode n_i. We take $\mu = 1$ GeV and $m = 0.5$ GeV. For the scan in p_{inf} we take $L = 1/\sqrt{3}$ GeV^{-1} and for the scan in L we take $p_{\text{inf}} = 1$ GeV. For the scan in p_{inf}, the length $L \sim 0.1$ fm is rather small phenomenologically; however, the value is useful for illustrative purposes. For $s > 4m^2 \Leftrightarrow |\vec{p}| > 0$, both the infinite

volume and finite volume corrections have non-vanishing imaginary parts.

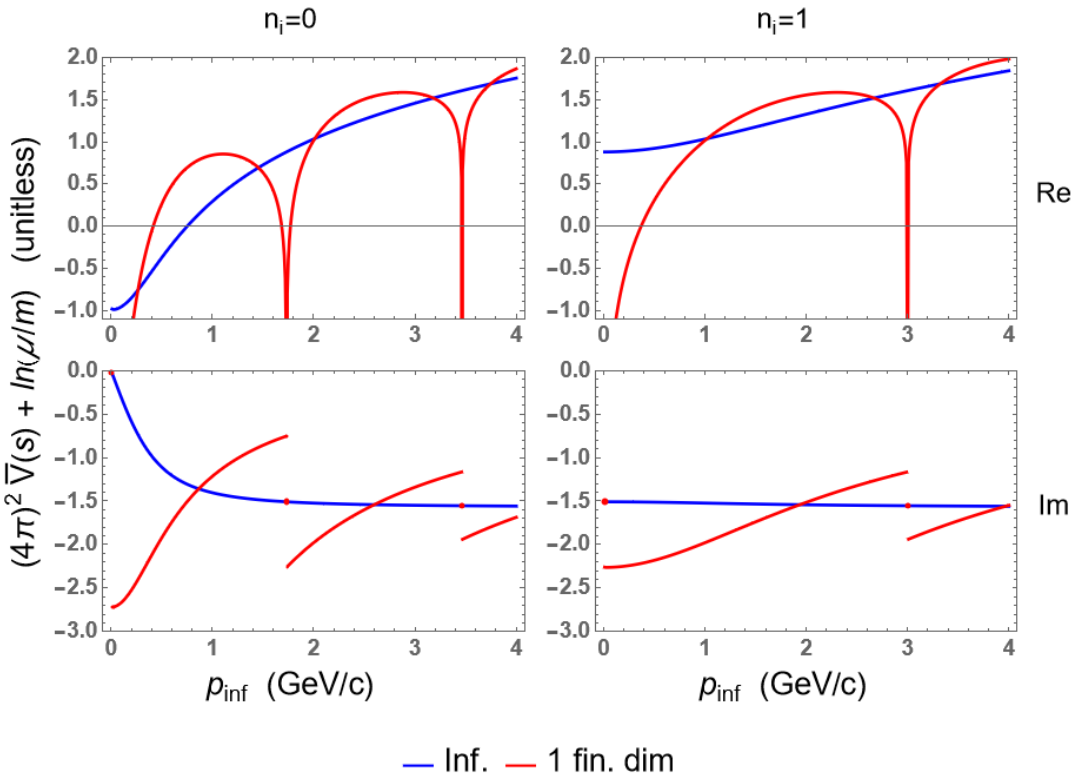

Figure 6.1: A plot of the infinite volume (blue) and finite length (red) real part (top) and imaginary part (bottom) of $\overline{V}_1(s, p_{\text{inf}}, \mu)$ as a function of p_{inf} for 1 compact dimension; left has no initial momentum in the compact direction, and right has one mode in the compact direction. $\mu = 1$ GeV, $m = 0.5$ GeV, and $L = 1/\sqrt{3}$ GeV^{-1}.

One can see that the finite system size correction does indeed converge to zero as either $|\vec{p}| \to \infty$ or $L \to \infty$. However, the convergence is non-trivial. For $|\vec{p}| \times L$ integer, the finite system size correction to the real part of $\overline{V}_1(s, L, \mu)$ receives a contribution from a term proportional to $-\operatorname{arctanh}(1) = -\infty$, while one can show that the finite system size correction to the imaginary part is identically zero at these integer values of $|\vec{p}| \times L$. Further, the imaginary part is discontinuous across values of $|\vec{p}| \times L$ integer due to the floor function in Eq. (C.7). Thus for large argument, the convergence of the correction to zero is only almost everywhere.

We can interpret the divergences in the real part of $\overline{V}_1(s, L, \mu)$ in the s-channel as due to "geometric bound states," in which *all* the momentum of each of the outgoing particles is in the finite direction. Since all the momentum is in the finite direction, the particles propagate back and forth a divergent number of times in the finite direction,

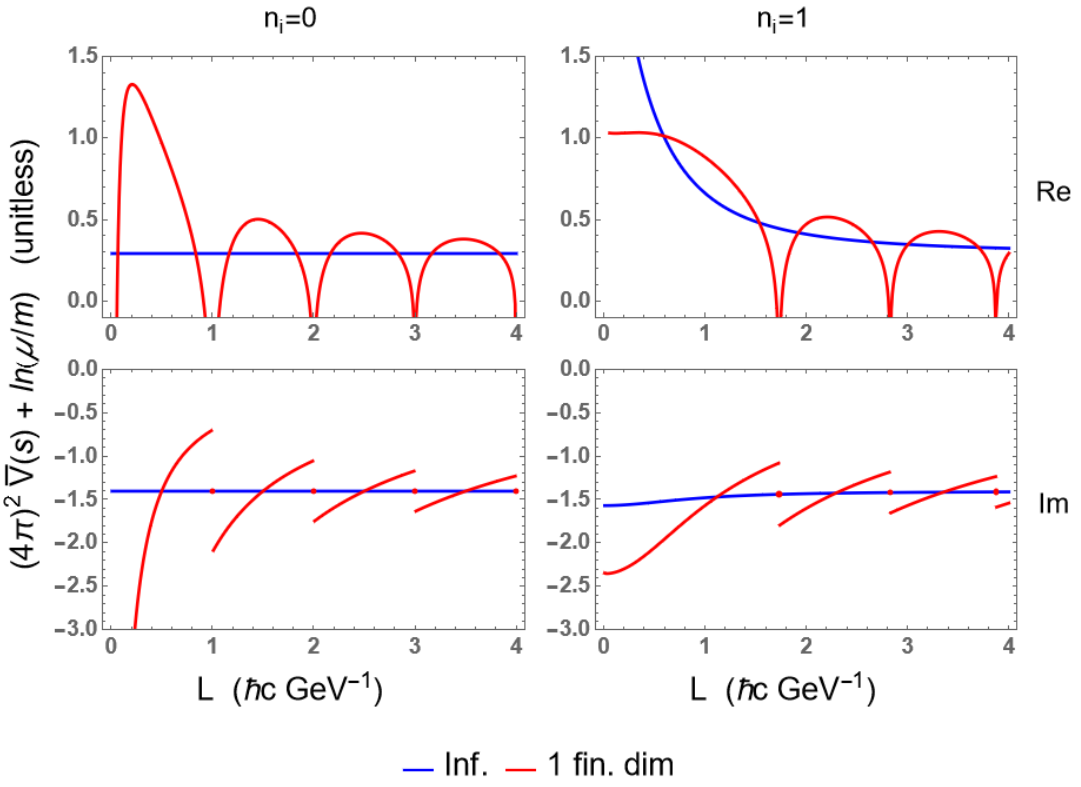

Figure 6.2: A plot of the infinite volume (blue) and finite length (red) real part (top) and imaginary part (bottom) of $\overline{V}_1(s, L, \mu)$ as a function of L for 1 compact dimension; left has no initial momentum in the compact direction, and right has one mode in the compact direction. $\mu = 1$ GeV, $m = 0.5$ GeV, and $p_{\text{inf}} = 1$ GeV.

with a divergent number of interactions over an arbitrarily long time. With such an *out* state, the particles take an arbitrarily long time to infinitely separate. Therefore the amplitude picks up a resonance associated with the particles being in a "geometric" bound state, with a corresponding pole in the S matrix as one is used to for more generic bound states.

It's important to note that as either $p_{\text{inf}} \to 0$ or $L \to 0$ the divergences in the amplitude are not due to a geometric bound state: in neither case is there enough momentum to fill the minimum mode in the finite direction. Rather, these IR-like divergences are precisely the effect of the small size of the system compared to the momentum ($p_{\text{inf}} \times L \ll 1$) we sought to capture in this work. We see, in fact, that the effect of placing the theory in a finite sized system *diverges* as the effective size of the system (as measured in the length units set by the momentum in the system) goes to zero, $p_{\text{inf}} \times L \ll 1$.

In particular, by noting that $s\,L^2/4 \to (Lm)^2 + n_i^2$ as $p_{\text{inf}} \to 0$, and that arctanh(1)

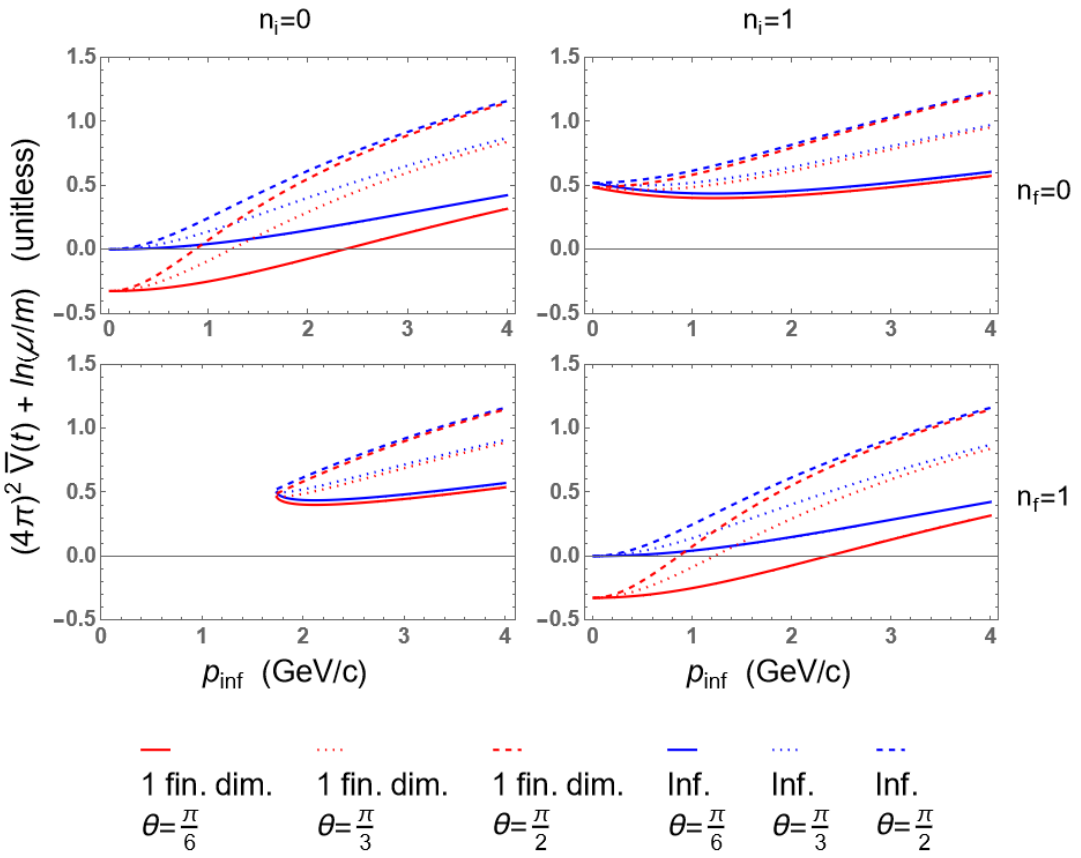

Figure 6.3: A plot of the infinite volume (blue) and finite length (red) $\overline{V}_1(t, p_{\text{inf}}, \mu)$ as a function of p_{inf} for $n = 1$ compact dimension for three values of the scattering angle θ among the two remaining infinite directions, $\theta = \pi/6$, $\pi/3$, and $\pi/2$, for solid, dotted, and dashed curves, respectively. The initial momentum has zero (one) modes in the finite direction in the left (right) column; the final momentum has zero (one) modes in the finite direction in the top (bottom) row. $\mu = 1$ GeV, $m = 0.5$ GeV, and $L = 1/\sqrt{3}$ GeV^{-1}.

diverges, one can easily show that the real part of Eq. (6.8) diverges (to negative infinity) for all $n_i \in \mathbb{Z}$. This behaviour can be seen in Fig. 6.1.

In order to fully understand the $L \to 0$ limit, we need a good handle on the asymptotics of a_1, which is non-trivial. We can however gain intuition from the observation that $s\,L^2/4 \to n_i^2$. If $n_i = 0$ then one finds a $(Lm)^{-1}$ divergence from the $l = 0$ term in Eq. (6.8). For $n_i > 0$, the only divergence may come from $a_1'(L\,m)$, where a_1' is given by Eq. (D.29) excluding the $l = 0$ term. One can see in Fig. 6.4 the divergences in the real and imaginary parts of $\overline{V}_1$ as $L \to 0$ for $n_i = 0$.

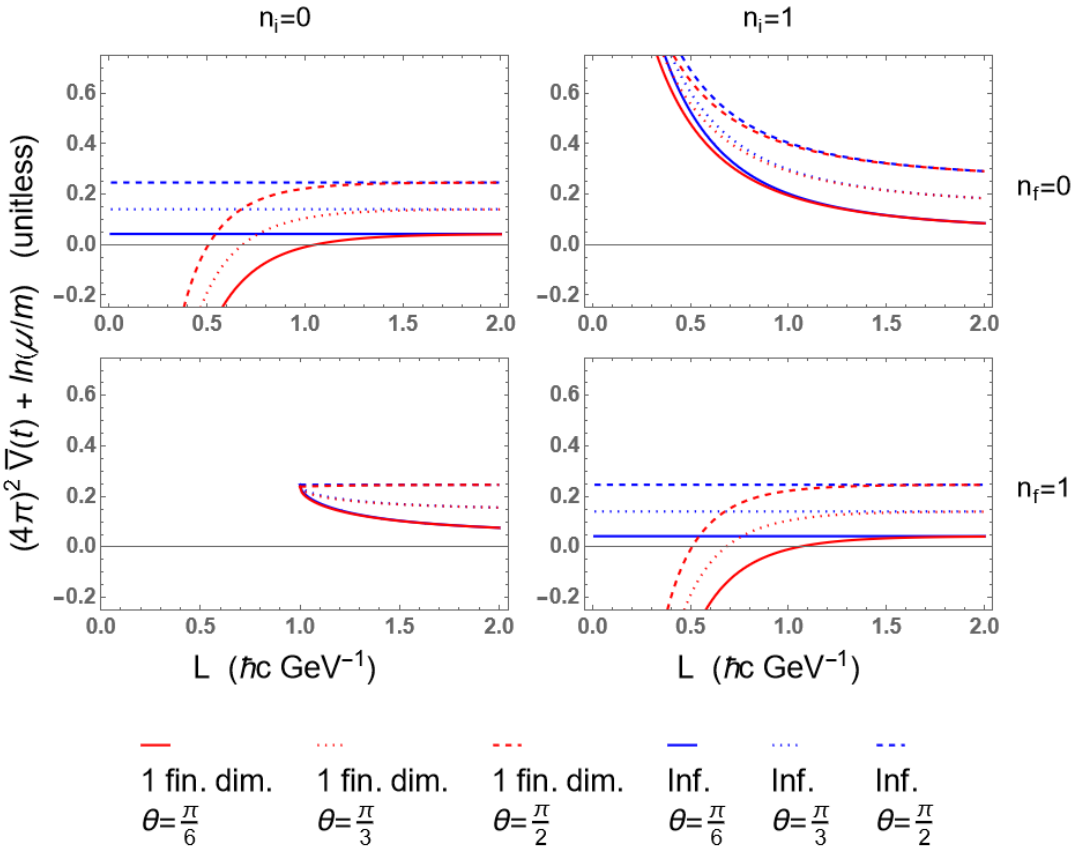

Figure 6.4: A plot of the infinite volume (blue) and finite length (red) $\overline{V}_1(t, L, \mu)$ as a function of p_{inf} for $n = 1$ compact dimension for three values of the scattering angle θ among the two remaining infinite directions, $\theta = \pi/6$, $\pi/3$, and $\pi/2$, for solid, dotted, and dashed curves, respectively. The initial momentum has zero (one) modes in the finite direction in the left (right) column; the final momentum has zero (one) modes in the finite direction in the top (bottom) row. $\mu = 1$ GeV, $m = 0.5$ GeV, and $p_{\text{inf}} = 1$ GeV.

6.1.2 t Channel

We show in Fig. 6.3,Fig. 6.4 a similar comparison as in Fig. 6.1,Fig. 6.2 respectively but for the t channel contribution for three values of scattering angle among the infinite directions $\theta = \pi/6$, $\pi/3$, and $\pi/2$. In this case, the convergence to zero of the finite system size correction is smooth as a function of either momentum or length going to infinity. If one, instead of fixing the modes in the finite direction, fix the scattering angle into the finite direction, and consider the discrete set of incoming momenta for which such a scattering angle is physical, one more clearly sees the slight oscillations from the phases in Eq. (4.14). The finite system size correction is finite for fixed L as $|\vec{p}| \to 0$ for $m > 0$; the non-zero mass sets an IR cutoff that limits the influence of the finite system

size correction. Not surprisingly, the finite system size correction becomes larger and larger, and subsequently more and more important, as L decreases; the finite system size correction diverges for fixed $|\vec{p}|$ as $L \to 0$. The non-trivial dependence of $\overline{V}$ on scattering angle θ implies that the effective coupling will also in general depend on the scattering angle θ.

In Fig. 6.3 and Fig. 6.4 for $n_i < n_f$ $\overline{V}_1$ ceases to exist below a certain p_{inf} or L since there is no way to maintain conservation of energy in these regions.

Fig. 6.4 shows a divergence to negative infinity for the finite volume correction as $L \to 0$ for the $n_i = 0 = n_f$ and the $n_i = 1 = n_f$ cases and a divergence to positive infinity for both the infinite volume and the finite system size $\overline{V}_1$ in the $n_i = 1$, $n_f = 0$ case. We may understand these divergences as follows. For $L \to 0$, $-t\,L/2 \to n_i(n_i - n_f)$. If $n_i \neq 0$ and $n_i \neq n_f$, then we must have that $t \to -\infty$ as $L \to 0$. Then one sees that the $-\ln \mu^2/\Delta^2$ term of Eq. (4.14) will diverge to positive infinity. Further the finite system size correction goes to zero as $K_0(z) \sim \exp(-z)/\sqrt{z}$ for $z \gg 1$, leading to the behaviour seen for $n_i = 1$ and $n_f = 0$ case in **??**. For $n_i = 0 = n_f$ and $n_i = 1 = n_f$, when $L \to 0$ we have that $-t < \infty$. In this case the log remains finite, but the argument of the K_0 modified Bessel function in Eq. (4.14) goes to 0, which leads to the divergence as $K_0(z) \sim \ln z$ for $z \ll 1$.

6.2 Two Compact Dimensions

We will consider scattering in the centre of mass frame, where

$$\begin{aligned} p^i_{\text{in}} &= \left(\frac{n_{1i}}{L}, \frac{n_{2i}}{L}, p_{\text{inf}}\right)^i \\ p^i_{\text{out}} &= \left(\frac{n_{1f}}{L}, \frac{n_{1f}}{L}, \sqrt{p^2_{\text{inf}} + \frac{n^2_{1i} - n^2_{1f}}{L} + \frac{n^2_{2i} - n^2_{2f}}{L}}\right)^i \end{aligned} \tag{6.9}$$

such that the Mandelstam variables are again given by

$$\begin{aligned} s &= 4(m^2 + \vec{p}_{\text{in}}^{\,2}) \\ t &= -(\vec{p}_{\text{in}} - \vec{p}_{\text{out}})^2 \\ u &= -(\vec{p}_{\text{in}} + \vec{p}_{\text{out}})^2. \end{aligned} \tag{6.10}$$

6.2.1 s Channel

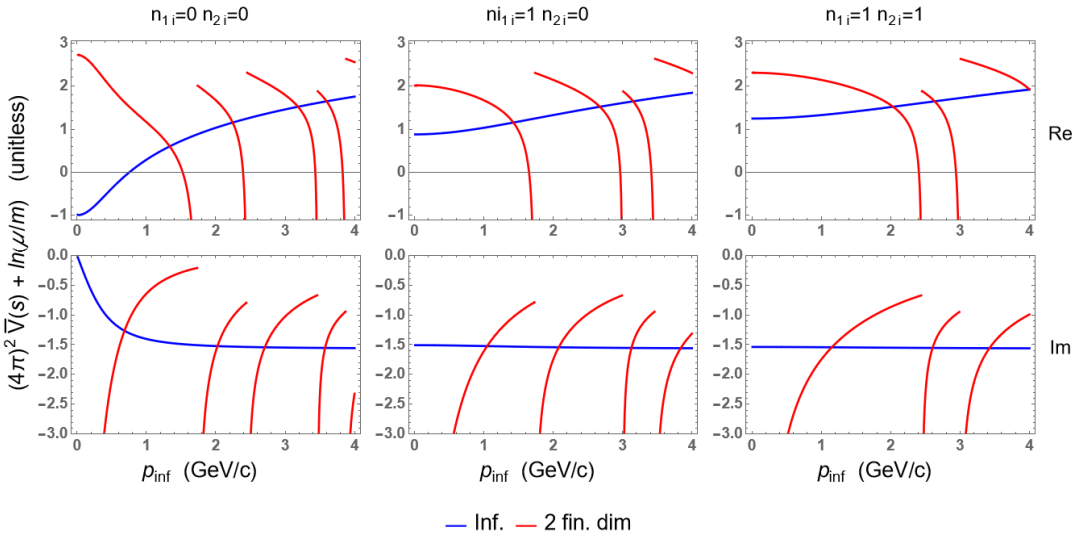

Figure 6.5: A plot of the infinite volume (blue) and finite length (red) real part (top) and imaginary part (bottom) of $\overline{V}_2(s, p_{\text{inf}}, \mu)$ as a function of p_{inf} for 2 compact dimensions. Left has no initial momentum in either of the compact directions, middle has one mode in one finite direction, and right has one mode in both compact directions. $\mu = 1$ GeV, $m = 0.5$ GeV, and $L = 1/\sqrt{3}$ GeV^{-1} for both compact directions.

We use Eqs. (D.5) and (D.36) to obtain

$$\begin{aligned} \overline{V}_2(s, L; \mu) = -\frac{1}{32\pi^2}\Bigg[&\ln\left(\frac{\mu^2}{m^2}\right) + a_2(Lm) \\ &+ \frac{1}{\pi}\sum_{l=0}^{\infty} r_2(l)\left(\frac{\frac{4}{L}\arcsin\left(\frac{L}{2}\sqrt{\frac{s+i\varepsilon}{(Lm)^2+l}}\right)}{\sqrt{s+i\varepsilon}\sqrt{4l - L^2(s-4m^2+i\varepsilon)}} - \frac{1}{l+(Lm)^2}\right)\Bigg], \end{aligned} \tag{6.11}$$

where $r_2(k)$ is the square counting function, which counts the number of 2D vectors $\vec{r}$ of integer components whose length is $|\vec{r}| = k$ (e.g. $r_2(0) = 1$, $r_2(1) = 4 = r_2(2)$), and a_2 is given by Eq. (D.35).

We show a comparison between the infinite volume contribution to $\overline{V}_2(s, L, \mu)$ and the finite volume contribution when two of the three directions are finite as a function

of p_{inf} in Fig. 6.5 and as a function of L in Fig. 6.6 for the s channel. Note again that the centre of mass energy depends only on the magnitude of the incoming (equivalently outgoing) momentum, and not the scattering angle. We take $\mu = 1$ GeV and $m = 0.5$ GeV. For the scan in p_{inf} we take $L = 1/\sqrt{3}$ GeV^{-1} and for the scan in L we take $p_{\text{inf}} = 1$ GeV.

One sees that—like the one compact dimension case—the real part of $\overline{V}$ diverges at particular values of $|\vec{p}| \times L$. For the two dimensional case, the imaginary part also diverges at these special values; also, the divergences are one-sided in the two dimensional case. Although difficult to see in Figs. 6.5 and 6.6, one may show that as either $|\vec{p}|$ or L goes to infinity, the finite system size correction converges almost everywhere to the infinite volume result. It's easiest to see the special values of $|\vec{p}|$ and L at which both the imaginary and real parts diverge from Eq. (6.11). When $r_2\left(\frac{1}{4}L^2(s-4m^2)\right) = r_2\left(\frac{1}{4}L^2|\vec{p}|^2\right) \neq 0$ the sum picks up a term that is divided by 0, giving a divergence; i.e. when $\frac{1}{4}L^2\,\vec{p}^{\,2}$ is an integer that can be written as the sum of two squares (or equivalently is the length of a 2D integer vector), $\overline{V}$ will diverge. When $r_2\left(\frac{1}{4}L^2|\vec{p}|^2\right) = 0$, the term falls outside of the sum over the lattice in the original expression, and the contribution is identically 0.

We can also see in the figures that the divergences are one-sided for the real and imaginary parts, and that the divergences are from the opposite directions in the real and imaginary parts. We may understand this one-sided divergence behaviour by considering the square root in the denominator of Eq. (6.11). Suppose a particular L_*, s_*, and l_* exist such that $4l_* - L_*^2(s_* - 4m^2 + i\varepsilon) = 0$. Now if $L \lesssim L_*$ (or, equivalently, $s \lesssim s_*$), then at l_* the argument of the square root is nearly zero and positive. Thus $\overline{V}_2$ will pick up a large real part. But if we rather have that $L \gtrsim L_*$ (or, equivalently, $s \gtrsim s_*$), then at l_* the argument of the square root is nearly zero and negative. Thus $\overline{V}_2$ will pick up a large imaginary part. We may use this reasoning further to understand the $p_{\text{inf}} \to 0$ behaviour seen in Fig. 6.5. As $p_{\text{inf}} \to 0$, $s \to 4m^2$. As $s \to 4m^2$, the $\sqrt{4l - L^2(s - 4m^2 + i\varepsilon)}$ denominator in Eq. (6.11) becomes very small and imaginary for $l = 0$ (and only $l = 0$), which leads to the real (imaginary) part of $\overline{V}_2$ going to a constant (diverging) as $p_{\text{inf}} \to 0$.

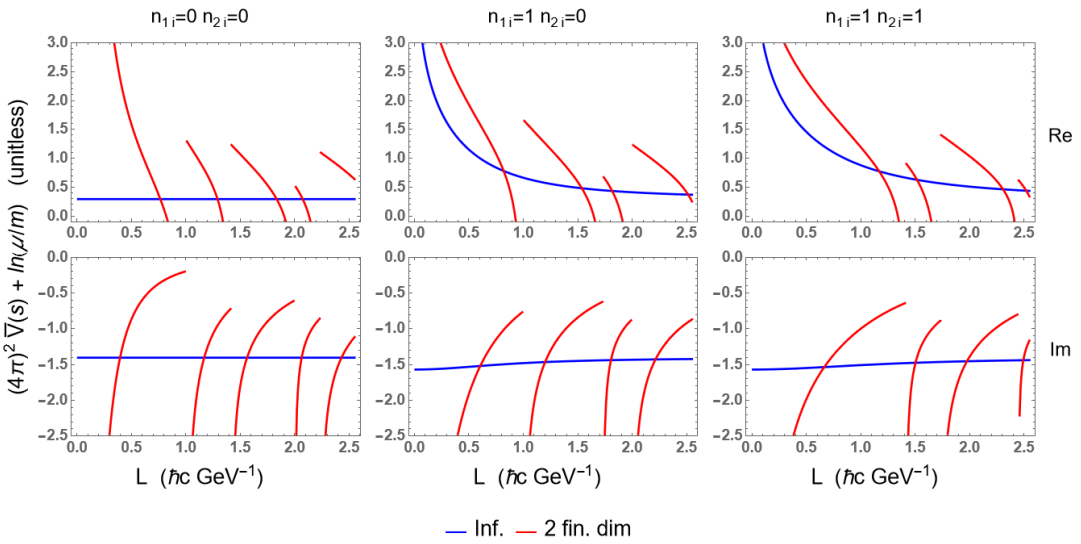

Figure 6.6: A plot of the infinite volume (blue) and finite length (red) real part (top) and imaginary part (bottom) of $\overline{V}_2(s, L, \mu)$ as a function of the length L for 2 compact dimensions. Left has no initial momentum in either of the compact directions, middle has one mode in one finite direction, and right has one mode in both compact directions. $\mu = 1$ GeV, $m = 0.5$ GeV, and $p_{\text{inf}} = 1$ GeV.

The divergences away from $p_{\text{inf}} \to 0$ and $L \to 0$ shown in the figures can again be interpreted as "geometric" bound states, where there is now the possibility for an *out* state with all momentum distributed between the two finite dimensions. Unlike in the case of only one finite dimension, one may see from the imaginary part of $\overline{V}_2$ that the measure of the divergence is large enough that the total cross section is infinite at NLO.

Again the divergences at $p_{\text{inf}} \to 0$ and $L \to 0$ are not due to geometric bound states but to the maximal influence of the small system size. From Eq. (D.36), $g_2 \sim |\Lambda^*|$ and thus like $1/L^2$ for $L \to 0$. It is thus unsurprising that Fig. 6.6 shows divergences in the real and imaginary parts of $\overline{V}_2$ as $L \to 0$.

6.2.2 t Channel

We compare the infinite volume and finite volume results for the t channel $\overline{V}_2(t, L, \mu)$ as a function of p_{inf} in Fig. 6.7 and L in Fig. 6.8 for a variety of modes in the initial and final momenta. We do not display plots for configurations for which no scattering occurs, i.e. for when the initial momenta are equal the final momenta $p_i = p_f$. For a fixed momentum transfer in the finite directions, t approaches a finite, non-zero value

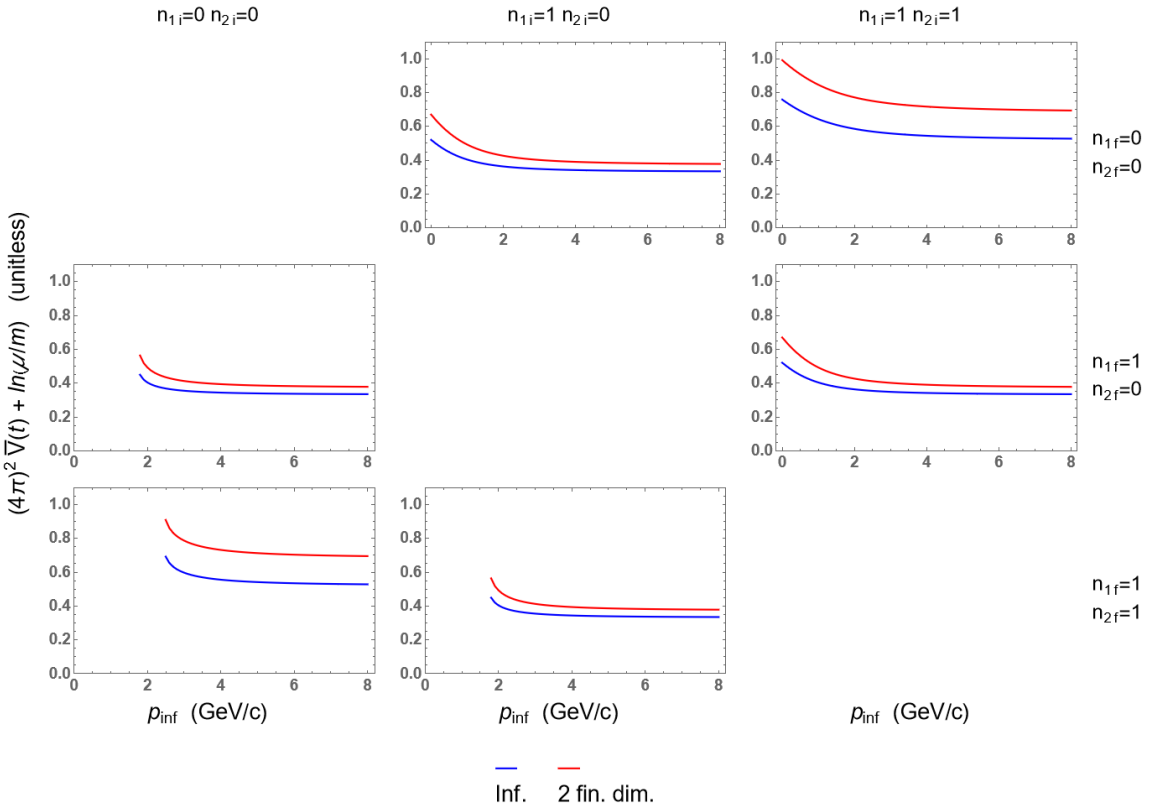

Figure 6.7: A plot of the infinite volume (blue) and finite length (red) $\overline{V}_2(t, p_{\text{inf}}, \mu)$ as a function of p_{inf} for 2 compact dimensions. The plots are shown for various numbers of modes in the initial and final finite directions. Plots are not shown for when the particles do not scatter, i.e. for $p_i = p_f$. $\mu = 1$ GeV, $m = 0.5$ GeV, and $L = 1/\sqrt{3}$ GeV^{-1}.

as $p_{\text{inf}} \to \infty$ limit. We are thus unsurprised to see in Fig. 6.7 that the finite system size correction remains non-zero even in the limit of $p_{\text{inf}} \to \infty$. However the real parts of $\overline{V}_2(s, L, \mu)$ and $\overline{V}_2(u, L, \mu)$ diverge in this limit, meaning the relative influence of the finite system size correction to the amplitude still vanishes as $p_{\text{inf}} \to \infty$. Similar to the 1 compact dimension case, for $n_{1i}^2 + n_{2i}^2 < n_{f1}^2 + n_{f2}^2$ we have that the plots of $\overline{V}_2$ cut off for small p_{inf} or L where an imaginary outgoing momentum in the infinite direction would be necessary to maintain conservation of energy.

We see that in contrast to the scan in momentum, we have convergence of the finite system size result in the $L \to \infty$ limit, as we would expect. As in 1 compact dimension, when $n_{1i}(n_{1i} - n_{1f}) + n_{2i}(n_{2i} - n_{2f}) > 0$, the $L \to 0$ limit implies $t \to -\infty$. Exactly as in the 1 compact dimension case, $t \to -\infty$ will lead to a divergence from the infinite volume contribution and a finite system size correction that goes to 0.

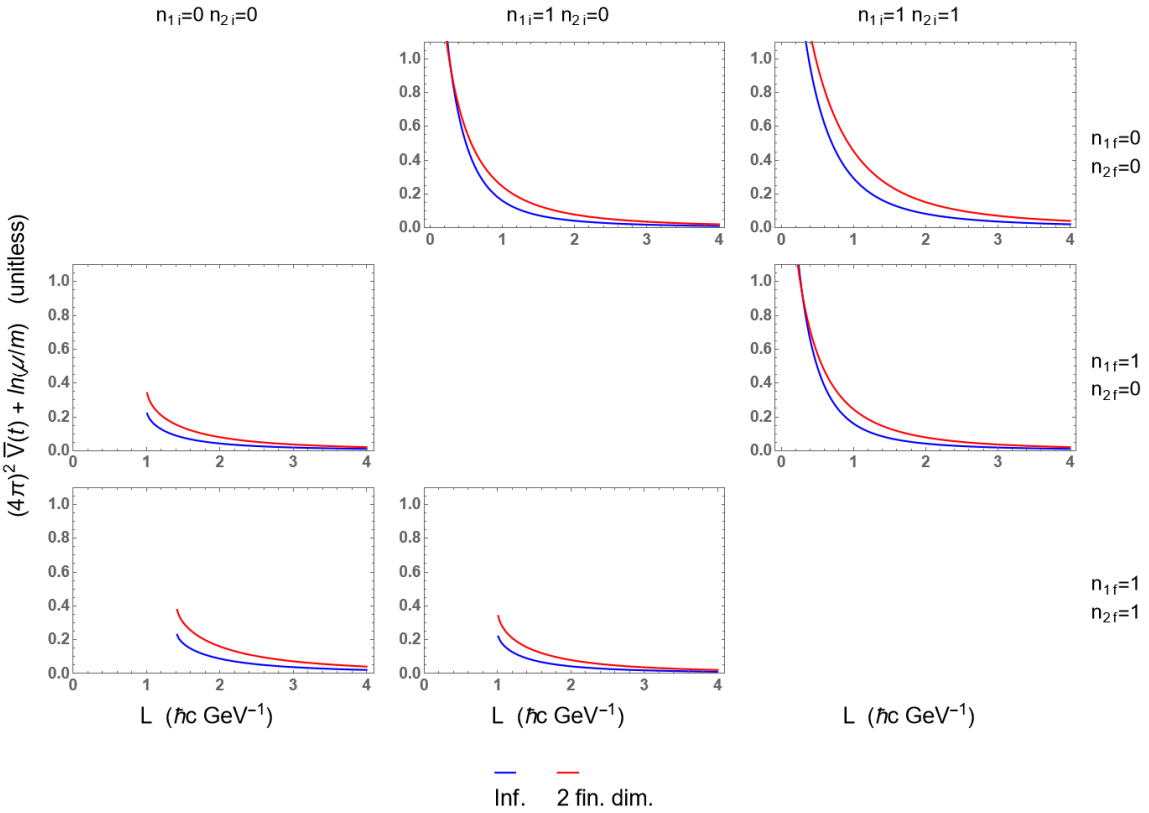

Figure 6.8: A plot of the infinite volume (blue) and finite length (red) $\overline{V}_2(t, L, \mu)$ as a function of L for 2 compact dimensions. The plots are shown for various numbers of modes in the initial and final finite directions. Plots are not shown for when the particles do not scatter, i.e. for $p_i = p_f$. $\mu = 1$ GeV, $m = 0.5$ GeV, and $p_{\text{inf}} = 1$ GeV.

6.3 Three Compact Dimensions

The case of three compact dimensions presents a number of conceptual and numerical challenges. Conceptually, unless the finite lengths are very large, the incoming and outgoing wavepackets are never widely separated. Since the incoming and outgoing states can no longer be asymptotically separated, presumably one would have to modify the usual LSZ treatment in order to connect to a physically realisable setup. Even though the connection to a real physical setup is unclear, one may still—in principle—formally evaluate Eq. (4.14).

However, as is shown in detail in Eq. (C.13), the s channel contribution to $\overline{V}$ is actually trivial. For momentum configurations that are physical, i.e. the momenta have an integer number of modes along any finite direction, one has that $\overline{V}(s_{physical}) = \infty$, since the particles are "geometrically bound"; the particles interact an infinite number of times

inside the fully compact space. Otherwise, for unphysical momenta, $\overline{V}(s_{unphysical}) = 0$.

We would like to perform another non-trivial check of our analytics and numerics through a comparison with an analytic expression for an asymptotic expansion of Eq. (4.14). We perform this check on the t channel contribution to $\overline{V}$ in three compact dimensions in the next section.

Chapter 7

Asymptotic Analysis

We show plots comparing the infinite volume contribution to the finite system size correction to $\overline{V}(t, \{L_i\}; \mu, \epsilon)$ for $\vec{p}^2 > 0$ and $p^0 = 0$ in Fig. 7.1 as a function of the momentum $|\vec{p}|$ and as a function of the finite system size L for $m = 0.5$ GeV and $\mu = 1$ GeV. We note that computing $\overline{V}(t)$ is something of a hypothetical exercise as the three compact dimension case is pathological. Nevertheless, it's interesting to consider the t channel contribution in three compact dimensions as a smooth function of $|\vec{p}|$ or L because the phases in Eq. (4.14) cause non-trivial oscillations as a function of these parameters and because the finite system size corrections are maximal in a fully compactified space. One can see that for $p \sim 1/L$ the finite system size corrections are on the same order as the infinite volume contribution. Note that the oscillations seen in the finite system size corrections as a function of both $|\vec{p}|$ and L are real and due to the oscillating phases multiplying the modified Bessel function, as we shall show.

7.1 Large Argument Analysis

We seek an asymptotic expansion for terms that look like products of cosines and a modified Bessel function of the second kind. Taking for simplicity only one cosine for the moment, generically we seek an expansion in inverse powers of $\lambda_2 \sim \sqrt{\vec{p}^2 L^2}$ of

$$I(\lambda_1, \lambda_2, \alpha) \equiv \int_0^1 dx \cos(2\pi x \lambda_1) K_0\big(2\pi\sqrt{x(1-x)+\alpha^2}\lambda_2\big), \tag{7.1}$$

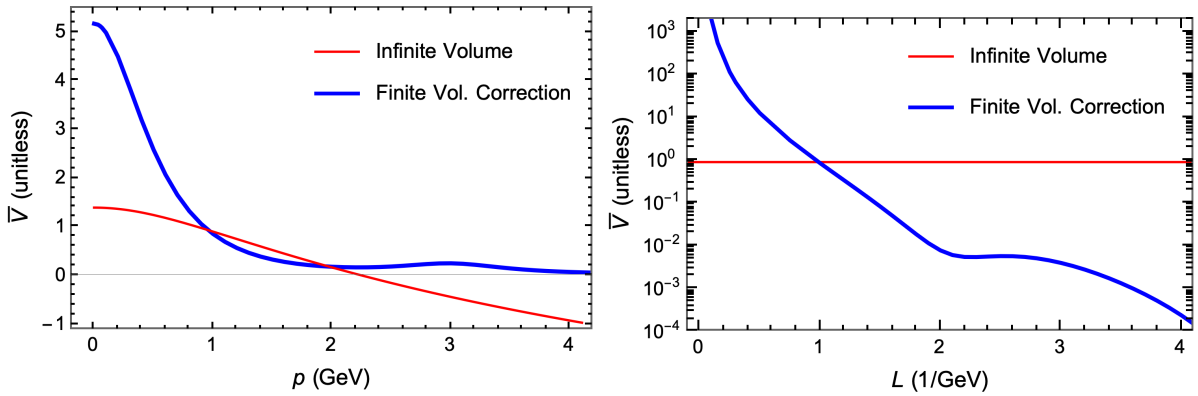

Figure 7.1: *Left*: A comparison of the infinite volume contribution to $\overline{V}(p^2, \{L_i\}; \mu, \epsilon)$ to the finite volume corrections (without the overall prefactor of $-1/32\pi^2$) as a function of $p \equiv |\vec{p}|$ for $L_i = 1/\sqrt{3}$ (GeV^{-1}), $m = 0.5$ GeV, and $\mu = 1$ GeV for the t channel contribution with the assumption of $p^0 = 0$ GeV.
Right: Same comparison but as a function of $L_i = L/\sqrt{3}$ for $|\vec{p}| = 1$ GeV, $p^0 = 0$ GeV, $m = 0.5$ GeV, and $\mu = 1$ GeV. The y-axes of both plots are dimensionless.

where $\alpha^2 \equiv m^2/\vec{p}^2$ and $\lambda_1 \sim p^i L_i$.

The approach we'll take is to employ Laplace's method [70]. To get the integral in the correct form, in which an integrand is multiplied by a decaying exponential, we change integration variables and use the integral representation of the Bessel function. First, take $y' \equiv \sqrt{x(1-x)+\alpha^2}$. The inverse of y' is double-valued, so we must separately consider the original integral from $x = 0$ to $1/2$ and from $x = 1/2$ to 1

$$I_\pm(\alpha, \lambda_1, \lambda_2) \equiv \int_\alpha^{\frac{1}{2}\sqrt{1+4\alpha^2}} dy' \frac{2y'}{\sqrt{1+4\alpha^2-4y'^2}} \cos\left(2\pi\frac{1}{2}(1 \pm \sqrt{1+4\alpha^2-4y'^2})\lambda_1\right) K_0(2\pi\lambda_2 y), \quad (7.2)$$

where

$$I(\lambda_1, \lambda_2, \alpha) = I_-(\lambda_1, \lambda_2, \alpha) + I_+(\lambda_1, \lambda_2, \alpha). \quad (7.3)$$

Note the crucial relative sign difference in the arguments of the cosines. To make the application of Laplace's method easier, we shift the integration variable to $y \equiv y' + \alpha$; at the same time, introduce one of the standard integral representations of the Bessel function [71] to yield

$$I_\pm(\alpha, \lambda_1, \lambda_2) = \int_0^\infty dt\, e^{-2\pi\alpha\lambda_2\cosh(t)} \int_0^{\frac{1}{2}\sqrt{1+4\alpha^2}-\alpha} dy f_\pm(\alpha, \lambda_1; y) e^{-2\pi\alpha\lambda_2\cosh(t)y}, \quad (7.4)$$

$$f_\pm(\alpha, \lambda_1; y) \equiv \frac{2(y+\alpha)}{\sqrt{1-8\alpha y-4y^2}} \cos\left(\pi(1 \pm \sqrt{1-8\alpha y-4y^2})\lambda_1\right).$$

Laplace's method tells us that

$$I_{\pm}(\alpha,\lambda_1,\lambda_2) \sim \int_0^\infty dt\, e^{-2\pi\,\alpha\,\lambda_2\cosh(t)} \int_0^\infty dy \big[f_{\pm}(\alpha,\lambda_1;0) + f'_{\pm}(\alpha,\lambda_1;0) y + \ldots \big] e^{-2\pi\,\alpha\,\lambda_2\cosh(t) y}, \quad (7.5)$$

where $\sim$ indicates that exponentially suppressed terms $\sim \exp(-\lambda_2)$ have been dropped; note especially the change in the upper bound of the y integration limit. One has in general that

$$\int_0^\infty dy\, y^{n-1} e^{-2\pi\lambda_2\cosh(t) y} = \frac{\Gamma(n)}{(2\pi\,\lambda_2)^n} \mathrm{sech}^n(t). \quad (7.6)$$

One may then perform the integral over t, yielding the Bickley function [71]

$$\mathrm{Ki}_n(x) \equiv \int_0^\infty dt\, e^{-x\,\cosh(t)} \mathrm{sech}^n(t), \quad x > 0. \quad (7.7)$$

Clearly $\mathrm{Ki}_0(x) = K_0(x)$. One may find an explicit expression for $\mathrm{Ki}_1(x)$ by integrating under the integral sign to find

$$\begin{aligned} \mathrm{Ki}_1(x) &= \int_x^\infty dx' K_0(x') \\ &= \frac{\pi}{2} - \frac{\pi\, x}{2} \big(K_0(x) L_{-1}(x) + K_1(x) L_0(x) \big). \end{aligned} \quad (7.8)$$

Further explicit representations of the Bickley function in terms of modified Bessel functions of the second kind and the modified Struve functions can be found through the recursion relation [71]

$$\alpha\, \mathrm{Ki}_{\alpha+1}(x) + x\, \mathrm{Ki}_\alpha(x) + (1-\alpha)\, \mathrm{Ki}_{\alpha-1}(x) - x\, \mathrm{Ki}_{\alpha-2}(x) = 0. \quad (7.9)$$

Like the modified Bessel functions of the second kind, the Bickley functions decrease monotonically with x, and further decrease monotonically with order. One finds for large x that

$$\mathrm{Ki}_\alpha(x) \sim K_\alpha(x) \sim \sqrt{\frac{\pi}{2x}} \exp(-x). \quad (7.10)$$

One readily computes that

$$f_-(\alpha,\lambda_1;0) = 2\alpha \quad (7.11)$$

$$f_+(\alpha,\lambda_1;0) = 2\alpha\cos(2\pi\,\lambda_1). \quad (7.12)$$

Thus we see how the phase factors in Eq. (4.14) lead to the non-trivial oscillations in

Fig. 7.1.

For increased numerical accuracy, we may go to the next order. One finds that

$$f'_-(\alpha,\lambda_1;0) = (1+4\alpha^2) \tag{7.13}$$

$$f'_+(\alpha,\lambda_1;0) = (1+4\alpha^2)\cos(2\pi\lambda_1) + 4\pi\alpha^2\lambda_1\sin(2\pi\lambda_1). \tag{7.14}$$

If we drop the higher order in α contributions, which is well-justified in the large p^2 limit, a significant simplification occurs;

$$I(\lambda_1,\lambda_2,\alpha) \sim \frac{\alpha}{\pi\lambda_2}\big(1+\cos(2\pi\lambda_1)\big)K_1(2\pi\alpha\lambda_2). \tag{7.15}$$

If we apply Eq. (7.15) to Eq. (4.14) (see also Eq. (B.20)) we find *after integrating over* x that

$$\overline{V}(p^2,\{L_i\};\mu) \sim \overline{V}_\infty(p^2;\mu) - \frac{1}{2}\frac{1}{(4\pi)^2}\Bigg\{\sum_{s\in 2^{[3]}} 2^{|s|+1}\sum_{\substack{m_i=1\\ i\in s}}^{\infty}\Bigg(1+\prod_{i\in s}\Big(\cos(2\pi\, m_i L_i p^i)\Big)\Bigg) \times \frac{m}{\pi p^2\sqrt{\sum(m_i^2L_i^2)}}K_1\Bigg(2\pi\, m\sqrt{\sum(m_i^2L_i^2)}\Bigg)\Bigg\}, \tag{7.16}$$

where

$$\begin{aligned}\overline{V}_\infty(p^2;\mu) &\equiv -\frac{1}{2}\frac{1}{(4\pi)^2}\int_0^1 dx\,\ln\frac{\mu^2}{\Delta^2}\\ &= -\frac{1}{2}\frac{1}{(4\pi)^2}\left[2+\ln\frac{\mu^2}{m^2} - 2\sqrt{1+\frac{4m^2}{p^2}}\tanh^{-1}\left(\sqrt{\frac{p^2}{p^2+4m^2}}\right)\right]\end{aligned} \tag{7.17}$$

is the infinite volume contribution to NLO $2\to 2$ scattering.

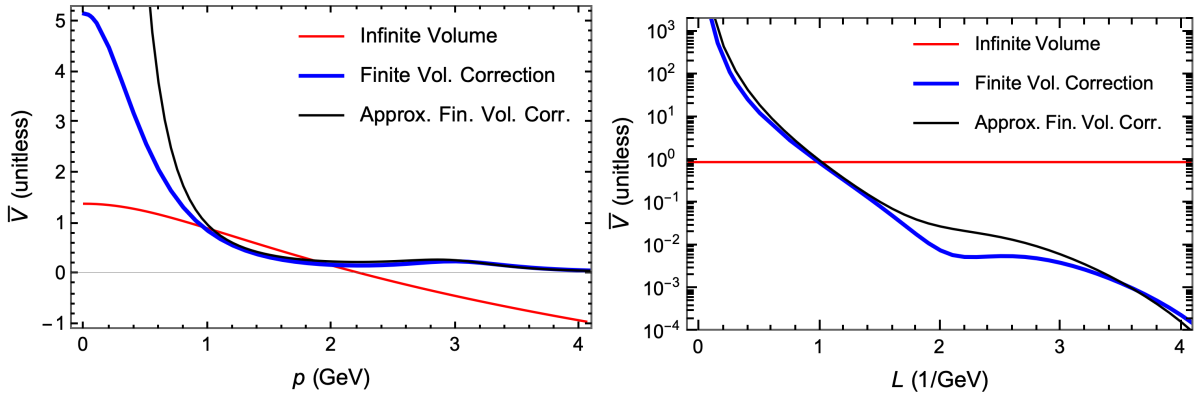

Figure 7.2: *Left*: A comparison of the infinite volume contribution to $\overline{V}(p^2,\{L_i\};\mu,\epsilon)$ to the finite volume corrections (without the overall prefactor of $-1/32\pi^2$) and its asymptotic approximation for large argument as a function of $p\equiv|\vec{p}|$ for $L_i = 1/\sqrt{3}$ (GeV^{-1}), $m = 0.5$ GeV, and $\mu = 1$ GeV for the t channel contribution with the assumption of $p^0 = 0$ GeV. *Right*: Same comparison but as a function of $L_i = L/\sqrt{3}$ for $|\vec{p}| = 1$ GeV, $p^0 = 0$ GeV, $m = 0.5$ GeV, and $\mu = 1$ GeV. The y-axes of both plots are dimensionless.

We compare the asymptotic expansion of Eq. (7.16) to the full result Eq. (4.14) in Fig. 7.2. The comparison is much better for the scan in p as $\alpha \propto 1/\sqrt{p^2}$. Including more terms in the asymptotic expansion improves the convergence.

7.2 Small Argument Analysis

We wish to understand the behaviour of the finite system size correction as $\vec{p} \to \vec{0}$ and/or $L_i \to 0$.

For $p^2 \to 0$ and $m > 0$, we may safely ignore the phases and trivially integrate over x. Then

$$\overline{V}(p^2, \{L_i\}; \mu) \approx \overline{V}_\infty(p^2; \mu) - \frac{1}{2}\frac{1}{(4\pi)^2} 2 {\sum_{\vec{m}\in\mathbb{Z}^3}}' K_0\Big(2\pi\, m\sqrt{\sum m_i^2 L_i^2}\Big). \tag{7.18}$$

One can see in Fig. 7.1 how in the small p^2 limit for $m > 0$ that the finite system size correction converges to a finite value.

If $m = 0$ and we take $p^2 \to 0$, or if $L_i \to 0$ (and $m \geq 0$), then we may still ignore the phases but must consider the integration over x in the finite system size correction. For small argument $K_0(z) = \ln(2/z) - \gamma_E + \mathcal{O}(z)$ [71]. If we perform our change of variables as in Eq. (7.2) we may integrate over x to find

$$\int_0^1 dx\, K_0(2\pi\sqrt{x(1-x)+\alpha^2}\lambda_2) = \frac{1}{2}\big(1 - \gamma_E - \ln(\pi\,\lambda_2)\big) + g(\alpha) + \mathcal{O}(\lambda_2), \tag{7.19}$$

where $g(\alpha) = \mathcal{O}(\alpha^2)$ is a complicated expression that smoothly goes to 0 as $m \to 0$ and may be safely ignored for the range of m and p^2 we consider here. We thus see that in the small L limit or in the small p^2 limit (for $m = 0$) the finite system size correction diverges logarithmically. The divergence is slightly faster than logarithmic in the sense that as the argument of the Bessel function decreases, more and more terms from the sum over m_i contribute; one must sum over $m_i \lesssim 1/\pi\sqrt{p^2 \sum L_i^2}$. One can see in Fig. 7.1 how in the small L_i limit the finite system size correction diverges slightly faster than logarithmically.

We now have a good handle on the behaviour of $\overline{V}$ in finite systems, so we can proceed to considering the behaviour of the effective coupling in Chapter 8.

Chapter 8

Finite Size Effective Coupling

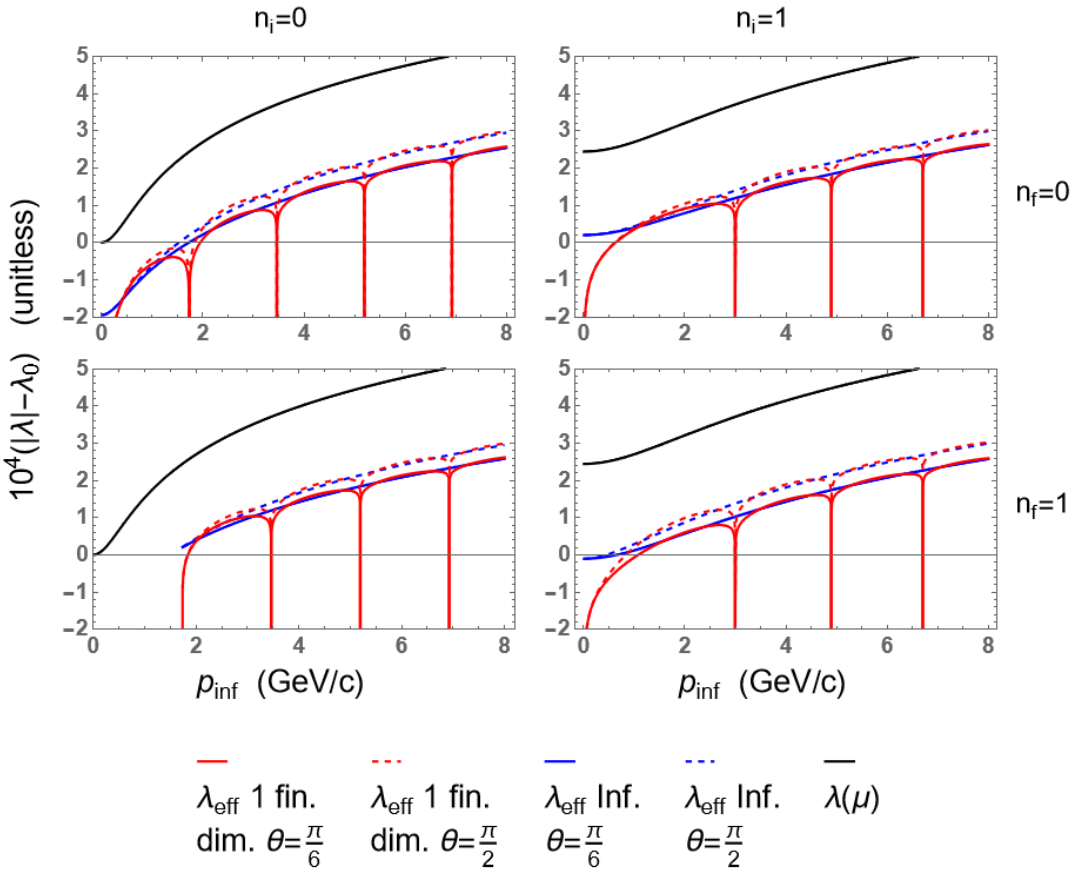

Figure 8.1: A comparison of the running coupling $\lambda(\mu)$ with $\mu^2 = s$ and $\mu_0 = 2m$ (black) and the absolute value of the infinite volume effective coupling $\lambda_{\text{eff}}(s,t)$ (blue) with $m = 0.5$ GeV and scattering angle $\theta = \pi/6, \pi/2$ (solid,dashed) and the absolute value of the finite volume effective coupling $\lambda_{\text{eff}}(s,t,\{L_i\})$ (red) with $L = 1/\sqrt{3}$ GeV^{-1} for $n = 1$ compact dimension as a function of p_{inf} for renormalised coupling with $\lambda_0 = 0.1$ at $\mu = \mu_0$.

Having explored the finite system size correction to $\overline{V}(p^2, \{L_i\}; \mu)$, we wish to under-

stand quantitatively the finite system size effects on the effective coupling. The finite system size effective coupling is the obvious generalisation of Eq. (2.22), replacing the infinite volume $\overline{V}(p^2;\mu)$ with the finite volume $\overline{V}(p^2,\{L_i\};\mu)$:

$$-i\lambda_{\text{eff}}(s,t,\{L_i\}) = \frac{-i\lambda(\mu)}{1-\lambda(\mu)\big(\overline{V}(s,\{L_i\})+\overline{V}(t,\{L_i\})+\overline{V}(u,\{L_i\})\big)}. \tag{8.1}$$

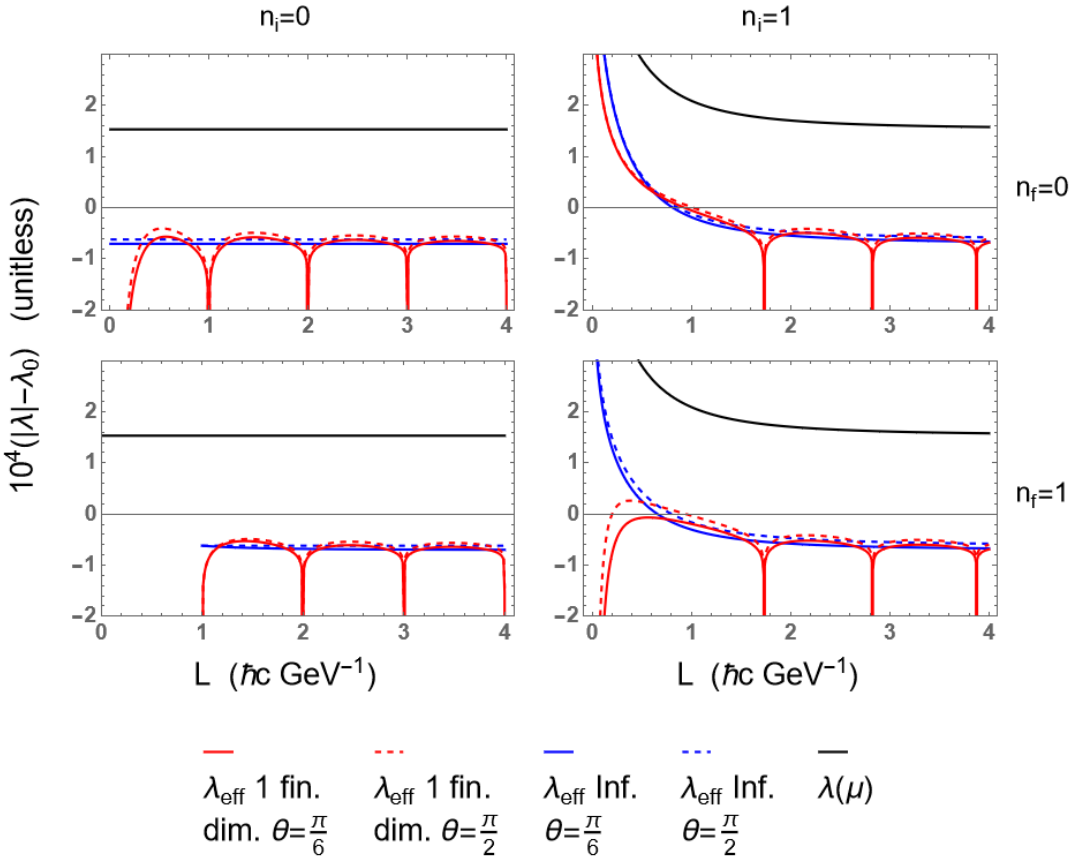

Figure 8.2: Same comparison but as a function of L (GeV^{-1}) for $p_{\text{inf}} = 1$ GeV. For both plots, the y-axes are dimensionless and the dips actually take the coupling all the way to 0 (note that the y-axis has been shifted and rescaled, to compare the corrections to the effect of the running of the coupling).

Since $\overline{V}$ picks up an imaginary part for the s channel for $|\vec{p}| > 0$, both in the infinite volume and for the finite volume correction (as required by unitarity), the effective coupling becomes complex. A complex effective coupling is a bit unusual but not a fundamental problem [72]: physical quantities always involve taking the modulus squared of the (potentially complex) amplitude.

We show the absolute value of the running coupling $\lambda(\mu)$, the infinite volume effective coupling λ_{eff}, and the finite volume effective coupling λ_{eff} minus the initial value of the

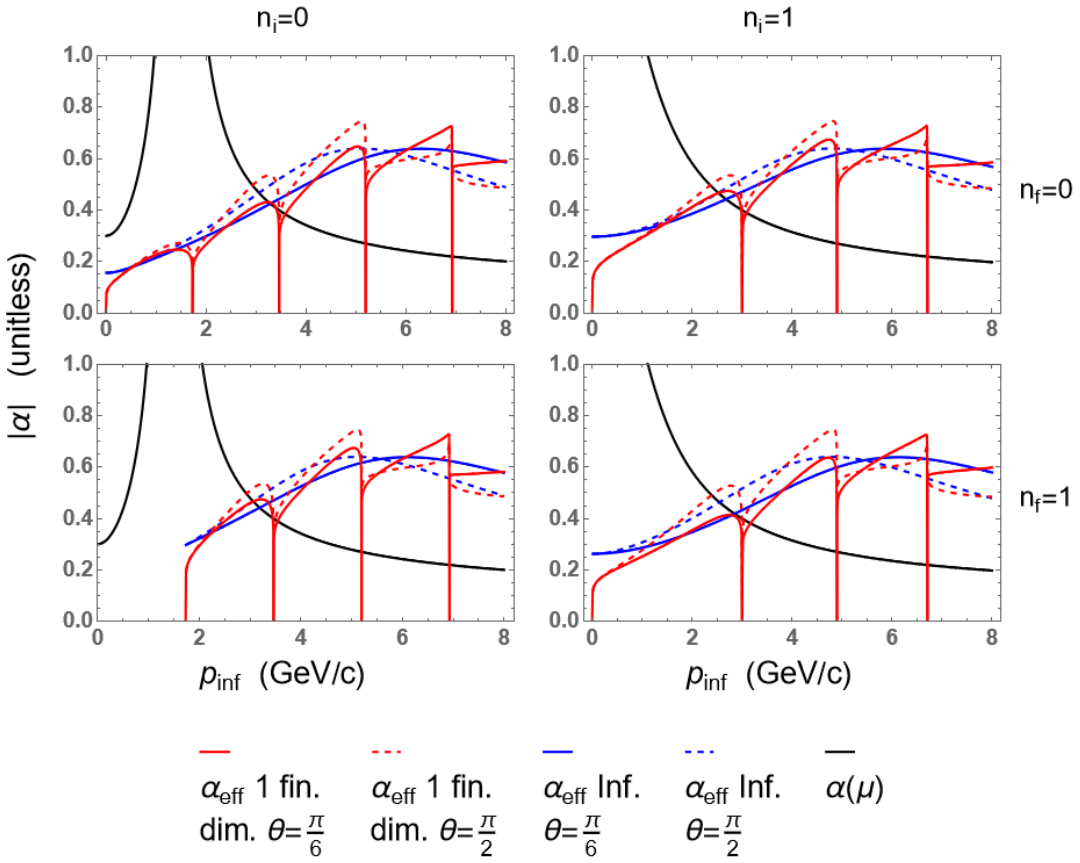

Figure 8.3: A comparison of the running coupling $\alpha(\mu)$ with $\mu^2 = s$ and $\mu_0 = 2m$ (black) and the absolute value of the infinite volume effective coupling $\alpha_{\text{eff}}(s,t)$ (blue) with $m = 0.5$ GeV and scattering angle $\theta = \pi/6, \pi/2$ (solid, dashed) and the absolute value of the finite volume effective coupling $\alpha_{\text{eff}}(s,t,\{L_i\})$ (red) with $L = 1/\sqrt{3}$ GeV^{-1} for $n = 1$ compact dimension as a function of p_{inf} for renormalised coupling with $\alpha_0 = 0.3$ at $\mu = \mu_0$.

coupling λ_0 and scaled by a factor of 10^4 as functions of p_{inf} in Fig. 8.1 and of the size of the finite dimension, L, in Fig. 8.2 for $n = 1$ compact dimensions. We choose to subtract the initial value and scale the results in order to make the differences among the results more clearly visible. We use the same notation as in Chapter 6; in particular, our momenta are given by Eq. (6.6). We take the finite system size direction to have a length $1/\sqrt{3}$ GeV^{-1}. For the running coupling, we use $\mu^2 = s$ and $\mu_0 = 2m$, where $m = 0.5$ GeV, and the value of the renormalised coupling at the initial scale is $\lambda_0 = 0.1$. We consider scattering at angles $\theta = \pi/2, \pi/6$ among the infinite directions. One sees that the running coupling captures the leading logarithmic behaviour of the effective coupling. One can further see that the finite system size effective coupling converges to the infinite system size effective coupling as either p_{inf} and/or L become large (compared to the other). We

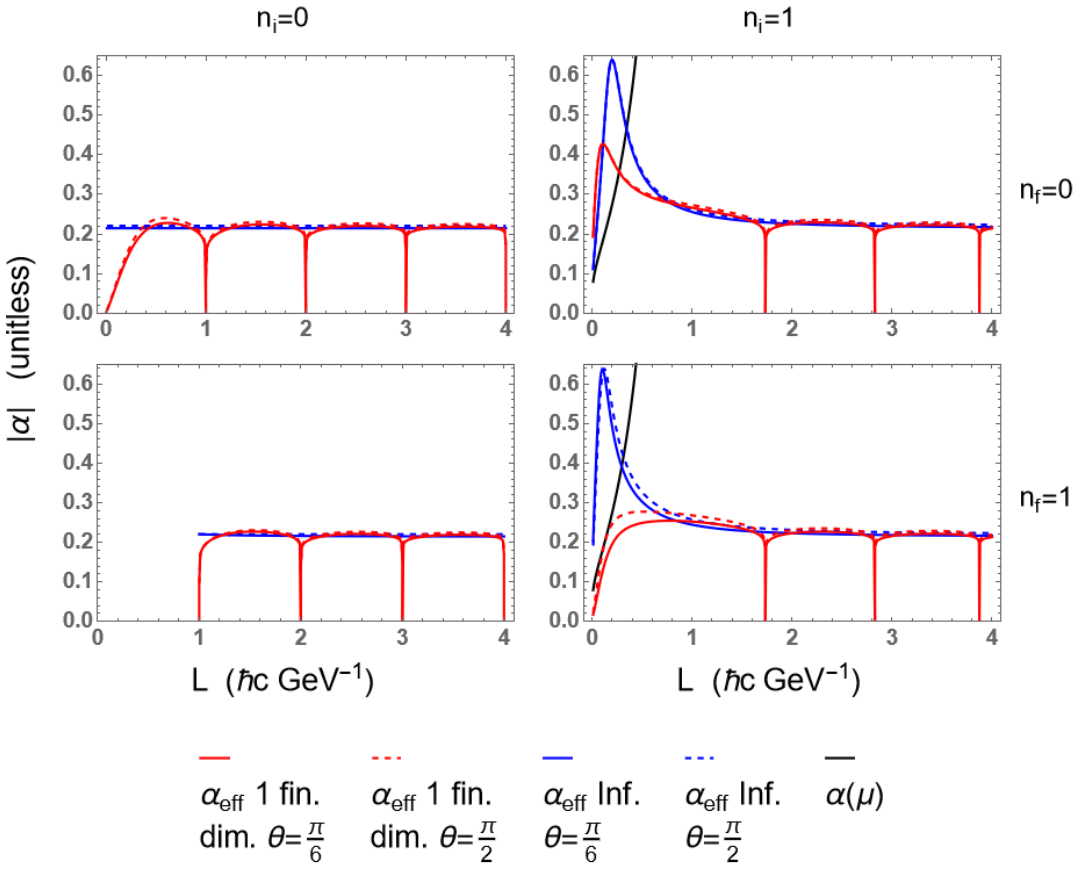

Figure 8.4: Same comparison but as a function of L (GeV^{-1}) for $p_{\text{inf}} = 1$ GeV. For both plots, the y-axes are dimensionless and the dips again take the coupling exactly to 0.

can see that other than the geometric bound states (where the effective coupling goes to 0) there are minimal corrections with one finite dimension. One may consider it odd that in the case of the geometric bound states the coupling goes to zero given that the cross section diverges. We understand this discrepancy as due to the resummation of the bubble diagrams not capturing the bound state physics; at the geometric bound states, one should rather resum a set of ladder diagrams. Note that the existence and location of these divergences in $\overline{V}(p^2, \{L_i\}; \mu)$, which lead to the finite system size effective coupling going to 0, are *independent* of the strength of the coupling.

Similar to α_{EM} (in QED) or α_s (in QCD), we may further define the relevant expansion parameter for ϕ^4 theory, $\alpha \equiv \lambda/(4\pi)^2$ [73]. We show the comparison between the running coupling $\alpha(\mu)$, the infinite volume effective coupling $\alpha_{\text{eff}}(s,t)$, and the finite volume effective coupling $\alpha_{\text{eff}}(s,t,\{L_i\})$ in Fig. 8.3 and Fig. 8.4. The much larger initial $\alpha = 0.3$ leads to a much larger change in the coupling as a function of the various scales.

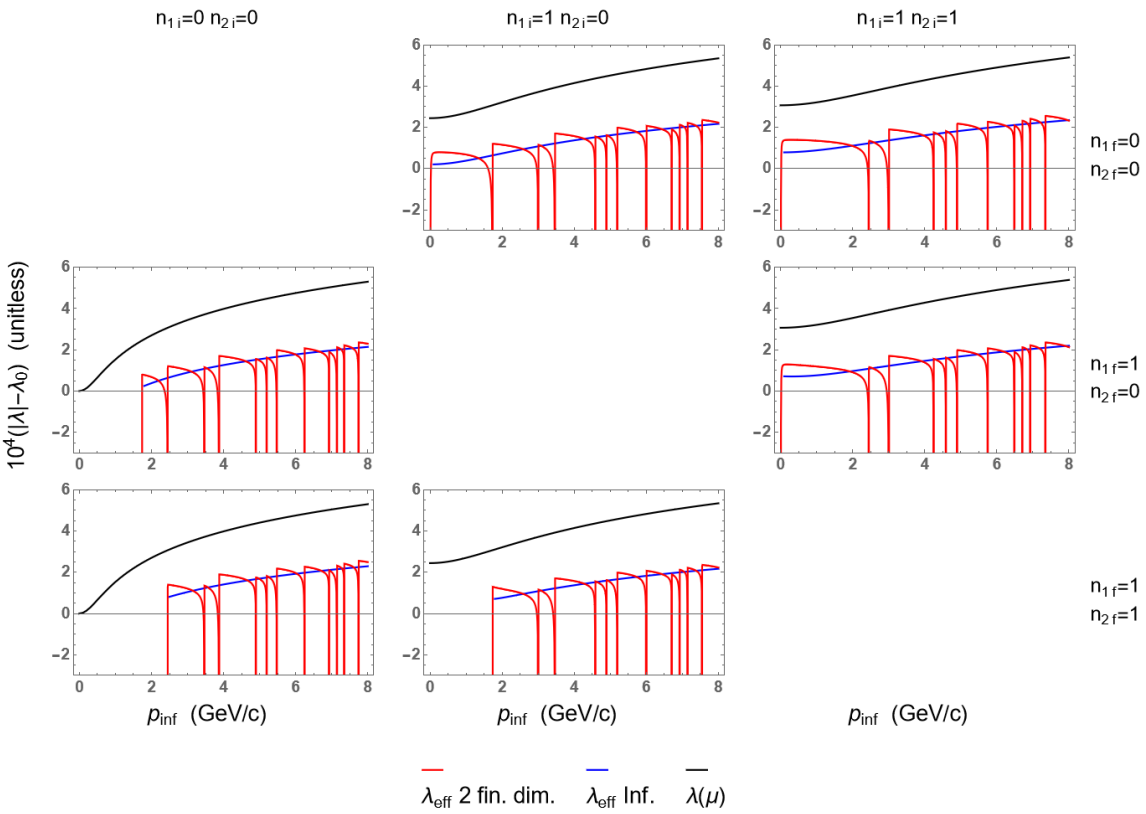

Figure 8.5: A comparison of the running coupling $\lambda(\mu)$ with $\mu^2 = s$ and $\mu_0 = 2m$ (black) and the absolute value of the infinite volume effective coupling $\lambda_{\text{eff}}(s,t)$ (blue) with $m = 0.5$ GeV and the absolute value of the finite volume effective coupling $\lambda_{\text{eff}}(s,t,\{L_i\})$ (red) with $L_1 = L_2 = L = 1/\sqrt{3}$ GeV^{-1} for $n = 2$ compact dimensions as a function of p_{inf} for renormalised coupling $\lambda_0 = 0.1$ at $\mu = \mu_0$. The y-axes are dimensionless and the coupling is exactly 0 at the dips.

In particular, one can see that the rapid approach of the Landau pole at modest $p \sim 2$ GeV means that the running coupling no longer captures the leading logarithmic dependence of the effective coupling. Interestingly, the effective coupling completely avoids the Landau pole. One can see that the finite system size effective coupling still tracks the infinite volume effective coupling; for large enough p or L the results converge.

One can see that, e.g. in Fig. 8.3 and Fig. 8.4, the effective coupling decreases as $p_{\text{inf}} \times L$ becomes small. The coupling decreasing in this limit is not due to a geometric bound state. Rather, the coupling going to zero here is a reflection of the magnitude of the NLO contribution to the amplitude increasing due to the small system size compared to the momentum, $p_{\text{inf}} \times L \ll 1$. This decrease of the coupling with $p_{\text{inf}} \times L$ is consistent with a calculation of the effective coupling in a lattice discretisation of ϕ^4 theory in finite volume [74]. Since $1/L \to \infty$ corresponds to a large momentum scale and the beta

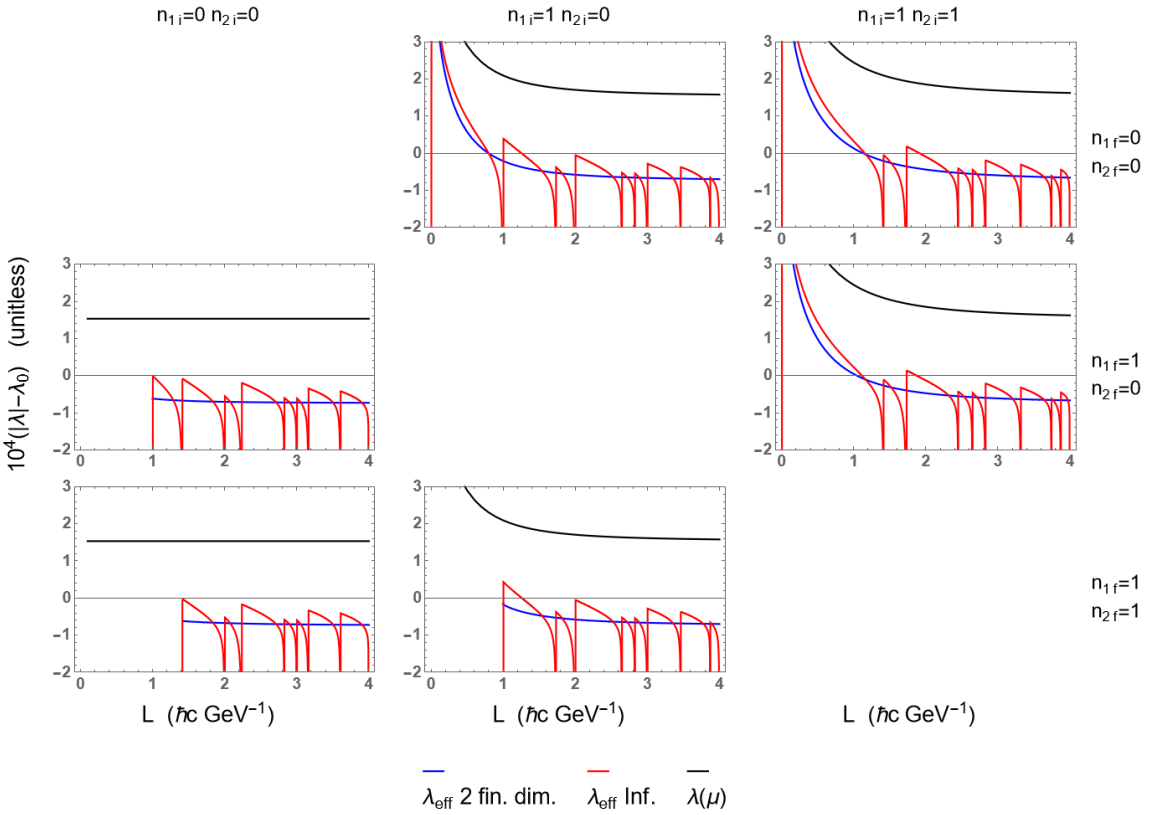

Figure 8.6: Same comparison as in Fig. 8.5 but as a function of L (GeV^{-1}) for $p_{\text{inf}} = 1$ GeV. The y-axes are dimensionless and the coupling is exactly 0 at the dips.

function for ϕ^4 theory is positive, it's very interesting that the coupling decreases as $p_{\text{inf}} \times L$ decreases.

Recall from Sec. 6.1.1 that for $p_{\text{inf}} \times L \to 0$ the amplitude $\overline{V}_1(s, L, \mu)$ in fact diverges. Certainly for $\lambda(\mu)\overline{V}_1(s, L, \mu) \lesssim 1$ we may trust the geometric sum into the effective coupling. For $\lambda(\mu)\overline{V}_1(s, L, \mu) \gtrsim 1$, one may consider the effective coupling as the analytic continuation of the resummation of the geometric series, which agrees with, e.g., the Borel sum of the geometric series. Taking the analytic continuation seriously, the effective coupling goes to zero in the limit $p_{\text{inf}} \times L \to 0$. It's not clear that one may still physically interpret this effective coupling; it is not immediately obvious that it is sensible for the effective coupling to be zero when the cross section is infinite.

For $n = 2$ compact dimensions, we show in Figs. 8.5 and 8.6 the absolute value of the running coupling $\lambda(\mu)$, the infinite volume effective coupling $\lambda_{\text{eff}}(s, t)$, and the finite volume effective coupling $\lambda_{\text{eff}}(s, t, \{L_i\})$ minus the initial value of the coupling λ_0 and scaled by a factor of 10^4 as functions of p_{inf} and of the size of the finite dimension, L.

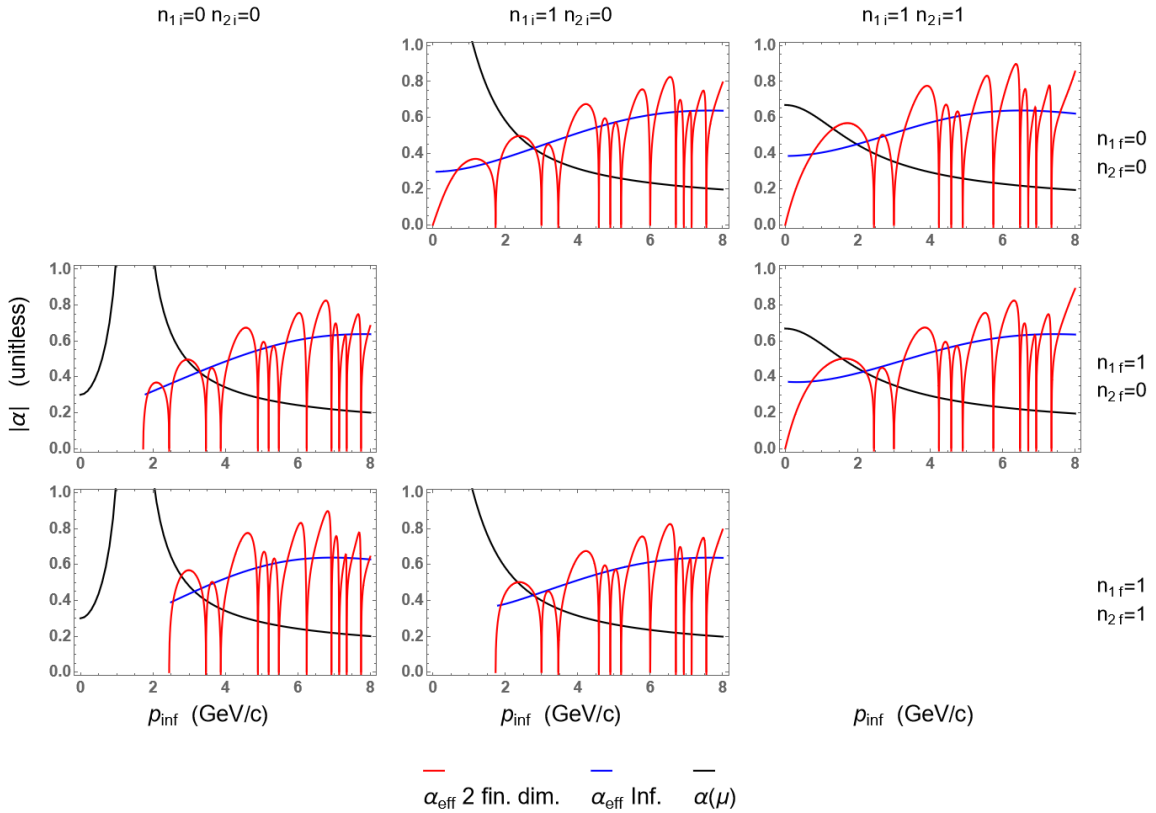

Figure 8.7: A comparison of the running coupling $\alpha(\mu)$ with $\mu^2 = s$ and $\mu_0 = 2m$ (black) and the absolute value of the infinite volume effective coupling $\alpha_{\text{eff}}(s,t)$ (blue) with $m = 0.5$ GeV $=$ and the absolute value of the finite volume effective coupling $\lambda_{\text{eff}}(s,t,\{L_i\})$ (red) with $L_1 = L_2 = L = 1/\sqrt{3}$ GeV^{-1} for $n = 2$ compact dimensions as a function of p_{inf} for renormalised coupling $\alpha_0 = 0.3$ at $\mu = \mu_0$. The y-axes are dimensionless and the coupling is exactly 0 at the dips.

We again choose $\mu^2 = s$ and $\mu_0 = 2m$ for the running coupling with $\lambda_0 = 0.1$. The finite sizes of the system are both $L_1 = L_2 = 1/\sqrt{3}$ GeV^{-1}. The running coupling is given by the black curves, the infinite volume effective coupling by the blue curves and the finite volume effective coupling by the red curves.

In Figs. 8.7 and 8.8 we show the running coupling $\alpha(\mu)$, the infinite volume effective coupling $\alpha_{\text{eff}}(s,t)$, and the finite volume effective coupling $\alpha_{\text{eff}}(s,t,\{L_i\})$ as functions of p_{inf} and of the size of the finite dimensions, $L_1 = L_2 \equiv L$, for $n = 2$ compact dimensions. We again choose $\mu^2 = s$ and $\mu_0 = 2m$ for the running coupling with $\alpha_0 = 0.3$. The running coupling is given by the black curves, the infinite volume effective coupling by the blue curves and the finite volume effective coupling by the red curves.

One can see that the size of the finite system size corrections increases noticeably

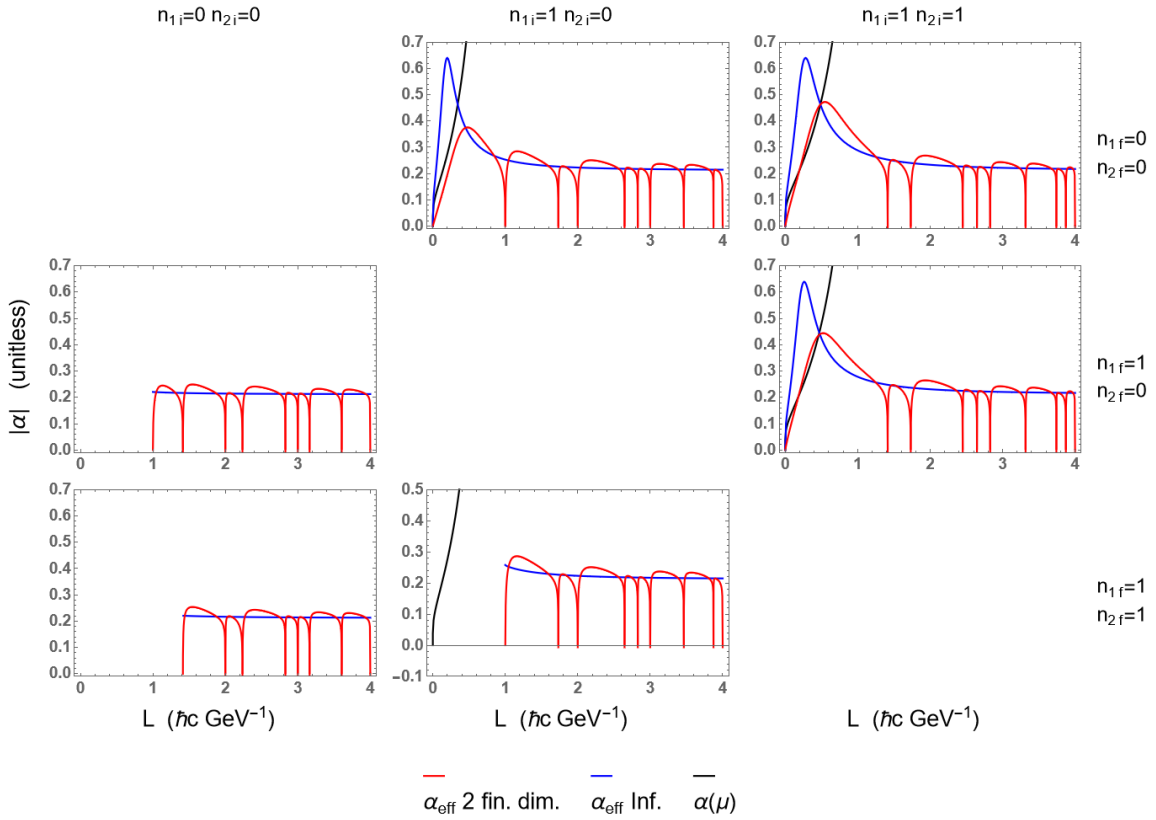

Figure 8.8: Same comparison as in Fig. 8.7 but as a function of L (GeV^{-1}) for $p_{\text{inf}} = 1$ GeV. The y-axes are dimensionless and the coupling is exactly 0 at the dips.

compared to the $n = 1$ case. Nevertheless, the finite system size effective coupling asymptotically approaches the infinite volume effective coupling for large p and/or large L. The dips are again to zero coupling, where the approach is smooth from both sides; the coupling is only non-differentiable at the points of exactly zero coupling. The drop to zero coupling is again due to the divergences of the real and imaginary parts of $\overline{V}$ in the s-channel.

Conclusions

In this thesis, we investigated the finite system sized effects on the NLO $2 \to 2$ scattering amplitude in massive scalar ϕ^4 theory. Special attention was given to the investigation of the effective coupling given by the ressumation of bubble diagrams, as the finite system size corrections to the QCD coupling would have implications to the QCD EOS used in relativistic hydrodynamic modelling of heavy-ion collisions.

We started by giving a non-technical introduction intended to be accessible to a non-expert audience. We then carefully recounted the usual infinite volume derivation of the NLO $2 \to 2$ scattering amplitude in massive ϕ^4 theory using dimensional regularisation, including the derivation of the running coupling from the Callan-Symanzik equation and the effective coupling from a resummation of bubble diagrams. The agreement of the running and effective couplings to a leading logarithm was also shown. We then showed how we can employ denominator regularisation as used in [8] to obtained the same renormalised quantities (by using a natural modification of the unobservable counterterms) in the infinite volume case.

We then considered a spacetime with n finite spatial dimensions (with possibly asymmetric length scales L_i), m infinite spatial dimensions and an infinite temporal dimension. The (renormalised) NLO $2 \to 2$ scattering amplitude in $n = 3$ finite dimension (and $m = 0$ infinite dimensions) was then computed using denominator regularisation and an analytic continuation of the generalised Epstein zeta function. We derived this analytic continuation of the generalised Epstein zeta function by formulating the generalised Epstein zeta function as a general lattice sum, and then employing the Poisson summation formula for lattice sums [67]. We then noted that by taking a relevant length

scale $L_i \to \infty$, we can self-consistently obtain results for the amplitude for $n < 3$ finite dimensions, including reproducing the known result for the $n = 0$ amplitude.

For each $n \leq 3$ we then confirmed that our derived amplitude satisfies unitarity. We did this by confirming that the optical theorem is satisfied by using a direct generalisation of a number theoretic formula originally conjectured by Ramanujan that involves the (2 dimensional) sum of squares function r_2. The derived generalization essentially extend the aforementioned number theoretic formula to using the n dimensional sum of squares function r_n for $0 \leq n \leq 3$. It further also holds for non-square-lattice sums, which can't be represented as sums using the usual sum of squares functions, as long as the lattice still has dimension $0 \leq n \leq 3$. Showing that the formula holds in the Abel summation sense for all $\operatorname{Re} n > 0$ further allows interpretation as an analytic continuation in lattice dimension to all lattices of "dimension" $\operatorname{Re} n > 0$. It is not presently clear that there is any physical interpretation or application of lattices with dimensions with non-zero imaginary part.

Having passed 2 non-trivial self-consistency checks, we numerically evaluate the s- and t-channels in 1 and 2 finite dimensions, in order to analyse their qualitative and quantitative behaviour. We find non-trivial behaviour and corrections. In particular our s-channel shows the existence of "geometric" bound states, by having a resonance with out states where all outgoing momentum is in the finite directions. The numerics of the s-channel in 2 finite dimensions (and one infinite), presented non-trivial convergence issues in the form of a sign problem. Exploiting the analytic structure of the amplitude was necessary to obtain an equivalent form that has much more well-behaved convergence properties.

We performed some asymptotic analysis of the renormalised $\overline{V}(p^2)$ functions representing NLO amputated bubble diagrams. We derive the asymptotic behaviour of the t channel (and equivalently the u channel) finite system size correction in 3 finite dimensions for asymptotically large pL. This result is shown to agree well with numerics. For small arguments we show that $\overline{V}(p^2)$ must have a faster than logarithmic divergence, which is also seen in the numerical evaluation of $\overline{V}(t)$ in 3 finite dimensions.

Finally we numerically investigate the behaviour of the effective and running couplings in 1 and 2 finite dimensions. We find that with 1 finite dimension the effective coupling, outside of geometric bound states, receives little correction for moderate to large scales ($pL \gtrsim 1$), but has non-trivial behaviour at small scales. In particular, at small scales we find that the effective coupling goes to 0. In 2 finite dimensions behaviour becomes even more non-trivial, but we observe corrections up to order 40% away from bound states (our effective coupling is identically 0 at bound states, so will always present 100% corrections there). The effective coupling approaching 0 at effective bound states initially seems contradictory with the observation that the total cross section is infinite at such geometric bound states. We note, however, that we only include the resummation of the bubble diagrams in the effective coupling shown here; our effective coupling does not include the resummation of ladder diagrams necessary to fully capture the relevant physics of the geometric bound states. Nevertheless, the fact that the effective coupling decreases *around* the geometric bound states can be trusted in our work as the coupling times the NLO contribution remains small, $\lambda\overline{V} \ll 1$, until the momenta are extraordinarily close to the resonance, $(p - p_{\text{resonance}})/p_{\text{resonance}} \sim 10^{-10}$. Indeed outside of this extraordinarily close region, one finds that the (non-resummed) NLO amplitude also decreases in magnitude (only diverging extraordinarily close to the geometric bound state).

We discuss interpretations of the effective coupling approaching 0 at geometric bound states, as well as how the small pL behaviour differs from that of geometric bound states. With all three spatial dimensions finite, we find the effective coupling 0 for all physical configurations, since the magnitude of the NLO contribution to the amplitude is infinite.

Our numerical and analytic explorations seem to confirm that the effect of maximum length scales in the system can not simply be thought of as the introduction of a new dimensionful scale for the effect it has on the effective interaction strength of the system. One would ideally have a first-principles Callan-Symanzik-like equation to at least approximately or asymptotically describe the effect of a finite maximum length scale on the interaction strength of a quantum field theory, but it is at present not clear that this is even possible in principle, let alone how to derive it. This is due to the Callan-Symanzik

equations exploiting the fictitious nature of the renormalisation scale, while the length scales introduced in a finite systems are not fictitious. We should therefore think of the *beta* function only as describing how the coupling runs with renormalisation scale *at constant system size*, and need new tools to describe the length-scale induced "running" of the coupling.

Since the effective coupling is found to decrease at small L for ϕ^4 theory, despite a positive β function, it shows the possibility that the effective QCD coupling could in principle increase in small $p+p$ collisions, despite the negative nature of the QCD β function. This can in principle then cause large and unexpected modifications to the QCD EOS in $p+p$ and $p+A$ collisions. Such modifications could cast doubt on the interpretation of p+p and p+A collisions forming a nearly inviscid fluid. This doubt would come from the necessary modifications to the hydrodynamic simulations (that currently use the infinite system QCD EOS [5, 58]) used to extract the shear and bulk viscosities from v_2 measurements. The discovery of non-trivial finite system size corrections to the equation of state could raise questions about the success of relativistic hydrodynamics in modelling p+p and p+A collisions. Understanding these corrections may provide insight into the justification for using the hydrodynamic approach in modelling $A+A$ collisions.

In conclusion, the insights gained from our analysis of finite system size effects provide new perspectives on the potential non-trivial behaviour of effective couplings in finite systems. The possibility that the effective QCD coupling could increase in small collisions, despite the negative nature of the QCD β function, is an intriguing possibility that invites further exploration. Future work will be required to delve into the explicit calculations needed to validate these findings. Verifying that the finite system size corrections to the trace anomaly in ϕ^4 theory corresponds with the finite system size corrections to the effective coupling derived in this thesis is a natural next step. One would also like an analytic exploration of the small argument asymptotics of the effective coupling, which would require solving non-trivial order of limit challenges to find the asymptotic behaviour of the finite system size corrections to the s channel. Computing finite system size corrections in a gauge theory would further present the problem of accounting for torons

[75, 76] (non-trivial gauge configurations on the torus) which is non-trivial and remains to be addressed. Many of the techniques developed and used in this thesis are expected to be useful in any such future calculations in finite systems.

Appendix A

Denominator Regularisation

In dimensional regularisation, one analytically continues the integration measure in order to regularise divergent integrals. In a discrete phase space, one utilises sums instead of integrals. Abstractly, one does Lebesgue integration using a counting measure over some lattice, instead of the Lebesgue measure over continuous phase space. Analytic continuation of the counting measure or the lattice on which it is defined presents practical and philosophical difficulties, especially when the discrete phase space has some asymmetry. This suggests that it may be appropriate to rather follow another strategy when dealing with discretised (asymmetric) phase spaces. One can of course instead try and analytically continue the integrand in a systematic fashion to imitate the effect of of an analytically continued integration measure.

Formally, we care about the logarithmically divergent integral

$$I = \int \frac{d^n l}{(2\pi)^n} \frac{1}{(l^2 + z)^{\frac{n}{2}}}, \tag{A.1}$$

with z some complex number with non-zero imaginary part. Dimensional regularisation prescribes the analytic continuation

$$I(\epsilon) = \int \frac{d^{n-2\epsilon} l}{(2\pi)^n} \frac{\mu^{2\epsilon}}{(l^2 + z)^{\frac{n}{2}}}, \tag{A.2}$$

where we will analyse the asymptotic behaviour of $I(\epsilon)$ as $\epsilon \to 0$. Note that we needed to introduce a renormalisation scale μ in order to ensure that our integral stays dimensionally consistent.

If we were to proceed in the usual manner, we would abuse the radial symmetry of

the integral as follows:

$$I(\epsilon) = \int \frac{d^{n-2\epsilon}l}{(2\pi)^{n-2\epsilon}} \frac{\mu^{2\epsilon}}{(l^2+z)^{\frac{n}{2}}} \tag{A.3}$$

$$= \int_0^\infty dr \int \frac{d\Omega_{n-2\epsilon-1} r^{n-2\epsilon-1}}{(2\pi)^{n-2\epsilon}} \frac{\mu^{2\epsilon}}{(r^2+z)^{\frac{n}{2}}} \tag{A.4}$$

$$= \frac{\Omega_{n-2\epsilon-1}}{(2\pi)^{n-2\epsilon}} \int_0^\infty dr \, \frac{r^{n-2\epsilon-1}\mu^{2\epsilon}}{(r^2+z)^{\frac{n}{2}}}. \tag{A.5}$$

Here $\Omega_{d-1} = \frac{2\pi^{\frac{d}{2}}}{\Gamma\left(\frac{d}{2}\right)}$ is the "surface area" of a unit $(d-1)$-sphere, the boundary of a d dimensional unit ball.

$$I(\epsilon) = \frac{2\pi^{\frac{n}{2}-\epsilon}}{\Gamma\left(\frac{n}{2}-\epsilon\right)(2\pi)^{n-2\epsilon}} \frac{\mu^{2\epsilon} z^{-\epsilon} \Gamma\left(\frac{n}{2}-\epsilon\right)\Gamma(\epsilon)}{2\Gamma\left(\frac{n}{2}\right)} \tag{A.6}$$

$$= \frac{\mu^{2\epsilon} z^{-\epsilon}\Gamma(\epsilon)}{(4\pi)^{\frac{n}{2}-\epsilon}\Gamma\left(\frac{n}{2}\right)} \tag{A.7}$$

$$= \frac{1}{(4\pi)^{\frac{n}{2}}\Gamma\left(\frac{n}{2}\right)} \left(\frac{1}{\epsilon} + \ln(4\pi) - \gamma + \ln\left(\frac{\mu^2}{z}\right)\right) + \mathcal{O}(\epsilon), \tag{A.8}$$

where everything independent of z will end up being renormalised away. Let us however realise that we can redo this calculation slightly differently. We can instead separate the integrals over integer and fractional dimensions as follows:

$$I(\epsilon) = \int \frac{d^{n-2\epsilon}l}{(2\pi)^{n-2\epsilon}} \frac{\mu^{2\epsilon}}{(l^2+z)^{\frac{n}{2}}} \tag{A.9}$$

$$= \int \frac{d^n l}{(2\pi)^n} \int \frac{d^{-2\epsilon}\ell}{(2\pi)^{-2\epsilon}} \frac{\mu^{2\epsilon}}{(\ell^2+l^2+z)^{\frac{n}{2}}} \tag{A.10}$$

$$= \int \frac{d^n l}{(2\pi)^n} \frac{\Omega_{-2\epsilon-1}}{(2\pi)^{-2\epsilon}} \int_0^\infty dr \, \frac{r^{-2\epsilon-1}\mu^{2\epsilon}}{(r^2+l^2+z)^{\frac{n}{2}}}. \tag{A.11}$$

Here the inner integral diverges in the IR, but since we are already analytically continuing in ϵ, we can get the following reasonable result:

$$I(\epsilon) = \int \frac{d^n l}{(2\pi)^n} \frac{2\pi^{-\epsilon}}{\Gamma(-\epsilon)(2\pi)^{-2\epsilon}} \frac{\Gamma(-\epsilon)\Gamma\left(\frac{n}{2}+\epsilon\right)}{2\Gamma\left(\frac{n}{2}\right)} \frac{\mu^{2\epsilon}}{(l^2+z)^{\frac{n}{2}+\epsilon}} \tag{A.12}$$

$$= \frac{\pi^{-\epsilon}\Gamma\left(\frac{n}{2}+\epsilon\right)}{(2\pi)^{-2\epsilon}\Gamma\left(\frac{n}{2}\right)} \int \frac{d^n l}{(2\pi)^n} \frac{\mu^{2\epsilon}}{(l^2+z)^{\frac{n}{2}+\epsilon}}. \tag{A.13}$$

Here we can see that analytically continuing the integral measure of this logarithmic integral is equivalent to analytically continuing the exponent in the denominator as well as the overall factor of the integral. We can calculate and expand both of these as series in powers of ϵ:

$$I(\epsilon) = \frac{\pi^{-\epsilon}\Gamma\left(\frac{n}{2}+\epsilon\right)}{(2\pi)^{-2\epsilon}\Gamma\left(\frac{n}{2}\right)} \int_0^\infty dr\, \frac{\Omega_{n-1} r^{n-1}}{(2\pi)^n} \frac{\mu^{2\epsilon}}{(r^2+z)^{\frac{n}{2}+\epsilon}} \tag{A.14}$$

$$= \frac{1}{(4\pi)^{\frac{n}{2}}} \left[\frac{\pi^{-\epsilon}\Gamma\left(\frac{n}{2}+\epsilon\right)}{(2\pi)^{-2\epsilon}\Gamma\left(\frac{n}{2}\right)}\right] \left[\frac{\mu^{2\epsilon} z^{-\epsilon}\Gamma(\epsilon)}{\Gamma\left(\frac{n}{2}+\epsilon\right)}\right] \tag{A.15}$$

$$= \frac{1}{(4\pi)^{\frac{n}{2}}\Gamma\left(\frac{n}{2}\right)} \left[1+\mathcal{O}(\epsilon)\right] \left[\frac{1}{\epsilon} - \gamma - \Gamma'\left(\frac{n}{2}\right) + \ln\left(\frac{\mu^2}{z}\right) + \mathcal{O}(\epsilon)\right], \tag{A.16}$$

so since everything independent of z ends up renormalised away, and everything $\mathcal{O}(\epsilon)$ can be neglected, we can claim that we only need to analytically continue the power of the denominator in the integrand, since the differences the analytic continuation of the prefactor introduce have no physical effect, it only changes the specifics of our subtraction scheme necessary to renormalise. We will call said analytic continuation denominator regularisation.

A similar analysis can be seen in [8, 11].

Appendix B

Generalised Epstein Zeta Function

We would like to analytically continue the generalised Epstein-zeta function

$$\zeta(\{a_i\},\{b_i\},c;s) \equiv \sum_{\vec{n}\in\mathbb{Z}^p} \left[a_i^2 n_i^2 + b_i n_i + c\right]^{-s}, \tag{B.1}$$

again using the Poisson summation formula [67]

$$\sum_{\vec{k}\in\Lambda} f(\vec{k}) = \frac{1}{|\Lambda|} \sum_{\ell\in\Lambda^*} F(\vec{\ell}), \tag{B.2}$$

where Λ^* is the dual lattice, the lattice with the same dimension with spacings inverted of that of the original (so $|\Lambda| = |\Lambda^*|^{-1}$), and F is the Fourier transform of f, given by

$$F(\vec{\ell}) \equiv \int d^n k\, e^{-2\pi i \vec{k}\cdot\vec{\ell}} f(\vec{k}). \tag{B.3}$$

We can write

$$\zeta(\Lambda,\vec{\delta},c;s) = \sum_{\vec{k}\in\Lambda} \left[(\vec{k}+\vec{\delta})^2 + c\right]^{-s}, \tag{B.4}$$

which logarithmically diverges at $\dim(\Lambda) = 2s$. If we write

$$f(\vec{k}) \equiv \left[(\vec{k}+\vec{\delta})^2 + c\right]^{-s} \tag{B.5}$$

$$g(\vec{k}) \equiv f(\vec{k}-\vec{\delta}) \tag{B.6}$$

$$= \left[k^2 + c\right]^{-s}. \tag{B.7}$$

By the shift formula for Fourier transforms we then have

$$F(\vec{\ell}) = e^{-2\pi i \vec{\ell}\cdot\vec{\delta}} G(\vec{\ell}), \tag{B.8}$$

but since g is a radial function, we can use

$$G(\ell) = 2\pi\ell^{\frac{2-n}{2}} \int_0^\infty dr g(r) J_{\frac{n-2}{2}}(2\pi\ell r) r^{\frac{n}{2}}, \tag{B.9}$$

where n is the dimension of Λ. For $\ell > 0, 0 < n < 1 + 4s, \operatorname{Im} c \neq 0$ we then get

$$G(\ell) = \frac{2\pi^s}{\Gamma(s)} c^{\frac{n-2s}{4}} \ell^{s-\frac{n}{2}} K_{\frac{n-2s}{2}}(2\pi\ell\sqrt{c}). \tag{B.10}$$

For $\ell = 0$, we can take the $\ell \to 0$ limit at Eq. (B.9), and then evaluate

$$G(0) = \frac{2\pi^{\frac{n}{2}}}{\Gamma\left(\frac{n}{2}\right)} \int_0^\infty dr\, r^{n-1}(c + r^2)^{-s} \tag{B.11}$$

$$= \frac{2\pi^{\frac{n}{2}}}{\Gamma(s)} \Gamma\left(s - \frac{n}{2}\right) c^{\frac{n-2s}{2}} \tag{B.12}$$

for $n < 2s, \operatorname{Im} c \neq 0$. So for $n < 2s$ and with $\operatorname{Im} c \neq 0$ we have that

$$\zeta(\Lambda, \vec{\delta}, c; s) = \sum_{\vec{k}\in\Lambda} \left[(\vec{k} + \vec{\delta})^2 + c\right]^{-s} \tag{B.13}$$

$$= \sum_{\vec{k}\in\Lambda} f(\vec{k}) \tag{B.14}$$

$$= \frac{1}{|\Lambda|} \sum_{\vec{\ell}\in\Lambda^*} F(\vec{\ell}) \tag{B.15}$$

$$= \frac{1}{|\Lambda|} \sum_{\vec{\ell}\in\Lambda^*} e^{-2\pi i\vec{\ell}\cdot\vec{\delta}} G(\ell) \tag{B.16}$$

$$= \frac{1}{|\Lambda|} \frac{2\pi^{\frac{n}{2}}}{\Gamma(s)} \Gamma\left(s - \frac{n}{2}\right) c^{\frac{n-2s}{2}} + \frac{1}{|\Lambda|} {\sum_{\vec{\ell}\in\Lambda^*}}' e^{-2\pi i\vec{\ell}\cdot\vec{\delta}} \frac{2\pi^s}{\Gamma(s)} c^{\frac{n-2s}{4}} \ell^{s-\frac{n}{2}} K_{\frac{n-2s}{2}}(2\pi\ell\sqrt{c}) \tag{B.17}$$

$$\zeta(\Lambda, \vec{\delta}, c; s) = \frac{2\pi^{\frac{n}{2}}}{\Gamma(s)} c^{\frac{n}{2}-s} |\Lambda^*| \times \left[\Gamma\left(s - \frac{n}{2}\right) + {\sum_{\vec{\ell}\in\Lambda^*}}' \cos(2\pi\vec{\ell}\cdot\vec{\delta}) \left(\frac{\|\vec{\ell}\|}{c}\right)^{s-\frac{n}{2}} K_{\frac{n}{2}-s}(2\pi\|\vec{\ell}\|\sqrt{c})\right]. \tag{B.18}$$

In order to be able to numerically evaluate Eq. (B.18), it is convenient to rephrase it

closer to the usual form of the generalised Epstein zeta function:

$$\sum_{\vec{n}\in\mathbb{Z}^p}(a_i^2n_i^2+b_in_i+c-i\varepsilon)^{-s}=\frac{1}{a_1\cdots a_p}\frac{1}{\Gamma(s)}\Bigg[\pi^{p/2}\Gamma\big(s-\frac{p}{2}\big)\Big(c-\sum\frac{b_i^2}{4a_i^2}-i\varepsilon\Big)^{\frac{p}{2}-s}$$
$$+2\pi^s\sum_{\vec{m}\in\mathbb{Z}^p}{}'\,e^{-2\pi\,i\sum\frac{m_ib_i}{2a_i^2}}\left(\frac{c-\sum\frac{b_i^2}{4a_i^2}-i\varepsilon}{\sum\frac{m_i^2}{a_i^2}}\right)^{\frac{p}{4}-\frac{s}{2}}K_{s-\frac{p}{2}}\left(2\pi\sqrt{(c-\sum\frac{b_i^2}{4a_i^2}-i\varepsilon)(\sum\frac{m_i^2}{a_i^2})}\right)\Bigg]. \tag{B.19}$$

We may numerically evaluate the $\sum_{\vec{m}\in\mathbb{Z}^p}{}'$ in Eq. (B.19) more efficiently by combining the phases into cosines. The speed-up comes from evaluating a pure real expression and from drastically reducing the total number of summed terms. The result is a sum over all the subsets of the set of numbers $\{1,\ldots,p\}$, known as the power set, $2^{[p]}$:

$$\sum_{\vec{m}\in\mathbb{Z}^p}{}'\,e^{-2\pi\,i\sum\frac{m_ib_i}{2a_i^2}}\left(\frac{c-\sum\frac{b_i^2}{4a_i^2}-i\varepsilon}{\sum\frac{m_i^2}{a_i^2}}\right)^{\frac{p}{4}-\frac{s}{2}}K_{s-\frac{p}{2}}\left(2\pi\sqrt{(c-\sum\frac{b_i^2}{4a_i^2}-i\varepsilon)(\sum\frac{m_i^2}{a_i^2})}\right)$$
$$=\sum_{s\in2^{[p]}}2^{|s|+1}\sum_{\substack{m_i=1\\ i\in s}}^{\infty}\prod_{i\in s}\Big(\cos(2\pi\,x\,m_iL_ip^i)\Big)$$
$$\times\left(\frac{c-\sum\frac{b_i^2}{4a_i^2}-i\varepsilon}{\sum\frac{m_i^2}{a_i^2}}\right)^{\frac{p}{4}-\frac{s}{2}}K_{s-\frac{p}{2}}\left(2\pi\sqrt{(c-\sum\frac{b_i^2}{4a_i^2}-i\varepsilon)(\sum\frac{m_i^2}{a_i^2})}\right), \tag{B.20}$$

where $|s|$ is the length of the current set of indices being summed over and the sums with the suppressed limits are over $i\in s$. This is a specific case of the more general observation that for some function f on a lattice Λ, such that $f(-\vec{k})=f(\vec{k})$ we have

$$\sum_{\vec{k}\in\Lambda}f(\vec{k})=\sum_{\Gamma\in2^\Lambda}2^{\dim(\Gamma)+1}\sum_{\vec{k}\in\Gamma^+}f(\vec{k}). \tag{B.21}$$

Here we used 2^Λ, the "powerset" of the lattice, which is the set of all sub-lattices, as well as Γ^+, which is the set of all vectors in Γ that have all relevant components positive. A sub-lattice can be seen as a subset of the original lattice, with some set of indices set identically to 0. We also note that

$$\sum_{\vec{k}\in\Lambda}f(\vec{k})\cos(2\pi\vec{k}\cdot\vec{\delta})=\sum_{\vec{k}\in\Lambda}f(\vec{k})\prod_i\cos(2\pi k_i\delta_i) \tag{B.22}$$

can be proved by recursively applying the sum of angles formula for cos and exploiting the even nature of $f,\cos$ and the odd nature of sin.

For a related analysis see [8, 9, 13].

Appendix C

Generalised Sum of Sinc Functions

For this unitarity analysis we will need to derive a generalisation of the formula

$$\sum_{0\leq n<x} \frac{r_2(n)}{\sqrt{x-n}} = 2\pi\sqrt{x} + \sum_{n=1}^{\infty} \frac{r_2(n)}{\sqrt{n}} \sin(2\pi\sqrt{nx}), \qquad x>0, x\notin\mathbb{Z} \tag{C.1}$$

originally proposed by Ramanujan and expanded on by Hardy in Eq. (2) on page 82 of [68].

We will generalise Eq. (C.1) by considering the rectangular lattice sum

$$\sum_{\vec{k}\in\Lambda} \mathrm{sinc}(2\pi\|\vec{k}\|),$$

where Λ is a lattice of dimension $\dim(\Lambda)=n$ and determinant $|\Lambda|$, the volume obtained as the product of the lattice spacings.

We will be employing the Poisson summation formula for rectangular lattice sums [67], given by

$$\sum_{\vec{k}\in\Lambda} f(\vec{k}) = \frac{1}{|\Lambda|} \sum_{\ell\in\Lambda^*} F(\vec{\ell}), \tag{C.2}$$

where Λ^* is the dual lattice, the lattice with the same dimension with spacings inverted of that of the original (so $|\Lambda| = |\Lambda^*|^{-1}$), and F is the Fourier transform of f, given by

$$F(\vec{\ell}) \equiv \int d^n k\, e^{-2\pi i \vec{k}\cdot\vec{\ell}} f(\vec{k}). \tag{C.3}$$

As in [77] we can exploit the radial nature of the function to use the formula

$$F(\ell) = 2\pi \ell^{\frac{2-n}{2}} \int_0^{\infty} dr f(r) J_{\frac{n-2}{2}}(2\pi\ell r) r^{\frac{n}{2}}.$$

We therefore need to evaluate

$$F(\ell) = 2\pi\ell^{\frac{2-n}{2}} \int_0^\infty dr\, \mathrm{sinc}(2\pi r) J_{\frac{n-2}{2}}(2\pi\ell r) r^{\frac{n}{2}} \tag{C.4}$$

$$= \frac{\pi^{\frac{1-n}{2}}}{2\Gamma\left(\frac{3-n}{2}\right)} \sqrt{1-\ell^2}^{1-n} \theta(1-\ell^2), \tag{C.5}$$

which is valid for $0 < n < 3$ and $\ell \geq 0$. Inserting Eq. (C.5) into Eq. (C.2) we find the generalisation of Eq. (C.1),

$$\sum_{\vec{k}\in\Lambda} \mathrm{sinc}(2\pi\|\vec{k}\|) = \frac{\pi^{\frac{1-n}{2}}\,|\Lambda^*|}{2\Gamma\left(\frac{3-n}{2}\right)} \sum_{\substack{\vec{\ell}\in\Lambda^* \\ \ell^2\leq 1}}^{*} \sqrt{1-\ell^2}^{1-n}, \tag{C.6}$$

where $\sum^*$ denotes that terms with $\ell^2 = 1$ have a weight of $\theta(0)$, whose value depends on convention. Equivalent results were obtained in [8, 9, 12]. If one considers the $n = 1$ dimensional lattice with unit spacing case, one can show that the only self-consistent choice is $\theta(0) = \frac{1}{2}$, which agrees with the convention used in Eq. (C.1) and is corroborated by explicitly computing Eq. (C.4) with $n = 1, \ell = 1$ and equating it with Eq. (C.5). Eq. (C.6) with $\theta(0) = \frac{1}{2}$ is then our generalisation of Hardy and Ramanujan's Eq. (C.1). One can carefully check that Eq. (C.6) is also valid for $n = 0$ (trivially gives $1 = 1$), but one should be careful with Eq. (C.4), since the dominated convergence theorem fails at $n = 0, \ell = 0$, so we cannot interchange a limit to $n = 0, \ell = 0$ with the integral (indeed, doing this gives an incorrect answer). We also consider the $n = 3$ case below. Eq. (C.6) of course also holds for more general lattices (than just the rectangular lattices we are interested in), where the determinant is then not, in general, simply given by the product of lattice spacings.

We can now also consider some special cases on square lattices with spacings given by some positive R. These come up in our numerical explorations, which considers the case where all finite dimensions have equal length scale.

Considering a 1D lattice with spacing R, Eq. (C.6) gives

$$\sum_{k=-\infty}^{\infty} \mathrm{sinc}(2\pi R k) = \frac{R^{-1}}{2} \sum_{-R\leq\ell\leq R}^{*} 1$$

$$= \begin{cases} \frac{\lfloor R \rfloor}{R} + \frac{1}{2R} & r_1(R^2) = 0 \\ 1 & R \in \mathbb{Z}. \end{cases} \tag{C.7}$$

Considering a 2D lattice with both spacings R; Eq. (C.6) gives

$$\sum_{\vec{k}\in\mathbb{Z}^2} \mathrm{sinc}(2\pi R\|\vec{k}\|) = \frac{R^{-2}}{2\pi} \sum_{\substack{\vec{\ell}\in\mathbb{Z}^2 \\ \ell^2\leq R^2}}^{*} \frac{1}{\sqrt{1-\frac{\ell^2}{R^2}}}. \tag{C.8}$$

2D radial sums can be simplified into a 1D sum using the sum of squares function r_2, giving

$$\sum_{k=0}^{\infty} r_2(k)\,\mathrm{sinc}\left(2\pi R\sqrt{k}\right) = \frac{1}{2\pi R} \sum_{0\leq l\leq R^2}^{*} \frac{r_2(l)}{\sqrt{R^2-l}}. \tag{C.9}$$

In order to connect with Eq. (C.1) we consider $R^2 \notin \mathbb{Z}$ and we write out $\mathrm{sinc}(x) = \sin(x)/x$

$$2\pi R + \sum_{k=1}^{\infty} \frac{r_2(k)}{\sqrt{k}} \sin\left(2\pi R\sqrt{k}\right) = \sum_{0\leq l<R^2} \frac{r_2(l)}{\sqrt{R^2-l}}. \tag{C.10}$$

Note that we have dropped the star from the $\sum^{*}_{0\leq l<R^2}$ and dropped the equality in the range of the sum, since we have $R^2 \notin \mathbb{Z}$. We can then see that we get Eq. (C.1) by setting $x = R^2$ in Eq. (C.10). This shows that Eq. (C.6) is a direct generalisation to Eq. (C.1).

To consider Eq. (C.6) with $n = 3$ (on a potentially asymmetric lattice), we need to think of Eq. (C.6) as an analytic continuation. The left hand side of Eq. (C.6) evaluated numerically with Cesaro summation seems to yield 0 for $R \notin \mathbb{Z}$ and diverge to positive infinity for $R \in \mathbb{Z}$. To consider the right hand side, we need to return to the Fourier transform integral in Eq. (C.5), which does not converge for $n = 3$. Let us then consider, for some small $\epsilon > 0$

$$F(\ell)\Big|_{n=3} \equiv 2\pi\ell^{-\frac{1}{2}} \int_0^{\infty} dr\,\mathrm{sinc}(2\pi r) J_{\frac{1}{2}}(2\pi\ell r) r^{\frac{3}{2}} e^{-\epsilon r} \tag{C.11}$$

$$= \frac{8\pi\epsilon}{16\pi^4(1-\ell^2)^2 + 8\pi^2(1+\ell^2)\epsilon^2 + \epsilon^4}$$

$$= \begin{cases} \frac{1}{2\pi\epsilon} + \mathcal{O}(\epsilon) & \ell^2 = 1 \\ \frac{\epsilon}{2\pi^3(1-\ell^2)^2} + \mathcal{O}(\epsilon^2) & \ell^2 \neq 1. \end{cases} \tag{C.12}$$

In the $\epsilon \to 0$ limit, we see this continuation agrees with numerics that for a 3 dimensional lattice Λ

$$\sum_{\vec{k}\in\Lambda} \mathrm{sinc}(2\pi\|\vec{k}\|) = \begin{cases} \infty & \vec{\ell} \in \Lambda^* \text{ with } \ell^2 = 1 \\ 0 & \text{otherwise.} \end{cases} \tag{C.13}$$

One might then wonder if the divergences on the two sides of Eq. (C.6) that happens for

an $n = 3$ dimensional lattice Λ with some $\vec{\ell} \in \Lambda^*$ with $\ell^2 = 1$ are equal. To think about two infinities being equal, we need to have some limit of a ratio of diverging quantities limit to 1. There are two ways we can consider these infinities to be equal. The first is to take the expression in Eq. (C.11) seriously, by considering

$$\lim_{\epsilon\to 0^+} \frac{\sum_{\vec{k}\in\Lambda} \operatorname{sinc}(2\pi\|\vec{k}\|)e^{-\epsilon\|\vec{k}\|}}{\sum_{\vec{\ell}\in\Lambda^*} \frac{8\pi\epsilon}{16\pi^4(1-\ell^2)^2 + 8\pi^2(1+\ell^2)\epsilon^2 + \epsilon^4}} = 1 \tag{C.14}$$

by the Poisson summation formula. Similarly we know (if we consider Eq. (C.6) to be an analytic continuation for non-integer $0 < n < 3$ dimensional lattice sums, neglecting to even attempt having a concrete notion of a non-integer dimensional lattice) that

$$\lim_{n\to 3^-} \frac{\sum_{\vec{k}\in\Lambda} \operatorname{sinc}(2\pi\|\vec{k}\|)}{\frac{\pi^{\frac{1-n}{2}}|\Lambda^*|}{2\Gamma\left(\frac{3-n}{2}\right)} \sum^*_{\substack{\vec{\ell}\in\Lambda^* \\ \ell^2\le 1}} \sqrt{1-\ell^2}^{1-n}} = 1 \tag{C.15}$$

by Eq. (C.6).

We may then push the interpretation of Eq. (C.6) as an analytic continuation in n even further. We note that

$$\lim_{\epsilon\to 0^+} \sum_{\vec{k}\in\Lambda} \operatorname{sinc}(2\pi\|\vec{k}\|)e^{-\epsilon\|\vec{k}\|}$$

is the Abel summation of the left hand side of Eq. (C.6). Retracing our previous derivation we then find that in order to employ the Poisson summation formula Eq. (C.2) we need to compute

$$\begin{aligned} F(\ell) &= 2\pi\ell^{\frac{2-n}{2}} \int_0^\infty dr \operatorname{sinc}(2\pi r)e^{-\epsilon r} J_{\frac{n-2}{2}}(2\pi\ell r) r^{\frac{n}{2}} \\ &= 2\pi\ell^{\frac{2-n}{2}} \int_0^\infty dr \operatorname{sinc}(2\pi r)e^{-\epsilon r} \left[\sum_{m=0}^\infty \frac{(-1)^m}{2^{2m+\frac{n-2}{2}}\Gamma\left(\frac{n}{2}\right)\Gamma\left(m+\frac{n}{2}\right)} (2\pi\ell r)^{2m+\frac{n-2}{2}}\right] r^{\frac{n}{2}} \end{aligned} \tag{C.16}$$

$$\begin{aligned} &= 2\pi\ell^{\frac{2-n}{2}} \sum_{m=0}^\infty \frac{(-1)^m}{2^{2m+\frac{n-2}{2}}\Gamma\left(\frac{n}{2}\right)\Gamma\left(m+\frac{n}{2}\right)} \sin\left((2m+n-1)\arctan\left(\frac{2\pi}{\epsilon}\right)\right) \\ &\qquad \times \ell^{2m+\frac{n-2}{2}} (2\pi)^{\frac{4m+n}{2}} (4\pi^2+\epsilon^2)^{\frac{1-2m-n}{2}} \Gamma(2m+n-1) \end{aligned} \tag{C.17}$$

for $1 > \ell \geq 0$ and $\operatorname{Re} n > 0$. It seems plausible that another method, other than employing

the power series of the Bessel function, would extend the range of validity even further. We then find by seemingly safely taking the limit and simplifying to find

$$\begin{aligned}\lim_{\epsilon\to 0^+} F(\ell) &= \frac{1}{2\pi^{\frac{n-1}{2}}}\sum_{m=0}^{\infty}\frac{(-\ell^2)^m}{m!}\Gamma\left(m+\frac{n-1}{2}\right)\sin\left(\pi\left(m+\frac{n-1}{2}\right)\right)\\ &= \frac{\pi^{\frac{1-n}{2}}}{2\Gamma\left(\frac{3-n}{2}\right)}\sqrt{1-\ell^2}^{1-n},\end{aligned} \tag{C.18}$$

where we performed the sum by assuming $0 \leq \ell < 1$. For $\ell = 1$ we have a bit more difficulty, but find that

$$F(1) = \begin{cases} 0 & \operatorname{Re} n < 1 \\ \frac{1}{4} & \operatorname{Re} n = 1 \\ \infty & \operatorname{Re} n > 1, \end{cases} \tag{C.19}$$

where the ∞ will, for general n with $\operatorname{Re} n > 1$, have some prefactor in the sense of characterising the divergences on both sides of Eq. (C.6) to be equal. For $\ell > 1$, the dominated convergence theorem fails to hold at Eq. (C.16), so one cannot simply interchange the integral and sum, and indeed we find inconsistent results if we do. For $0 < n \leq 3$ we know Eq. (C.16) evaluates to 0 for $\ell > 1$, and it seems reasonable that this is generally true for $\operatorname{Re} n > 0$, which would make Eq. (C.6) valid for all $\operatorname{Re} n > 0$ in the Abel summation sense.

If we consider Eq. (5.4), and apply a uniform rescaling by a factor of $\frac{1}{2}\sqrt{s}\tilde{Q}$ of the lattice Λ, Eq. (5.4) is in a form where we can then apply Eq. (C.6) to find an expression equivalent to Eq. (5.11) under its proper rescaling (the dual lattice Λ^* needs to be uniformly rescaled by a factor of $\left(\frac{1}{2}\sqrt{s}\tilde{Q}\right)^{-1}$ in order to be the dual lattice of the rescaled Λ).

Appendix D

s Channel Dispersion Relations

We are interested in evaluating the s channel contribution to the NLO amplitude

$$\overline{V}_n(s,\{L_i\},\mu) = -\frac{1}{32\pi^2}\int_0^1 dx\Bigg\{\ln\frac{\mu^2}{m^2-x(1-x)s-i\varepsilon} + 2{\sum_{\vec{k}\in\mathbb{Z}^n}}' K_0\left(2\pi\sum L_i k_i\sqrt{m^2-x(1-x)s-i\varepsilon}\right)\Bigg\}, \quad \text{(D.1)}$$

which in its current form is numerically ill-behaved. For simplicity, let us define

$$f(\sigma,\varepsilon) = \int_0^1 dx \ln\left(\frac{1}{1-x(1-x)\sigma-i\varepsilon}\right) \quad \text{(D.2)}$$

$$g_n(\Lambda,\sigma,\varepsilon) = f(\sigma,\varepsilon) + 2{\sum_{\vec{k}\in\Lambda}}'\int_0^1 dx K_0\left(2\pi\|\vec{k}\|\sqrt{1-x(1-x)\sigma-i\varepsilon}\right), \quad \text{(D.3)}$$

where Λ is an n-dimensional lattice. We note that using the dominated convergence theorem [10] one can show that, as long as there are no $\vec{\ell}\in\Lambda^*$ with $\ell^2 = \frac{\sigma}{4}-1$, one can safely take both the $\sigma\to\infty$ or lattice spacings of Λ to ∞ limits using that $K_0 \sim e^{-x}/\sqrt{x}$ to show that $g_n(\Lambda,\sigma,\varepsilon)\sim f(\sigma,\varepsilon)$ in these limits. Eqs. (D.2) and (D.3) then allow us to write Eq. (D.1) as

$$\overline{V}_n(s,\{L_i\},\mu) = -\frac{1}{32\pi^2}\left[\ln\left(\frac{\mu^2}{m^2}\right) + g_n\left(\Lambda(\{L_i m\}),\frac{s}{m^2},\varepsilon\right)\right], \quad \text{(D.4)}$$

where $\Lambda(\{L_i m\})$ is the n-dimensional rectangular lattice with lattice spacings given by the $L_i m$. In the special case of all finite lengths being equal,

$$\overline{V}_n(s,L,\mu) = -\frac{1}{32\pi^2}\left[\ln\left(\frac{\mu^2}{m^2}\right) + g_n\left(\Lambda(Lm),\frac{s}{m^2},\varepsilon\right)\right], \quad \text{(D.5)}$$

where $\Lambda(Lm)$ is then the n-dimensional square lattice with all lattice spacings equal to Lm.

Imaginary part

We will try to exploit the complex structure of these functions to find a numerically well behaved equivalent form for Eq. (D.1). We have chosen to self-consistently take the arg, log, K_0, and the square root branch cuts along the negative real axis. This straightforwardly gives that both f and g have a branch cut along the positive real axis from $\sigma = 4$ to $\sigma = \infty$. The real part of both f and g is continuous across the branch cut, and the imaginary part changes sign. We further need to make the assumption that there are no poles for g in the complex σ plane off of the positive real axis. This assumption seems reasonable and is supported by numerics. We do however note that there are physical situations where the S-matrix has poles violating this assumption [78]. Something we can easily calculate and evaluate is the imaginary part of f as follows:

$$\begin{aligned}\operatorname{Im} f(\sigma,\varepsilon) &= \int_0^1 dx \operatorname{Im} \ln\left(\frac{1}{1-x(1-x)\sigma - i\varepsilon}\right) \\ &= \int_0^1 dx \pi\theta\left(x(1-x)\sigma - 1\right) + \mathcal{O}(\varepsilon) \\ \operatorname{Im} f(\sigma,0^+) &= \pi\sqrt{1-\frac{4}{\sigma}},\end{aligned} \tag{D.6}$$

where ε helped us avoid the branch cut and choose the sign of the imaginary part. We will use 0^+ to denote that our ε is some infinitesimal positive real number, but since ε only selects a branch cut we will neglect to write it. This does mean we need to be continually mindful of branch cuts. We can then continue onward to calculate

$$\begin{aligned}I &\equiv \operatorname{Im} \int_0^1 dx K_0\left(2\pi\|\vec{k}\|\sqrt{1-x(1-x)\sigma - i\varepsilon}\right) \\ &= \int_0^1 dx \operatorname{Im} K_0\left(2\pi\|\vec{k}\|\sqrt{1-x(1-x)\sigma - i\varepsilon}\right).\end{aligned}$$

We again use the ε to avoid the branch cut and indicate the sign of the imaginary part, giving us

$$I = \frac{\pi}{2}\int_0^1 dx J_0\left(2\pi\|\vec{k}\|\sqrt{x(1-x)\sigma - 1}\right)\theta\left(x(1-x)\sigma - 1\right) + \mathcal{O}(\varepsilon).$$

We can then discard the $\mathcal{O}(\varepsilon)$ terms. We can also use the symmetry of the integral about $x = \frac{1}{2}$ and the step function to find

$$I = \pi \int_{\frac{1}{2}}^{\frac{1}{2}+\frac{1}{2}\sqrt{1-\frac{4}{\sigma}}} dx J_0\left(2\pi\|\vec{k}\|\sqrt{x(1-x)\sigma - 1}\right). \tag{D.7}$$

We can further simplify Eq. (D.7) by using the substitution $y \equiv \dfrac{x-\frac{1}{2}}{\frac{1}{2}\sqrt{1-\frac{4}{\sigma}}}$ to find

$$I = \frac{\pi}{2}\sqrt{1-\frac{4}{\sigma}}\int_0^1 dy J_0\left(2\pi\|\vec{k}\|\sqrt{\frac{\sigma}{4}-1}\sqrt{1-y^2}\right).$$

We then use $\displaystyle\int_0^1 dy\, J_0(a\sqrt{1-y^2}) = \mathrm{sinc}(a)$ to find

$$I = \frac{\pi}{2}\sqrt{1-\frac{4}{\sigma}}\,\mathrm{sinc}\left(2\pi\|\vec{k}\|\sqrt{\frac{\sigma}{4}-1}\right). \tag{D.8}$$

We can combine Eqs. (D.6) and (D.8) to find

$$\mathrm{Im}\, g_n(\Lambda,\sigma,0^+) = \pi\sqrt{1-\frac{4}{\sigma}}\sum_{\vec{k}\in\Lambda}\mathrm{sinc}\left(2\pi\sqrt{\frac{\sigma}{4}-1}\|\vec{k}\|\right) \tag{D.9}$$

which now allows us to use a uniformly rescaled Eq. (C.6) in order to write Eq. (D.9) as

$$\begin{aligned}\mathrm{Im}\, g_n(\Lambda,\sigma,0^+) &= \pi\sqrt{1-\frac{4}{\sigma}}\frac{\pi^{\frac{1-n}{2}}|\Lambda^*|}{2\Gamma\left(\frac{3-n}{2}\right)\sqrt{\frac{\sigma}{4}-1}^n}\sum_{\substack{\vec{\ell}\in\Lambda^*\\ \ell^2\le\frac{\sigma}{4}-1}}^{*}\sqrt{1-\frac{\ell^2}{\frac{\sigma}{4}-1}}^{1-n}\\ &= \frac{\pi^{\frac{3-n}{2}}|\Lambda^*|}{\sqrt{\sigma}\Gamma\left(\frac{3-n}{2}\right)}\sum_{\vec{\ell}\in\Lambda^*}^{*}\left(\frac{\sigma}{4}-1-\ell^2\right)^{\frac{1-n}{2}}\theta\left(\frac{\sigma}{4}-1-\ell^2\right).\end{aligned} \tag{D.10}$$

Complex Analysis

For asymptotically large $|\sigma|$, we find that $|g_n(\Lambda,\sigma,\varepsilon)/\sigma^2|$ falls of faster than $|\sigma|^{-1}$ for $n < 3$ dimensional lattices. We can use this as follows. Consider the Cauchy integral formula

$$\frac{d}{d\sigma}\left(g_n(\Lambda,\sigma,0^+)\right) = \frac{1}{2\pi i}\int_\gamma dz\frac{g_n(\Lambda,z,0^+)}{(z-\sigma)^2}, \tag{D.11}$$

where γ is some small counter-clockwise contour around the pole at $z = \sigma$.

Looking at the complex structure as discussed above and shown in Fig. D.1, we can see that we can deform our contour around the branch cut just under the real axis (offset due to $\varepsilon = 0^+$). Then since $g_n(\Lambda,\sigma,0)/\sigma^2$ falls off faster than σ^{-1}, the integral along

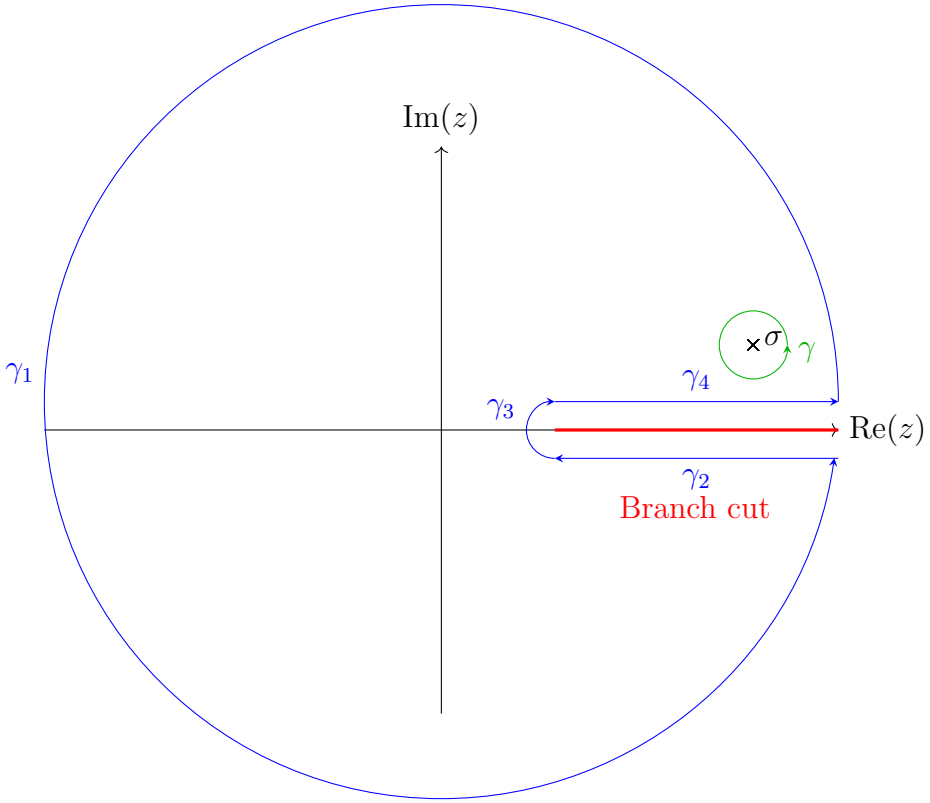

Figure D.1: The analytic structure of Eq. (D.11).

γ_1 does not contribute. It's also possible to show that the integral along γ_3 does not contribute. This leaves us with γ_2, γ_4.

$g_n(\Lambda, \sigma, 0)$ has a real part that is continuous across its branch cut, and the imaginary part simply changes sign, so since γ_2, γ_4 run in opposite directions along opposite sides of the branch cut, we find

$$\frac{d}{d\sigma}\left(g_n(\Lambda,\sigma,0^+)\right)\Big|_{\sigma=\sigma_0+i\eta} = \frac{1}{\pi}\int_4^\infty dz \frac{\operatorname{Im} g_n(\Lambda,z,0^+)}{(z-\sigma_0-i\eta)^2} \tag{D.12}$$

$$= \frac{\pi^{\frac{1-n}{2}}|\Lambda^*|}{\Gamma\left(\frac{3-n}{2}\right)} \sum_{\ell\in\Lambda^*} \int_4^\infty dz \frac{\theta\left(\frac{z}{4}-1-\ell^2\right)}{\sqrt{z}\left(\frac{z}{4}-1-\ell^2\right)^{\frac{n-1}{2}}} \frac{1}{(z-\sigma_0-i\eta)^2}. \tag{D.13}$$

We have pushed the pole we introduced through the Cauchy integral formula into the upper-half plane, such that it is inside the contour we are considering, and not exactly on the branch cut itself, since our contour needs to run between the two.

Integrating both sides with respect to σ_0 (note that this is a contour integral, so some

care needs to be taken) then gives

$$g_n(\Lambda,\sigma+i\eta,0^+)-g_n(\Lambda,\sigma_0+i\eta,0^+)= \frac{\pi^{\frac{1-n}{2}}|\Lambda^*|}{\Gamma\left(\frac{3-n}{2}\right)}\sum_{\ell\in\Lambda^*}\int_4^\infty dz\frac{\theta\left(\frac{z}{4}-1-\ell^2\right)}{\sqrt{z}\left(\frac{z}{4}-1-\ell^2\right)^{\frac{n-1}{2}}}\left[\frac{1}{z-\sigma-i\eta}-\frac{1}{z-\sigma_0-i\eta}\right]. \quad \text{(D.14)}$$

Case: $n=0$

In principle, the $n=0$ case is trivial as there is no sum to perform. However, we will examine the $n=0$ case for three reasons. First, we would like to confirm that Eq. (D.14) reproduces the original Eq. (D.3), which in this case trivially reduces to Eq. (D.2). Second, we will find that even in this simple case we will utilise a method that will be extremely useful in the higher n cases. Third, we will use an asymptotic form of Eq. (D.2), which will prove invaluable for the higher n cases.

Simply setting $n=0$, there is no sum to be performed in Eq. (D.3), and we obtain

$$g_0(\{\vec{0}\},\sigma+i\eta,0^+)-g_0(\{\vec{0}\},\sigma_0+i\eta,0^+) = \int_4^\infty dz\sqrt{1-\frac{4}{z}}\left[\frac{1}{z-\sigma-i\eta}-\frac{1}{z-\sigma_0-i\eta}\right]. \quad \text{(D.15)}$$

Integrating and then safely taking $\eta\to 0$

$$g_0(\{\vec{0}\},\sigma,0^+)-g_0(\{\vec{0}\},\sigma_0,0^+)=2\sqrt{1-\frac{4}{\sigma}} \times\left[\left(\operatorname{arctanh}\left(\sqrt{1-\frac{4}{\sigma}}\right)+\operatorname{arctanh}\left(\frac{2-\sigma}{\sqrt{\sigma(\sigma-4)}}\right)\right) -\left(\operatorname{arctanh}\left(\sqrt{1-\frac{4}{\sigma_0}}\right)+\operatorname{arctanh}\left(\frac{2-\sigma_0}{\sqrt{\sigma_0(\sigma_0-4)}}\right)\right)\right]. \quad \text{(D.16)}$$

We can rearrange Eq. (D.16) to obtain

$$g_0(\{\vec{0}\},\sigma,0^+)=\Bigg[g_0(\{\vec{0}\},\sigma_0,0^+) -2\sqrt{1-\frac{4}{\sigma_0}}\left(\operatorname{arctanh}\left(\sqrt{1-\frac{4}{\sigma_0}}\right)+\operatorname{arctanh}\left(\frac{2-\sigma_0}{\sqrt{\sigma_0(\sigma_0-4)}}\right)\right)\Bigg] +2\sqrt{1-\frac{4}{\sigma}}\left(\operatorname{arctanh}\left(\sqrt{1-\frac{4}{\sigma}}\right)+\operatorname{arctanh}\left(\frac{2-\sigma}{\sqrt{\sigma(\sigma-4)}}\right)\right). \quad \text{(D.17)}$$

Since the left hand side is explicitly independent of σ_0, we know the first term on the right-hand side must be σ_0 independent and is simply a constant that needs to be

determined. (We will exploit this method of isolating the σ_0 independent constant in the higher n cases.) We therefore define

$$a_0 \equiv$$
$$g_0(\{\vec{0}\},\sigma_0,0^+) - 2\sqrt{1-\frac{4}{\sigma_0}}\left(\operatorname{arctanh}\left(\sqrt{1-\frac{4}{\sigma_0}}\right)+\operatorname{arctanh}\left(\frac{2-\sigma_0}{\sqrt{\sigma_0(\sigma_0-4)}}\right)\right) \quad \text{(D.18)}$$

in order to obtain

$$g_0(\{\vec{0}\},\sigma,0^+) =$$
$$a_0 + 2\sqrt{1-\frac{4}{\sigma}}\left(\operatorname{arctanh}\left(\sqrt{1-\frac{4}{\sigma}}\right)+\operatorname{arctanh}\left(\frac{2-\sigma}{\sqrt{\sigma(\sigma-4)}}\right)\right). \quad \text{(D.19)}$$

For the higher n cases, we'll need to take $\sigma_0 \to \infty$ and evaluate an equation similar to Eq. (D.18) numerically. For the $n = 0$ case we may analytically evaluate a_0. We first note that $g_0(\{\vec{0}\},\sigma,0^+) = f(\sigma,0^+)$, and thus for $\sigma > 4$

$$g_0(\{\vec{0}\},\sigma,0^+) = 2 - 2\sqrt{1-\frac{4}{\sigma}}\operatorname{arccoth}\left(\sqrt{1-\frac{4}{\sigma}}\right) \quad \text{(D.20)}$$

from an explicit analytic evaluation of Eq. (D.2). One may then evaluate a_0 in Eq. (D.18) by taking $\sigma \to \sigma_0$ in Eq. (D.20) and then simplifying to find that

$$a_0 = 2. \quad \text{(D.21)}$$

Therefore

$$g_0(\{\vec{0}\},\sigma,0^+) = 2 + 2\sqrt{1-\frac{4}{\sigma}}\left[\operatorname{arctanh}\left(\sqrt{1-\frac{4}{\sigma}}\right)+\operatorname{arctanh}\left(\frac{2-\sigma}{\sqrt{\sigma(\sigma-4)}}\right)\right], \quad \text{(D.22)}$$

and we have successfully found an explicit expression for g_0 using our alternative method of derivation. We note that for $\sigma > 4$ one can show analytically that Eq. (D.22) is equivalent to Eq. (D.20), and thus Eq. (D.22) is equivalent to Eq. (D.3) for $n = 0$.

For the higher n cases we'll need the following asymptotic form for Eq. (D.2), which readily comes from the large σ expansion of Eq. (D.20):

$$f(\sigma,0^+) = 2 + i\pi - \ln(\sigma) + \mathcal{O}(\sigma^{-1}). \quad \text{(D.23)}$$

Case: $n = 1$

We may now consider the first non-trivial case, $n = 1$. In this case we may compare a brute force evaluation of Eq. (D.3) with a numerical evaluation of an equivalent form that we now derive with the methods we have developed so far.

Considering Λ to be a 1D lattice

$$\begin{aligned} & g_1(\Lambda, \sigma + i\eta, 0^+) - g_1(\Lambda, \sigma_0 + i\eta, 0^+) \\ &= |\Lambda^*| \sum_{\ell \in \Lambda^*} \int_4^\infty dz \frac{\theta\left(\frac{z}{4} - 1 - \ell^2\right)}{\sqrt{z}} \times \left[\frac{1}{z - \sigma - i\eta} - \frac{1}{z - \sigma_0 - i\eta} \right] \qquad \text{(D.24)} \\ &= |\Lambda^*| \sum_{\ell \in \Lambda^*} \int_{4(1+\ell^2)}^\infty \frac{dz}{\sqrt{z}} \left[\frac{1}{z - \sigma - i\eta} - \frac{1}{z - \sigma_0 - i\eta} \right] \qquad \text{(D.25)} \\ &= 2|\Lambda^*| \sum_{\ell \in \Lambda^*} \left(\frac{\operatorname{arctanh}\left(\frac{1}{2}\sqrt{\frac{\sigma + i\eta}{1+l^2}}\right)}{\sqrt{\sigma + i\eta}} - \frac{\operatorname{arctanh}\left(\frac{1}{2}\sqrt{\frac{\sigma_0 + i\eta}{1+l^2}}\right)}{\sqrt{\sigma_0 + i\eta}} \right). \qquad \text{(D.26)} \end{aligned}$$

We now have to be careful how we split up the sum in Eq. (D.26), to ensure we don't lose convergence. If we look at the asymptotic behaviour of each term, we see that both asymptotically decay like $1/|l|$, so we can add and subtract any function that has the same asymptotic form in order to separate the σ and σ_0 dependent parts respectively. A convenient and natural choice then is simply $1/\sqrt{1 + l^2}$. We also note that the η is there to ensure the correct branch cut choice. Since $\sigma > 4$, we may therefore safely take $\eta = 0$ in the denominator of Eq. (D.26). We can then split our sum into two convergent sums:

$$\begin{aligned} g_1(\Lambda, \sigma + i\eta, 0^+) - g_1(\Lambda, \sigma_0 + i\eta, 0^+) = & \\ & |\Lambda^*| \sum_{\ell \in \Lambda^*} \left(\frac{2}{\sqrt{\sigma}} \operatorname{arctanh}\left(\frac{1}{2}\sqrt{\frac{\sigma}{1+l^2}} + i\eta\right) - \frac{1}{\sqrt{1+\ell^2}} \right) \\ & - |\Lambda^*| \sum_{\ell \in \Lambda^*} \left(\frac{2}{\sqrt{\sigma_0}} \operatorname{arctanh}\left(\frac{1}{2}\sqrt{\frac{\sigma_0}{1+l^2}} + i\eta\right) - \frac{1}{\sqrt{1+\ell^2}} \right). \qquad \text{(D.27)} \end{aligned}$$

We can then rearrange Eq. (D.27) as

$$\begin{aligned} g_1(\Lambda, \sigma, 0^+) = & \left[g_1(\Lambda, \sigma_0, 0^+) - |\Lambda^*| \sum_{\ell \in \Lambda^*} \left(\frac{2}{\sqrt{\sigma_0}} \operatorname{arctanh}\left(\frac{1}{2}\sqrt{\frac{\sigma_0}{1+l^2}} + i\eta\right) - \frac{1}{\sqrt{1+\ell^2}} \right) \right] \\ & + |\Lambda^*| \sum_{\ell \in \Lambda^*} \left(\frac{2}{\sqrt{\sigma}} \operatorname{arctanh}\left(\frac{1}{2}\sqrt{\frac{\sigma}{1+l^2}} + i\eta\right) - \frac{1}{\sqrt{1+\ell^2}} \right). \qquad \text{(D.28)} \end{aligned}$$

Since the left hand side is again independent of σ_0, we know the first term must be a func-

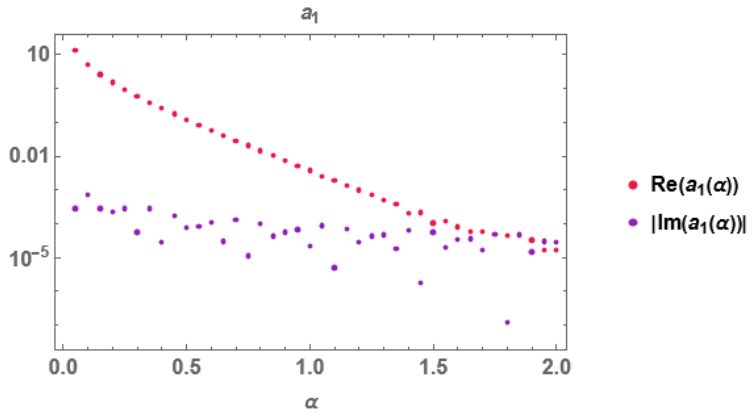

Figure D.2: The real and imaginary parts of a_1 as a function of the lattice spacing α on a log scale. The absolute value of the imaginary part was taken, since it oscillates around 0.

tion of only the lattice. Noticing that for asymptotically large σ_0 we have $g_1(\Lambda, \sigma_0, 0^+) \sim f(\sigma_0, 0^+) \sim 2 + i\pi - \ln(\sigma)$, where the first asymptotic can be seen from Eq. (D.3) and the second can be computed easily from Eq. (D.2). We can now numerically and asymptotically evaluate

$$a_1(\Lambda) \equiv 2 + i\pi + \lim_{\sigma_0 \to \infty} \left[-\ln(\sigma_0) - |\Lambda^*| \sum_{\ell \in \Lambda^*} \left(\frac{2}{\sqrt{\sigma_0}} \operatorname{arctanh}\left(\frac{1}{2}\sqrt{\frac{\sigma_0}{1+l^2}} + i\eta \right) - \frac{1}{\sqrt{1+\ell^2}} \right) \right] \quad \text{(D.29)}$$

in order to obtain

$$g_1(\Lambda, \sigma + i\eta, 0^+) = a_1(\Lambda) + |\Lambda^*| \sum_{\ell \in \Lambda^*} \left(\frac{2}{\sqrt{\sigma}} \operatorname{arctanh}\left(\frac{1}{2}\sqrt{\frac{\sigma}{1+l^2}} + i\eta \right) - \frac{1}{\sqrt{1+\ell^2}} \right). \quad \text{(D.30)}$$

We plot $a_1(\Lambda)$ as a function of the lattice spacing α of the $n = 1$ dimensional lattice Λ in Fig. D.2. We can then compare g_1 with an $n = 1$ dimensional lattice at different lattice spacings calculated with Eq. (D.30) versus Eq. (D.3) in Fig. D.3. We note that there is a subtlety in the ordering of the limits in Eq. (D.29) that affects numerics. There is no general way to move the $\log(\sigma_0)$ inside the sum in Eq. (D.29), and so we must take the limit of the upper bound of the infinite sum before we take the $\sigma_0 \to \infty$ limit. For some σ_0 we need to sum all vectors $\vec{\ell}$ that don't give vanishing $\sqrt{\sigma_0/(1+l^2)}$, but since we have a logarithmic divergence in σ_0, we need to have $\sigma_0 \sim 10^5$ to get precision on the order of 10^{-1} for a_1. Since the real part of a_1 is significantly larger than the imaginary

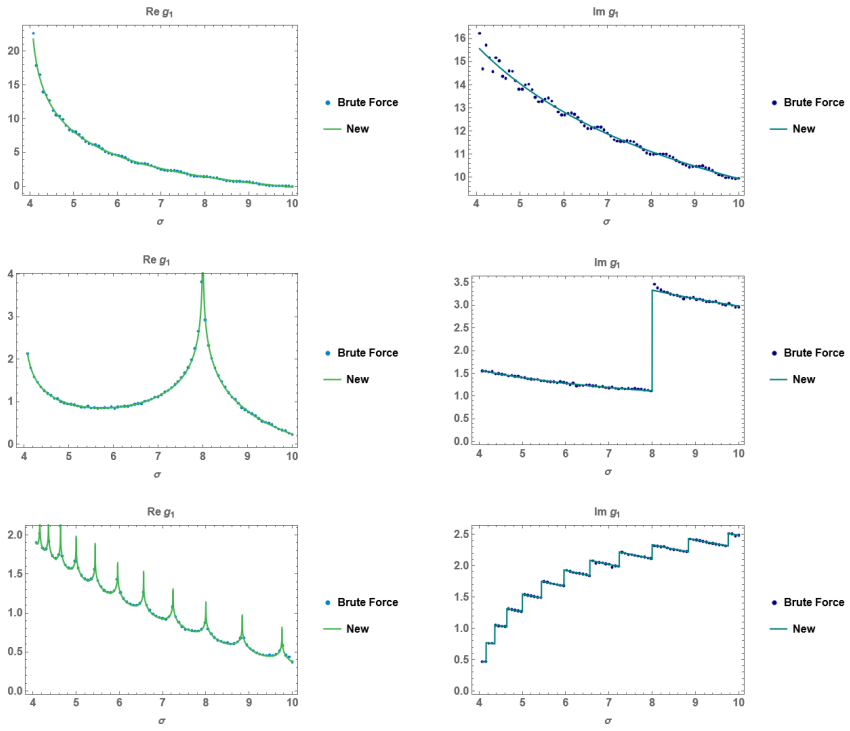

Figure D.3: Comparison of real and imaginary parts of g_1 calculated with Eq. (D.30) ("New") versus Eq. (D.3) with $n = 1$ ("Brute Force"), with lattice spacing $= 0.1, 1, 10$ from top to bottom.

part, the real part is much less sensitive to this limiting issue than the imaginary part, as can be seen in Fig. D.2. This lack of precision in the imaginary part of a_1 ends up not mattering, since the imaginary part coming from the rest of g_1 in Eq. (D.30) is orders of magnitude larger than that coming from a_1. We can confirm that the lack of numerical precision of a_1 is irrelevant by examining the comparison of g_1 computed by brute force evaluation of Eq. (D.3) and by evaluating the newly derived Eq. (D.30) in Fig. D.3. We can furthermore see how much faster Eq. (D.30) converges when compared to Eq. (D.3) with an $n = 1$ dimensional lattice in Fig. D.4.

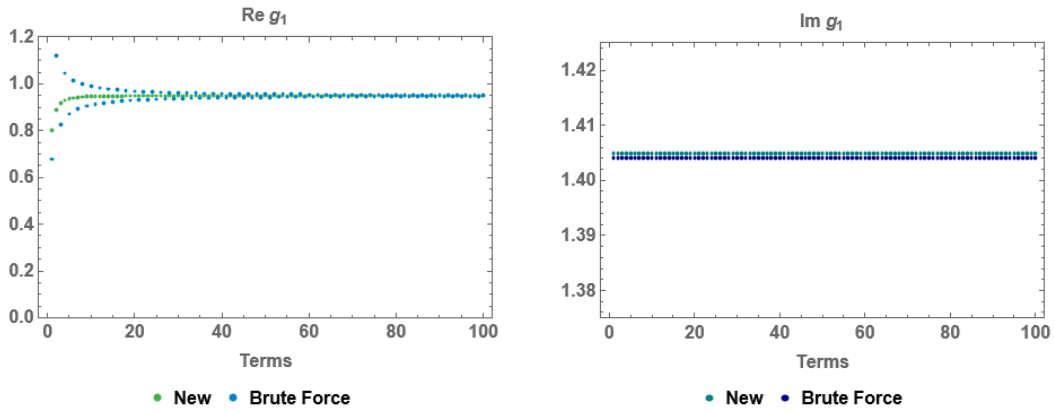

Figure D.4: Convergence of partial sums of the real (left) and imaginary (right) parts of g_1 from a "Brute Force" evaluation of Eq. (D.3) (blue) compared to the "New" method of Eq. (D.30) (green) on a lattice with lattice spacing unity, and at $\sigma = 5$.

Case: $n = 2$

Considering Λ to be a 2D lattice

$$\begin{aligned} &g_2(\Lambda, \sigma + i\eta, 0^+) - g_2(\Lambda, \sigma_0 + i\eta, 0^+) \\ &= \frac{|\Lambda^*|}{\pi} \sum_{\ell \in \Lambda^*} \int_4^\infty dz \frac{\theta\left(\frac{z}{4} - 1 - \ell^2\right)}{\sqrt{z}\left(\frac{z}{4} - 1 - \ell^2\right)^{\frac{1}{2}}} \left[\frac{1}{z - \sigma - i\eta} - \frac{1}{z - \sigma_0 - i\eta}\right] \qquad \text{(D.31)} \\ &= \frac{4|\Lambda^*|}{\pi} \sum_{\ell \in \Lambda^*} \left(\frac{\arcsin\left(\frac{1}{2}\sqrt{\frac{\sigma + i\eta}{1+\ell^2}}\right)}{\sqrt{\sigma + i\eta}\sqrt{4\ell^2 - (\sigma + i\eta - 4)}} - \frac{\arcsin\left(\frac{1}{2}\sqrt{\frac{\sigma_0 + i\eta}{1+\ell^2}}\right)}{\sqrt{\sigma_0 + i\eta}\sqrt{4\ell^2 - (\sigma_0 + i\eta - 4)}} \right). \qquad \text{(D.32)} \end{aligned}$$

We can again carefully split up the terms, where an appropriate and natural term to add and subtract is $1/1 + \ell^2$,

$$\begin{aligned} g_2(\Lambda, \sigma + i\eta, 0^+) - g_2(\Lambda, \sigma_0 + i\eta, 0^+) =& \frac{|\Lambda^*|}{\pi} \sum_{\ell \in \Lambda^*} \left(\frac{2\arcsin\left(\frac{1}{2}\sqrt{\frac{\sigma}{1+\ell^2}} + i\eta\right)}{\sqrt{\sigma}\sqrt{\ell^2 + 1 - \frac{\sigma}{4} - i\eta}} - \frac{1}{1+\ell^2} \right) \\ &- \frac{|\Lambda^*|}{\pi} \sum_{\ell \in \Lambda^*} \left(\frac{2\arcsin\left(\frac{1}{2}\sqrt{\frac{\sigma_0}{1+\ell^2}} + i\eta\right)}{\sqrt{\sigma_0}\sqrt{\ell^2 + 1 - \frac{\sigma_0}{4} - i\eta}} - \frac{1}{1+\ell^2} \right). \end{aligned} \qquad \text{(D.33)}$$

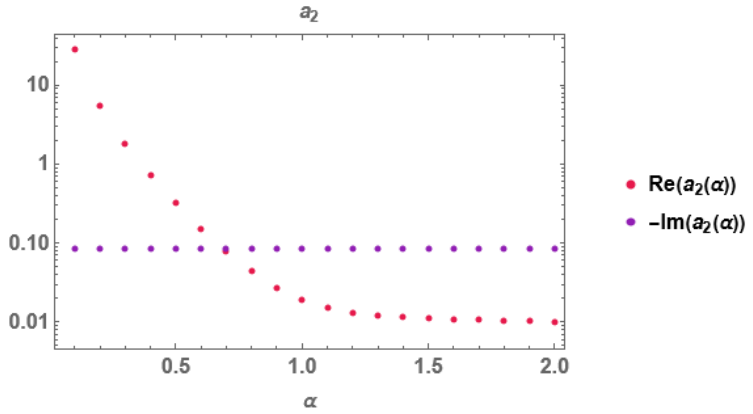

Figure D.5: The real and (minus the) imaginary parts of a_2 for a square lattice as a function of the lattice spacing α.

We can rearrange Eq. (D.33) as

$$g_2(\Lambda,\sigma,0^+) = \left[g_2(\Lambda,\sigma_0,0^+) - \frac{|\Lambda^*|}{\pi}\sum_{\ell\in\Lambda^*}\left(\frac{2\arcsin\left(\frac{1}{2}\sqrt{\frac{\sigma_0}{1+\ell^2}}+i\eta\right)}{\sqrt{\sigma_0}\sqrt{\ell^2+1-\frac{\sigma_0}{4}-i\eta}} - \frac{1}{1+\ell^2}\right)\right] + \frac{|\Lambda^*|}{\pi}\sum_{\ell\in\Lambda^*}\left(\frac{2\arcsin\left(\frac{1}{2}\sqrt{\frac{\sigma}{1+\ell^2}}+i\eta\right)}{\sqrt{\sigma}\sqrt{\ell^2+1-\frac{\sigma}{4}-i\eta}} - \frac{1}{1+\ell^2}\right). \quad \text{(D.34)}$$

Since the left hand side is independent of σ_0, we know the first term must be a function of only the lattice. With the same reasoning as for $n=1$, we can now introduce

$$a_2(\Lambda) \equiv 2 + i\pi + \lim_{\sigma_0\to\infty}\left[-\ln(\sigma_0) - \frac{|\Lambda^*|}{\pi}\sum_{\ell\in\Lambda^*}\left(\frac{2\arcsin\left(\frac{1}{2}\sqrt{\frac{\sigma_0}{1+\ell^2}}+i\eta\right)}{\sqrt{\sigma_0}\sqrt{\ell^2+1-\frac{\sigma_0}{4}-i\eta}} - \frac{1}{1+\ell^2}\right)\right] \quad \text{(D.35)}$$

in order to obtain

$$g_2(\Lambda,\sigma+i\eta,0^+) = a_2(\Lambda) + \frac{|\Lambda^*|}{\pi}\sum_{\ell\in\Lambda^*}\left(\frac{2\arcsin\left(\frac{1}{2}\sqrt{\frac{\sigma}{1+\ell^2}}+i\eta\right)}{\sqrt{\sigma}\sqrt{\ell^2+1-\frac{\sigma}{4}-i\eta}} - \frac{1}{1+\ell^2}\right). \quad \text{(D.36)}$$

An equivalent expression was found in [9]. We plot $a_2(\Lambda)$ as a function of the lattice spacing α for a square $n=2$ dimensional lattice in Fig. D.5. In contrast to a_1, we find that Eq. (D.35) is more numerically stable. The order $\mathcal{O}(\ell)$ in the denominator of Eq. (D.35), means that terms vanish for large ℓ no matter the value of σ_0.

One can see how much faster Eq. (D.36) converges compared to Eq. (D.3) in an $n=2$ dimensional lattice in Fig. D.6.

We can now compare the summation of $\sim 10^4$ terms of Eq. (D.1) directly for the real

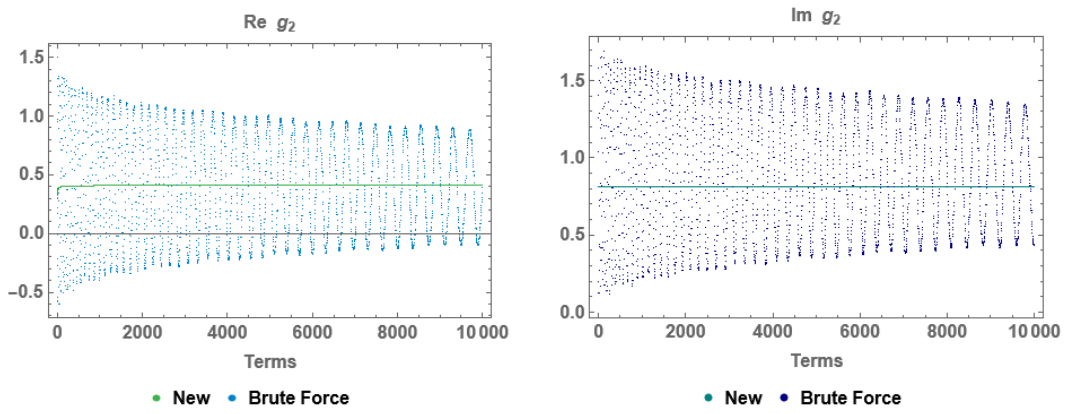

Figure D.6: Convergence of partial sums of the real (left) and imaginary (right) parts of g_2 from a "Brute Force" evaluation of Eq. (D.3) (blue) compared to the "New" method of Eq. (D.36) (green) on a lattice with lattice spacing unity, and at $\sigma = 5$.

part of the s-channel at $p = 1$ GeV and scanning in L (the length of both finite directions), as well as for constant $L_1 = L_2 = 1/\sqrt{3}$ GeV^{-1} scanning in p, to the summation of only 10^3 terms of Eq. (D.36). In Fig. D.7 we can see this comparison, making it clear why this detour to derive a more numerically friendly form was necessary. We understand the apparent disagreement of the two methods at small L in Fig. D.7 as due to the exceptionally slow numerical convergence of the "Brute Force" method of evaluation of Eq. (D.1), which does not accurately capture the divergence of $\overline{V}_2(s, L, \mu)$. Intuitively, as L decreases, the number of terms required to accurately determine $\overline{V}_2(s, L, \mu)$ using the "Brute Force" method diverges. The advantage of the "New" method is that it sums over the dual lattice, so as L decreases, the method becomes more and more accurate for any fixed number of terms included. (In principle, then, the "New" method becomes inaccurate at large enough L; we however have not encountered yet a value of L for which the method fails numerically.)

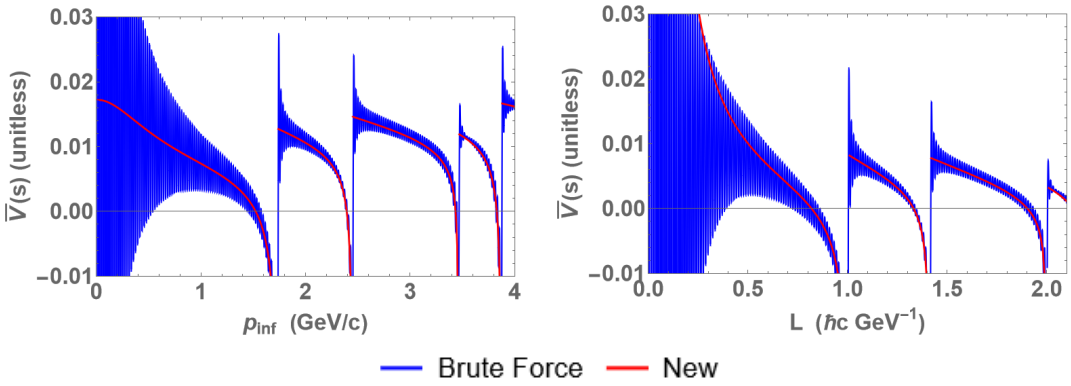

Figure D.7: *Left*: Re $\overline{V}_2(s, L, \mu)$ with $s = 4(m^2+p^2)$, $m = 0.5$ GeV, $\mu = 1$ GeV, $L = 1/\sqrt{3}$ GeV^{-1} and scanning in p naively summed to 10^4 terms in blue (note that what might appear to be solid filled in, is in fact high-resolution oscillations, due to bad numerical behaviour) compared to the 1000 terms of the newly derived result in red.
Left: Same as to the left, but with $p = 1$ GeV and scanning in L.

Bibliography

[1] Abelev B, Adam J *et al.* 2013 *Physics Letters B* **719** 29–41 ISSN 0370-2693 URL www.sciencedirect.com/science/article/pii/S037026931300035X

[2] Aad G, Abajyan T, Abbott B *et al.* (ATLAS Collaboration) 2013 *Phys. Rev. Lett.* **110**(18) 182302 URL https://link.aps.org/doi/10.1103/PhysRevLett.110.182302

[3] Adare A, Aidala C *et al.* (PHENIX Collaboration) 2013 *Phys. Rev. Lett.* **111**(21) 212301 URL https://link.aps.org/doi/10.1103/PhysRevLett.111.212301

[4] Aad G, Abbott B *et al.* (ATLAS Collaboration) 2016 *Phys. Rev. Lett.* **116**(17) 172301 URL https://link.aps.org/doi/10.1103/PhysRevLett.116.172301

[5] Weller R D and Romatschke P 2017 *Phys. Lett. B* **774** 351–356 ISSN 0370-2693

[6] Mogliacci S, Kolbé I and Horowitz W A 2020 *Phys. Rev. D* **102** 116017 (*Preprint* 1807.07871)

[7] Kitazawa M, Mogliacci S, Kolbé I and Horowitz W A 2019 *Phys. Rev. D* **99** 094507 (*Preprint* 1904.00241)

[8] Horowitz W A and Du Plessis J F 2022 *Phys. Rev. D* **105**(9) L091901 URL link.aps.org/doi/10.1103/PhysRevD.105.L091901

[9] Horowitz W A and Du Plessis J F 2023 Finite system size correction to the effective coupling in ϕ^4 scattering (*Preprint* 2308.08651)

[10] Du Plessis J F and Horowitz W A 2022 NLO scattering in ϕ^4 theory finite system size corrections self-consistency *International Nuclear Physics Conference Proceedings*

[11] Du Plessis J F and Horowitz W A 2022 Finite system size correction in ϕ^4 theory NLO scattering using denominator regularization *Proceedings of 41st International Conference on High Energy physics — PoS(ICHEP2022)* (Sissa Medialab) URL https://doi.org/10.22323/1.414.1206

[12] Du Plessis J F and Horowitz W A 2022 NLO finite system size corrections to $2 \to 2$ scattering in ϕ^4 theory using newly derived sum of sinc functions (*Preprint* 2209.15309)

[13] Du Plessis J F and Horowitz W A 2022 Analytic continuation of the generalized epstein zeta function for calculating finite system corrections in ϕ^4 theory *The Proceedings of SAIP2022, the 66th Annual Conference of the South African Institute of Physics* (South African Institute of Physics) URL https://events.saip.org.za/event/225/page/546-the-proceedings-of-saip2022

[14] Busza W, Rajagopal K and van der Schee W 2018 *Ann. Rev. Nucl. Part. Sci.* **68** 339–376 (*Preprint* 1802.04801)

[15] Collins J C and Perry M J 1975 *Phys. Rev. Lett.* **34**(21) 1353–1356 URL link.aps.org/doi/10.1103/PhysRevLett.34.1353

[16] Linde A D 1979 *Rep. Prog. Phys.* **42** 389 ISSN 0034-4885

[17] Ryden B 2016 *Introduction to Cosmology* 2nd ed (Cambridge University Press)

[18] Šafařík K 2003 Heavy ions (high-energy physics) *Encyclopedia of Physical Science and Technology (Third Edition)* ed Meyers R A (New York: Academic Press) pp 293–307 third edition ed ISBN 978-0-12-227410-7 URL www.sciencedirect.com/science/article/pii/B0122274105003136

[19] Committee T D N S A 2008 *arXiv* (*Preprint* 0809.3137)

[20] Guenther J N 2021 *Eur. Phys. J. A* **57** 1–23 ISSN 1434-601X

[21] Pasechnik R and Šumbera M 2017 *Universe* **3** ISSN 2218-1997 URL www.mdpi.com/2218-1997/3/1/7

[22] Peskin M E and Schroeder D V 1995 *An Introduction to quantum field theory* (Reading, USA: Addison-Wesley) ISBN 978-0-201-50397-5

[23] Mandl F and Shaw G 2011 *Quantum Field theory* (Wiley)

[24] Robinson M, Bland K, Cleaver G and Dittmann J 2008 *arXiv* (*Preprint* 0810.3328)

[25] Robinson M B, Ali T and Cleaver G B 2009 *arXiv* (*Preprint* 0908.1395)

[26] Eichten E, Gottfried K, Kinoshita T, Lane K D and Yan T M 1978 *Phys. Rev. D* **17** 3090 [Erratum: Phys.Rev.D 21, 313 (1980)]

[27] Brambilla N and Vairo A 1999 Quark confinement and the hadron spectrum *13th Annual HUGS AT CEBAF (HUGS 98)* pp 151–220 (*Preprint* hep-ph/9904330)

[28] Achard P, Adriani O, Aguilar-Benitez M, Alcaraz J *et al.* 2005 *Phys. Lett. B* **623** 26–36 ISSN 0370-2693

[29] Newton I 1687 *Philosophiæ Naturalis Principia Mathematica* (London: Societas Regia)

[30] 2019 Runningcc [Online; accessed 8. Aug. 2023] URL web2.ph.utexas.edu/~coker2/index.files/runningcc.htm

[31] Gross D J and Wilczek F 1973 *Phys. Rev. Lett.* **30**(26) 1343–1346 URL link.aps.org/doi/10.1103/PhysRevLett.30.1343

[32] Politzer H D 1973 *Phys. Rev. Lett.* **30**(26) 1346–1349 URL link.aps.org/doi/10.1103/PhysRevLett.30.1346

[33] Aaboud M, Aad G, Abbott B, Abdallah J *et al.* 2017 *Eur. Phys. J. C* **77** 872–34 ISSN 1434-6052

[34] Ploskon M 2018 *arXiv* (*Preprint* 1808.01411)

[35] Yu W 2013 *Nucl. Instrum. Methods Phys. Res., Sect. A* **706** 55–58 ISSN 0168-9002

[36] Miller M L, Reygers K, Sanders S J and Steinberg P 2007 *Annu. Rev. Nucl. Part. Sci.* **57** 205–243 ISSN 0163-8998

[37] Gyulassy M and McLerran L 2005 *Nucl. Phys. A* **750** 30–63 ISSN 0375-9474

[38] Wang X N and Gyulassy M 1992 *Phys. Rev. Lett.* **68**(10) 1480–1483 URL link.aps.org/doi/10.1103/PhysRevLett.68.1480

[39] Gyulassy M and Wang X n 1994 *Nucl. Phys. B* **420** 583–614 ISSN 0550-3213

[40] Adler S S *et al.* (PHENIX) 2006 *Phys. Rev. Lett.* **96** 202301 ISSN 1079-7114

[41] Adler S S *et al.* (PHENIX) 2003 *Phys. Rev. Lett.* **91** 241803 ISSN 1079-7114

[42] Adler S S *et al.* (PHENIX) 2005 *Phys. Rev. Lett.* **94** 232301 ISSN 1079-7114

[43] Gordon L E and Vogelsang W 1993 *Phys. Rev. D* **48**(7) 3136–3159 URL link.aps.org/doi/10.1103/PhysRevD.48.3136

[44] Adler S S *et al.* (PHENIX) 2005 *Phys. Rev. D* **71** 071102 (*Preprint* hep-ex/0502006)

[45] Vitev I and Gyulassy M 2002 *Phys. Rev. Lett.* **89**(25) 252301 URL link.aps.org/doi/10.1103/PhysRevLett.89.252301

[46] Koch P, Müller B and Rafelski J 1986 *Phys. Rep.* **142** 167–262 ISSN 0370-1573

[47] Andersen E *et al.* 1999 *Phys. Lett. B* **449** 401–406 ISSN 0370-2693

[48] Afanasiev S V, Anticic T, Barna D, Bartke J *et al.* 2002 *Phys. Lett. B* **538** 275–281 ISSN 0370-2693

[49] Antinori F, Bacon P A, Badalà A, Barbera R *et al.* 2004 *Phys. Lett. B* **595** 68–74 ISSN 0370-2693

[50] Abelev B, Adam J, Adamová D, Adare A M *et al.* 2014 *Phys. Lett. B* **728** 216–227 ISSN 0370-2693

[51] STAR Collaboration, Abelev B I, Aggarwal M M, Ahammed Z *et al.* 2008 *Phys. Rev. C* **77** 044908 ISSN 2469-9993

[52] Adam J, Adamová D, Aggarwal M M, Rinella G A *et al.* 2017 *Nat. Phys.* **13** 535–539 ISSN 1745-2481

[53] Matsui T and Satz H 1986 *Phys. Lett. B* **178** 416–422 ISSN 0370-2693

[54] 2017 J/Ψ Suppression in QGP Outline: [Online; accessed 8. Aug. 2023] URL slideplayer.com/slide/5216303

[55] PHENIX Collaboration, Adare A, Afanasiev S, Aidala C *et al.* 2011 *Phys. Rev. C* **84** 054912 ISSN 2469-9993

[56] Aggarwal M M 2020 Elliptic Flow in Relativistic Heavy-Ion Collisions *Advances in Nuclear Physics* (Singapore: Springer) pp 161–188 ISBN 978-981-15-9062-7

[57] ATLAS Collaboration, Aad G, Abbott B, Abbott D C *et al.* 2022 *Phys. Rev. C* **105** 064903 ISSN 2469-9993

[58] Gale C, Jeon S and Schenke B 2013 *Int. J. Mod. Phys. A* **28** 1340011 ISSN 0217-751X

[59] Kovtun P, Son D T and Starinets A O 2003 *Journal of High Energy Physics* **2003** 064 URL dx.doi.org/10.1088/1126-6708/2003/10/064

[60] Bazavov A, Bhattacharya T, Cheng M, DeTar C, Ding H T, Gottlieb S, Gupta R, Hegde P, Heller U M, Karsch F, Laermann E, Levkova L, Mukherjee S, Petreczky P, Schmidt C, Soltz R A, Soeldner W, Sugar R, Toussaint D, Unger W and Vranas P (HotQCD Collaboration) 2012 *Phys. Rev. D* **85**(5) 054503 URL link.aps.org/doi/10.1103/PhysRevD.85.054503

[61] Horowitz W A and Rothkopf A 2021 The QCD Equation of State in Small Systems *50th International Symposium on Multiparticle Dynamics* (*Preprint* 2109.01422)

[62] Lehmann H, Symanzik K and Zimmermann W 1955 *Il Nuovo Cimento* **1** 205–225 URL https://doi.org/10.1007/bf02731765

[63] Brodsky S J, Lepage G P and Mackenzie P B 1983 *Phys. Rev. D* **28**(1) 228–235 URL https://link.aps.org/doi/10.1103/PhysRevD.28.228

[64] Brodsky S J, Lepage G P and Mackenzie P B 1983 *Phys. Rev. D* **28** 228

[65] Kirsten K 1994 *J. Math. Phys.* **35** 459–470

[66] Zwillinger D, Moll V, Gradshteyn I and Ryzhik I 2014 *Table of Integrals, Series, and Products (Eighth Edition)* eighth edition ed (Boston: Academic Press) ISBN 978-0-12-384933-5 URL www.sciencedirect.com/science/article/pii/B9780123849335000060

[67] Cohn H, Kumar A, Reiher C and Schürmann A 2013 Formal duality and generalizations of the poisson summation formula. *Discrete geometry and algebraic combinatorics*

[68] Hardy G H 1940 *Ramanujan: Twelve Lectures on Subjects Suggested by His Life and Work* (Cambridge University Press)

[69] Gell-Mann M and Low F 1951 *Phys. Rev.* **84**(2) 350–354 URL https://link.aps.org/doi/10.1103/PhysRev.84.350

[70] Bender C M and Orszag S A 1978 *Advanced Mathematical Methods for Scientists and Engineers* (McGraw-Hill, Inc.) ISBN 0-07-004452-X

[71] Olver F W J (ed) 2010 *NIST Handbook of Mathematical Functions* (Cambridge University Press) ISBN 978-0-521-19225-5

[72] Horowitz W A and Kovchegov Y V 2011 *Nucl. Phys. A* **849** 72–97 (*Preprint* 1009.0545)

[73] Kleinert H and Schulte-Frohlinde V 2001 *Critical Properties of Phi4-Theories* (Singapore: World Scientific Publishing Company) ISBN 978-981-02-4658-7

[74] Montvay I and Munster G 1997 *Quantum fields on a lattice* Cambridge Monographs on Mathematical Physics (Cambridge University Press) ISBN 978-0-521-59917-7, 978-0-511-87919-7

[75] 't Hooft G 1979 *Nucl. Phys. B* **153** 141–160 ISSN 0550-3213

[76] Coste A, Gonzalez-Arroyo A, Jurkiewicz J and Korthals Altes C P 1985 *Nucl. Phys. B* **262** 67–94 ISSN 0550-3213

[77] Johnson-McDaniel N K 2012 *Journal of Fourier Analysis and Applications* **18** 367–385

[78] Moroz A and Miroshnichenko A E 2019 *New Journal of Physics* **21** 103035 URL dx.doi.org/10.1088/1367-2630/ab484b